

Institut für Ionenstrahlphysik und Materialforschung
Helmholtz-Zentrum Dresden-Rossendorf

**Hyperdoping Si with deep-level impurities by ion
implantation and sub-second annealing**

Dissertation

zur Erlangung des akademischen Grades
Doctor rerum naturalium (Dr. rer. nat.)

vorgelegt der Fakultät Mathematik und Naturwissenschaften
der Technischen Universität Dresden

von

Fang Liu

geboren am 10.10.1989 in China

Eingereicht am 08.01.2018

Verteidigt am 20.06.2018

Gutachter:

1. Prof. Dr. Manfred Helm (TU-Dresden and HZDR)
2. Prof. Dr. Elke Wendler (Friedrich-Schiller-Universität Jena)

ACKNOWLEDGEMENTS

Four years ago, I came to Helmholtz-Zentrum Dresden-Rossendorf and started a new journey of my life. Now, my PhD study is more or less finished. During the past four years, I had the joy of success and the frustration of failure. There are too many people and things worth being memorized.

First, I would like to thank my supervisor Prof. Manfred Helm for the insightful comments, critical discussions and hard questions for my work.

I would like give many thanks to Dr. Shengqiang Zhou who is my co-supervisor. My research would not be able to finish without his patient guidance, support and encouragement. Under his guidance I overcame many difficulties and learned a lot in experimental skills, data analysis, presentation and scientific writing, which will lay the groundwork for my future work.

I would give my sincere thanks to Dr. Slawomir Prucnal for the help with flash lamp annealing experiments. I can learn a lot from the every time discussion with him. Also I thank Dr. Slawomir Prucnal for his nice corrections and helpful comments for my scientific papers.

I am very grateful to Dr. Lars Rebohle and Dr. Yonder Berencén for their useful corrections and critical comments for my scientific papers.

I am also deeply indebted to Dr. Wolfgang Skorupa. Thanks for his critical comments and helpful suggestions for my work.

I would like to express my gratitude to Ion Beam Center (IBC) for the ion implantation at HZDR. I thank Dr. Richard Wilhelm and Dr. René Heller for RBS measurements, thank Dr. Rene Hübner and Ms. Elfi Christalle for the SEM and TEM measurements and thank Dr. Martin Engler for the help of CAFM measurement. I am also very grateful to Ms. Ilona Skorupa for gold electrode deposition.

I would like to express my heartfelt gratitude to Dr. Kun Gao, Dr. Yutian Wang, Dr. Yu Liu, Dr. Zhitao Zhang, Ye Yuan, Mao Wang, Chi Xu and other colleagues in our group. I thank their help for my work.

I would like to acknowledge the China Scholarship Council (CSC) that offer generous scholarship for my study in Germany.

I would like to thank my parents for their continuous support and encouragement through these years.

Finally, I would like to express my gratitude to my husband who has been always supporting me through the difficult time. I also thank to his help and company.

Fang Liu

ABSTRACT

Intermediate band (IB) materials have attracted considerable research interest since they can dramatically enhance the near infrared light absorption and lead to applications in the fields of so-called intermediate band solar cells or infrared photodetectors. Hyperdoping Si with deep level impurities is one of the most effective approaches to form an IB inside Si.

In this thesis, titanium (Ti) or chalcogen doped Si with concentrations far exceeding the Mott transition limits ($\sim 5 \times 10^{19} \text{ cm}^{-3}$ for Ti) are fabricated by ion implantation followed by pulsed laser annealing (PLA) or flash lamp annealing (FLA). The structural and electrical properties of the implanted layer are investigated by channeling Rutherford backscattering spectrometry (cRBS) and Hall measurements.

For Si supersaturated with Ti, it is shown that Ti-implanted Si after liquid phase epitaxy shows cellular breakdown at high doping concentrations during the rapid solidification, preventing Ti incorporation into Si matrix. However, the out-diffusion and the cellular breakdown can be effectively suppressed by solid phase epitaxy during FLA, leading to a much higher Ti incorporation. In addition, the formed microstructure of cellular breakdown also complicates the interpretation of the electrical properties. After FLA, the samples remain insulating even with the highest Ti implantation fluence, whereas the sheet resistance decreases with increasing Ti concentration after PLA. According to the results from conductive atomic force microscopy (C-AFM), the decrease of the sheet resistance after PLA is attributed to the percolation of Ti-rich cellular walls, but not to the insulator-to-metal transition due to Ti-doping.

Se-hyperdoped Si samples with different Se concentrations are fabricated by ion implantation followed by FLA. The study of the structural properties of the implanted layer reveals that most Se atoms are located at substitutional lattice sites. Temperature-dependent sheet resistance shows that the insulator-to-metal transition occurs at a Se peak concentration of around $6.3 \times 10^{20} \text{ cm}^{-3}$, proving the formation of an IB in host semiconductors. The correlation between the structural and electrical properties under different annealing processes is also investigated. The results indicate that the degrees of crystalline lattice recovery of the implanted layers and the Se substitutional fraction depend on pulse duration and energy density of the flash. The sample annealed at short pulse durations (1.3 ms) shows better conductivity

than long pulse durations (20 ms). The electrical properties of the hyperdoped layers can be well-correlated to the structural properties resulting from different annealing processes.

KURZFASSUNG

Materialien mit einem Defektband in der Bandlücke (IB) haben ein deutliches Forschungsinteresse hervorgerufen, da sie die Absorption im nahen Infrarot drastisch erhöhen und zu neuen Anwendungen auf dem Gebiet der Photovoltaik und Infrarotdetektion führen können. Die Überdotierung von Si mit tiefen Störstellen ist eine der besten Möglichkeiten, ein IB in Si zu erzeugen.

In dieser Arbeit wird Si mittels Ionenimplantation, gefolgt von gepulster Laserausheilung (PLA) oder Blitzlampenausheilung (FLA), mit Ti oder Chalkogenen dotiert, wobei die Konzentrationen weit oberhalb des Mott-Überganges ($\sim 5 \times 10^{19} \text{ cm}^{-3}$ für Ti) liegen. Die strukturellen und elektrischen Eigenschaften der implantierten Schichten wurden mittels Rutherford-Rückstreu-Spektrometrie und Hallmessungen untersucht.

Im Falle von mit Ti übersättigtem Si wird gezeigt, dass bei hohen Dotierkonzentrationen nach der Flüssigphasenepitaxie und während der schnellen Erstarrung ein als „cellular breakdown“ bekanntes Phänomen auftritt, was den Einbau von Ti in die Si-Matrix verhindert. Der „cellular breakdown“ und die Ausdiffusion kann durch Festphasenepitaxie während der FLA effektiv unterdrückt werden, was zu einem viel höheren Einbau von Ti führt. Weiterhin erschwert die Mikrostruktur des „cellular breakdown“ die Interpretation der elektrischen Eigenschaften. Die Proben bleiben nach der FLA auch bei der höchsten Implantationsfluenz von Ti isolierend, während der Schichtwiderstand nach der PLA mit steigender Ti-Konzentration sinkt. Laut den Ergebnissen der Rasterkraftmikroskopie im leitfähigen Modus (C-AFM) wird der Rückgang des Schichtwiderstandes nach der PLA der Perkolation Ti-reicher Zellwände zugeschrieben, aber nicht dem Isolator-Metallübergang aufgrund der Ti-Dotierung.

Mit Se überdotiertes Si mit verschiedenen Se-Konzentrationen wurde mittels Ionenimplantation, gefolgt von FLA, hergestellt. Die Untersuchungen der strukturellen Eigenschaften der implantierten Schichten haben ergeben, dass die meisten Se-Atome auf substitutionellen Gitterplätzen sitzen. Die temperaturabhängige Messung des Schichtwiderstandes zeigt, dass der Isolator-Metallübergang bei einer Se-Konzentration von ca. $6.3 \times 10^{20} \text{ cm}^{-3}$ stattfindet, was als Nachweis des IB gewertet werden kann. Die Korrelation der strukturellen und elektrischen Eigenschaften unter verschiedenen Ausheilprozessen wurde ebenfalls untersucht. Die Ergebnisse weisen

darauf hin, dass der Umfang der Rekristallisierung und der Anteil von Se auf Gitterplätzen von Pulsdauer und Energiedichte des Blitzes abhängen. Die mit kurzen Pulsen (1.3 ms) ausgeheilte Probe zeigt eine bessere Leitfähigkeit als die bei langen Pulsen (20 ms) ausgeheilte Probe. Die elektrischen Eigenschaften der überdotierten Schicht kann gut mit den strukturellen Eigenschaften, wie sie sich nach den verschiedenen Ausheilprozessen ergeben, korreliert werden.

CONTENTS

Chapter 1 Introduction	1
1.1 Shallow and Deep level impurities in semiconductors.....	1
1.2 Challenges for hyperdoping semiconductors with deep level Impurities	2
1.3 Solid vs. liquid phase epitaxy	5
1.4 Previous work.....	7
1.4.1 Transition metal in Si	7
1.4.2 Chalcogens in Si.....	10
1.5 The organization of this thesis	15
Chapter 2 Experimental methods	18
2.1 Ion implantation.....	18
2.1.1 Basic principle of ion implantation	18
2.1.2 Ion implantation equipment	19
2.1.3 Energy loss.....	20
2.2 Pulsed laser annealing (PLA).....	23
2.3 Flash lamp annealing (FLA)	24
2.4 Rutherford backscattering and channeling spectrometry (RBS/C).....	27
2.4.1 Basic principles.....	27
2.4.2 Analysis of the elements in the target.....	28
2.4.3 Channeling and RBS/C	29
2.4.4 Analysis of the impurity lattice location	31
2.5 Hall measurements	31
2.5.1 Sample preparation	32
2.5.2 Resistivity	32
2.5.3 Hall measurements.....	33
Chapter 3 Suppressing the cellular breakdown in silicon supersaturated with titanium	34
3.1 Introduction	34
3.2 Experimental	35
3.3 Results	36
3.4 Conclusions	42
Chapter 4 Titanium-implanted silicon: does the insulator-to-metal transition really happen?.....	44
4.1 Introduction	44
4.2 Experimental section.....	45
4.3 Results	47
4.3.1 Recrystallization of Ti-implanted Si.....	47

4.3.2 Lattice location of Ti impurities	48
4.3.3 Electrical conduction.....	50
4.3.4 Surface morphology	52
4.3.5 Spatially resolved conduction	53
4.4 Discussion.....	55
4.5 Conclusion	56
Chapter 5 Realizing the insulator-to-metal transition in Se hyperdoped Si via non-equilibrium material processing	57
5.1 Introduction	57
5.2 Experimental	59
5.3 Results	60
5.4 Conclusions	65
Chapter 6 Structural and electrical properties of Se-hyperdoped Si via ion implantation and flash lamp annealing	67
6.1 Introduction	67
6.2 Experimental	68
6.3 Results	69
6.4 Conclusions	76
Chapter 7 Summary and outlook	78
7.1 Summary.....	78
7.2 Outlook.....	81
References	83
Publications	89

Chapter 1 Introduction

1.1 Shallow and Deep level impurities in semiconductors

Doping is used to intentionally introduce impurities into the semiconductor material. It is mainly used to control the optical and electrical properties of the semiconductor [1-5]. Impurities which can be used to control such properties are called dopants. The common dopants for Silicon are Boron, Phosphorus, and Arsenic. The ionized group V elements in silicon or germanium can release electrons and generate conductive electrons and form positive charge centers. Such impurities are called donor impurities or n-type impurities. The energy state of the electrons bound by the donor impurity is called the donor level (see figure 1.1 (a)) which is located at the energy near the bottom of the conduction band. The ionized group III elements in silicon or germanium can accept electrons and generate conductive holes and form negative charge centers. Such impurities are called acceptor impurities or p-type impurities. The energy state of the holes bounded by the impurity is called the acceptor level (see figure 1.1 (b)) which is located at the energy near the top of the valence band. Group V and group III impurities in Si are referred as shallow levels impurities. Shallow level impurities have small ionization of around 10 – 50 meV and can be fully ionized at room temperature.

Different from group V and III impurities, group VI (and some transition metal) impurities in Si usually have ionization energy of 200 – 400 meV. They are regarded as deep level impurities. As we can see from figure 1.1 (c), electrons need to absorb high energy photons to jump from the valence band to the conduction band for pure Si. If we introduce deep level impurities into Si and the doping concentration is high enough, an impurity band or so-called intermediate band (IB) can be formed close to the middle of the band gap. Electron can absorb low energy photons to jump from the valence band to the intermediate band, and then the electron can further absorb another low energy photon to jump from the intermediate band to the conduction band. During this process, the photons at far infrared wavelength can be absorbed.

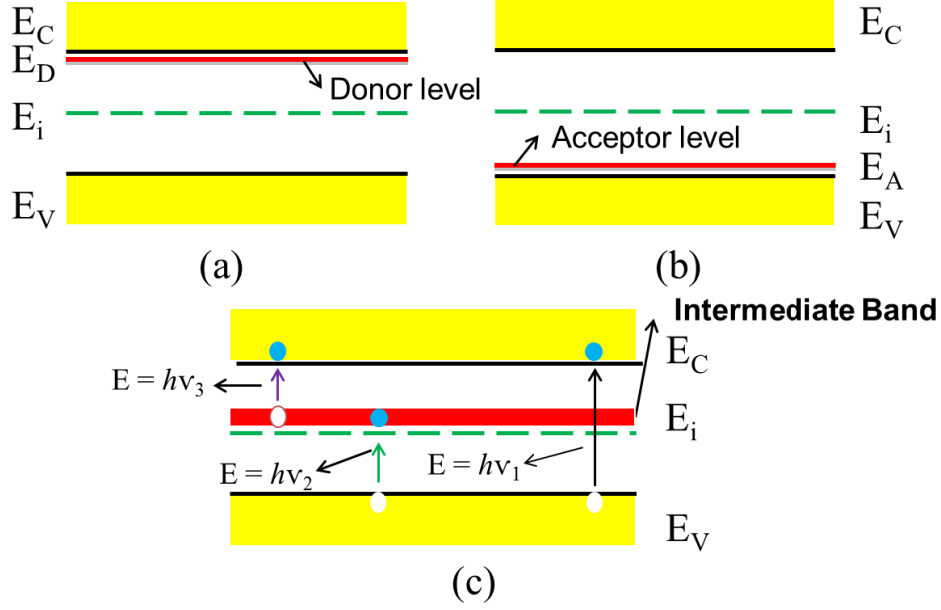


Figure 1.1 Schematics of the electronic bands in semiconductor. Conduction Band (E_C); Valance Band (E_V); Fermi Level (E_i); Donor level (E_D); Acceptor level (E_A).

1.2 Challenges for hyperdoping semiconductors with deep level Impurities

There are some fundamental problems to introduce deep level impurities into Si. One is that impurities have their solid solubility limits in Si. The solid solubility limits of impurities in Si have been extensively studied by many researchers. The solid solubility limits of impurities in Si are shown in figure 1.2. The green part represents the shallow level impurities and the other part represents the deep level impurities. It is found that shallow level impurities have large solid solubility limits, e. g., which for B and As are $4 \times 10^{21} / \text{cm}^3$ and $4 \times 10^{22} / \text{cm}^3$ at high temperature, respectively [6]. In contrast, deep level impurities have much lower solid solubility limits, which are several orders of magnitude lower than those of shallow level impurities. e. g. for S, Se, and Ti are around, $3 \times 10^{16} \text{ cm}^{-3}$, $8 \times 10^{16} \text{ cm}^{-3}$, and $4 \times 10^{14} \text{ cm}^{-3}$ at high temperature, respectively [6-8]. However, the formation of IB in Si requires the doping concentrations to be far exceeding the Mott transition limit for deep level impurities, e. g., $\sim 5 \times 10^{19} \text{ cm}^{-3}$ for Ti [9].

In doped semiconductors the critical carrier concentration corresponding to the insulator-metal transition is usually well described by the Mott formula [10]:

$$p_c^{\frac{1}{3}} a_B = 0.26 \pm 0.05, \quad (1.1)$$

$$a_B = \frac{e^2}{8\pi\epsilon_0\epsilon_r E_I}, \quad (1.2)$$

where a_B is the effective Bohr radius, p_c is the critical hole concentration, e is the charge of single electron, ϵ_r is the static dielectric constant, ϵ_0 is the vacuum permittivity, and E_i is the impurity binding energy. For deep level impurities, E_i is in the range of several hundreds meV, the critical concentration p_c is in the range of $10^{20} - 10^{21} \text{ cm}^{-3}$.

Therefore, it is very difficult to introduce deep level impurities into silicon in doping concentrations above the Mott transition limit by equilibrium methods. Other doping techniques are required to achieve the high concentrations for impurities that have low equilibrium solubilities in silicon. As an industry-standard method, ion implantation works in non-thermal-equilibrium regime and can overcome the thermal solubility limit.

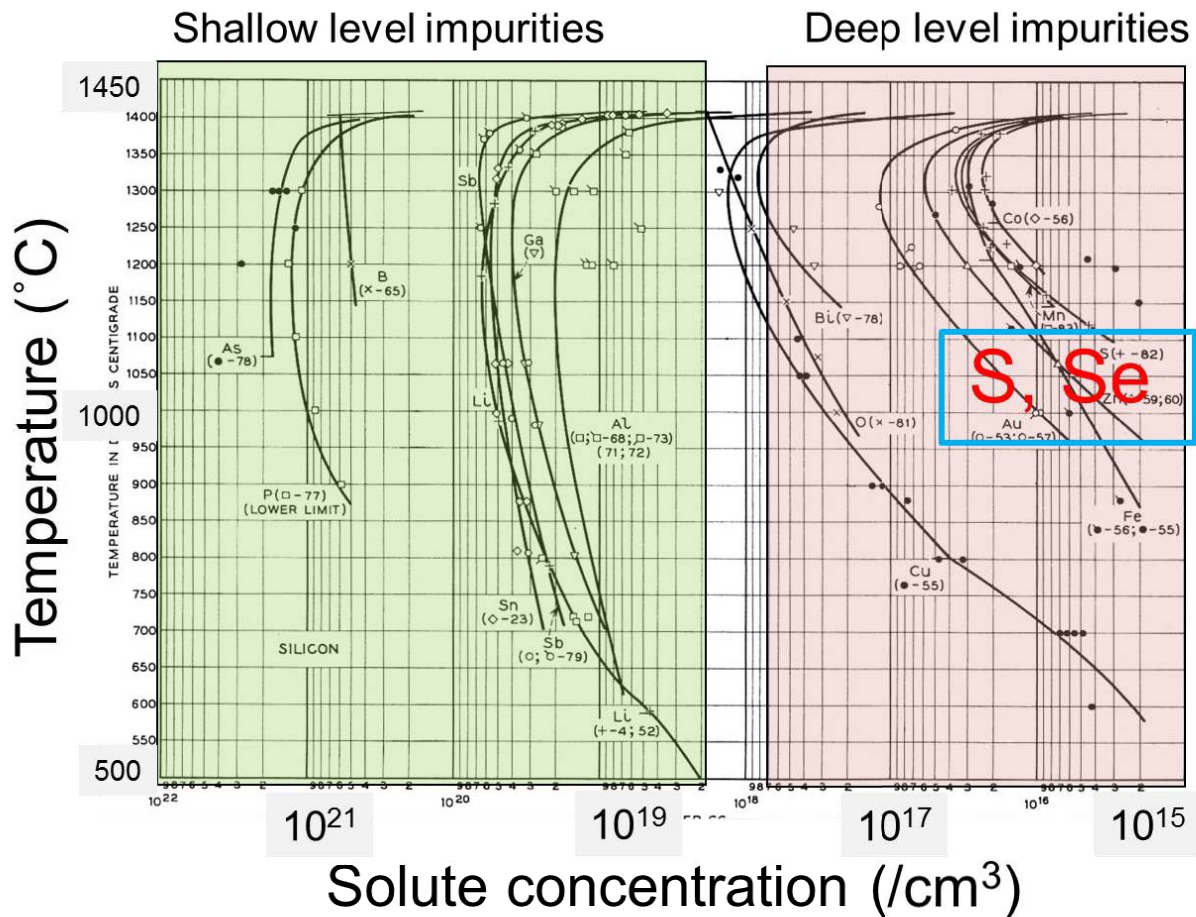


Figure 1.2 Solid solubility limits of impurities in Si. For most transition metals and group VI elements, the solubility limits are much smaller compared. The solid solubility limits for S and Se is $3 \times 10^{16} \text{ cm}^{-3}$ and $8 \times 10^{16} \text{ cm}^{-3}$, respectively [6,7]. Adapted from ref. [7].

Another problem is that the deep level impurities have high diffusivity. Fig. 1.3 shows the diffusion coefficient of impurities in Si. We can see that deep level impurities have larger diffusion coefficient than those of shallow level impurities. For instance, the diffusion coefficient of P is $\sim 10^{-14}$ cm²/sec, whereas Ti is around 6×10^{-10} - 4×10^{-9} cm²/sec in the temperature range from 1000 °C to 1250 °C. Even though deep level impurities can be introduced into Si, there are problems for the following sample annealing. The impurities will diffuse to the sample surface or deeper into the sample if the annealing time is too long. This presents the challenge that we cannot anneal the sample for long time. However, this problem can be partially solved by pulsed laser annealing which brings the sample to liquid phase. The cooling down procedure is very fast during the rapid solidification. So the impurities can be trapped in the Si matrix in the case that the regrowth velocity is larger than the diffuse velocity. The detailed information about how to trap impurities into Si will be described in the following part.

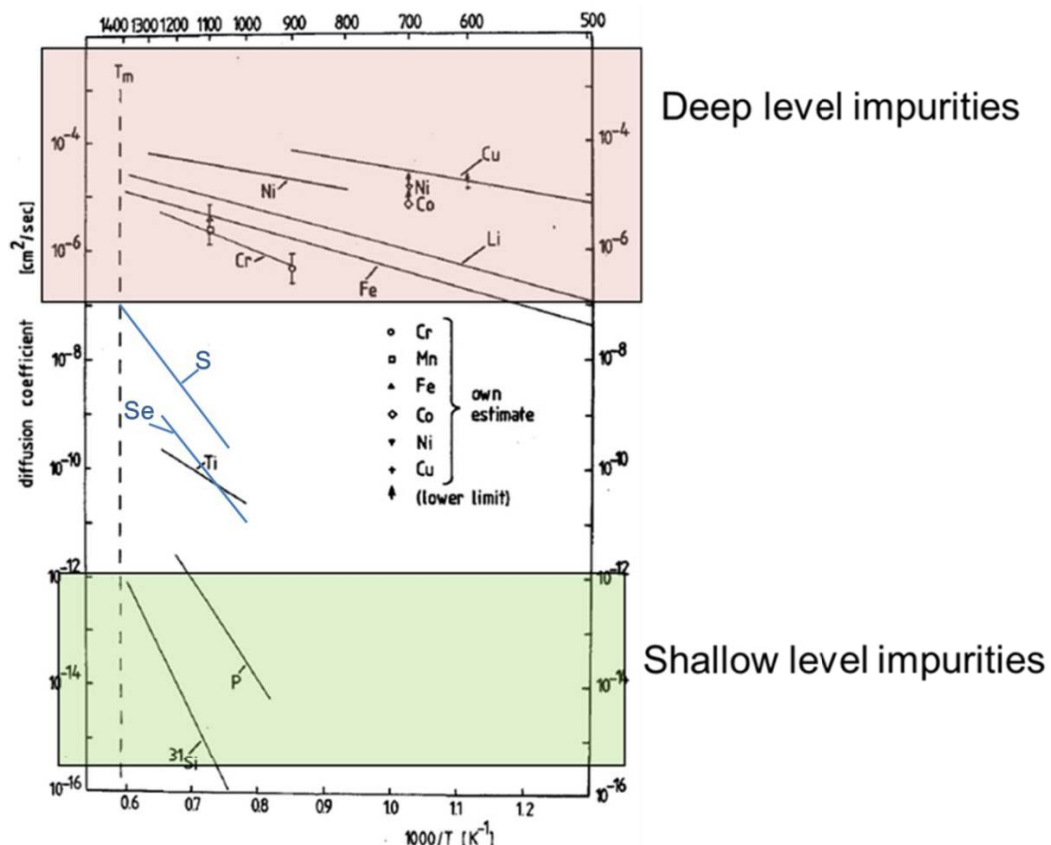


Figure 1.3 Diffusion coefficient of impurities in Si. Adapted from ref. [11]. The diffusion coefficient of S in Si is $7.1 \times 10^{-9} - 1.8 \times 10^{-7}$ cm²/sec in the temperature range from 1055 °C to 1398 °C, Se is $1.1 \times 10^{-11} - 1.0 \times 10^{-9}$ cm²/sec in the temperature range from 1005 °C to 1263 °C [12,13].

1.3 Solid vs. liquid phase epitaxy

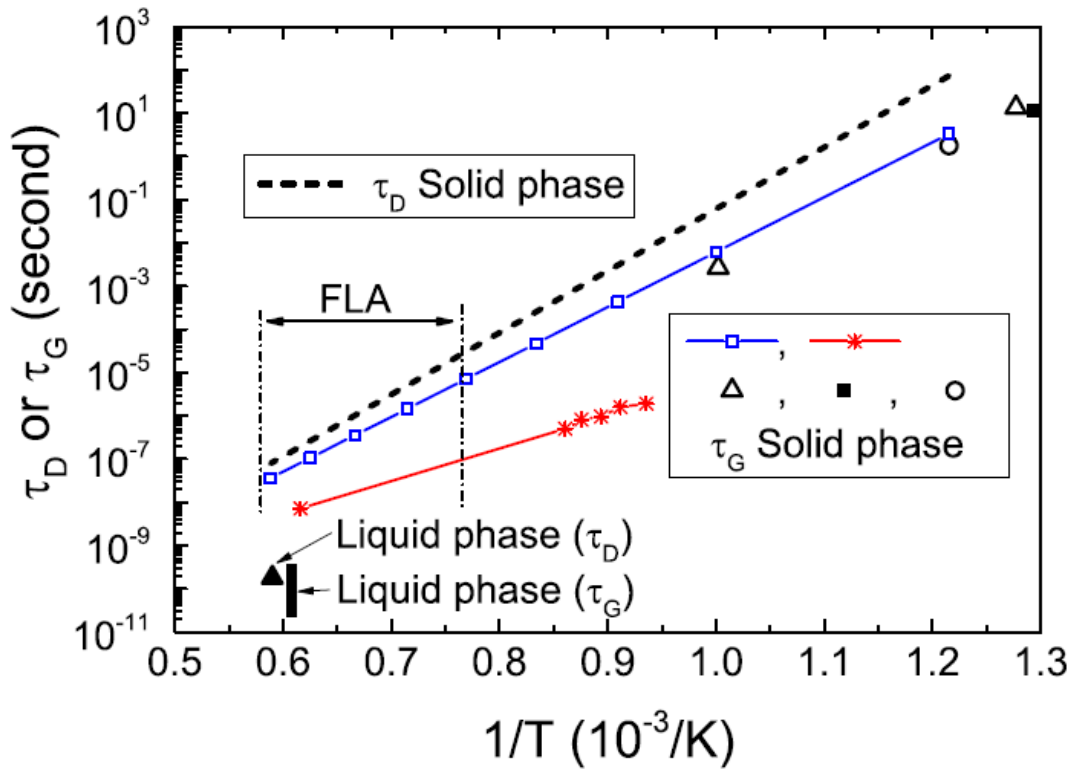


Figure 1.4 Competition between the Si recrystallization and selenium diffusion characterized by the time needed to regrow (τ_G) or diffuse (τ_D) one monolayer. The dashed line is τ_D in solid phase according to the diffusion parameter in Ref. [14]. The other lines or symbols are τ_G according to different references: open blue square [16], red star [17], open triangle [18], solid square [19], open circle [15]. Despite the possible uncertainty of the regrowth velocity, τ_G is smaller than τ_D . That means it is possible to trap selenium and realize metastable, selenium over-saturated Si layer. The vertical dashed and dotted lines indicate the working regime of flash lamp annealing (FLA). The reported τ_D is shown as a solid triangle [20] and τ_G is shown as a vertical thick line by assuming the growth velocity of 1–10 m/s for pulsed laser annealing (PLA). From ref. [21].

We try to characterize the competition between the solute trapping and diffusion by estimating the time needed to regrow (τ_G) or to diffuse (τ_D) over a Si monolayer (0.27 nm). In other words, the speed of the resolidification and the speed at which the impurity atoms can move determine how likely they will stay ahead or be trapped by the moving amorphous/crystalline interface. If τ_D is larger than τ_G , the dopants are able to be trapped in the crystalline matrix. In figure 1.4 we compare τ_G and τ_D estimated from data published in literature. τ_D is calculated according to the data in

ref. [14]. The large uncertainty in τ_G comes from the large scattering in the regrowth velocity, which exhibits different values reported by various groups [15, 16-19]. However, as shown in figure 1.4, in solid phase Si τ_D is generally larger than τ_G . That means selenium impurities can be trapped in the Si matrix if an optimized thermal treatment is applied even in solid phase processing. Particularly in the low temperature regime, τ_D is much larger than τ_G , which well explains the realization of doping above solubility limit by low temperature annealing [15].

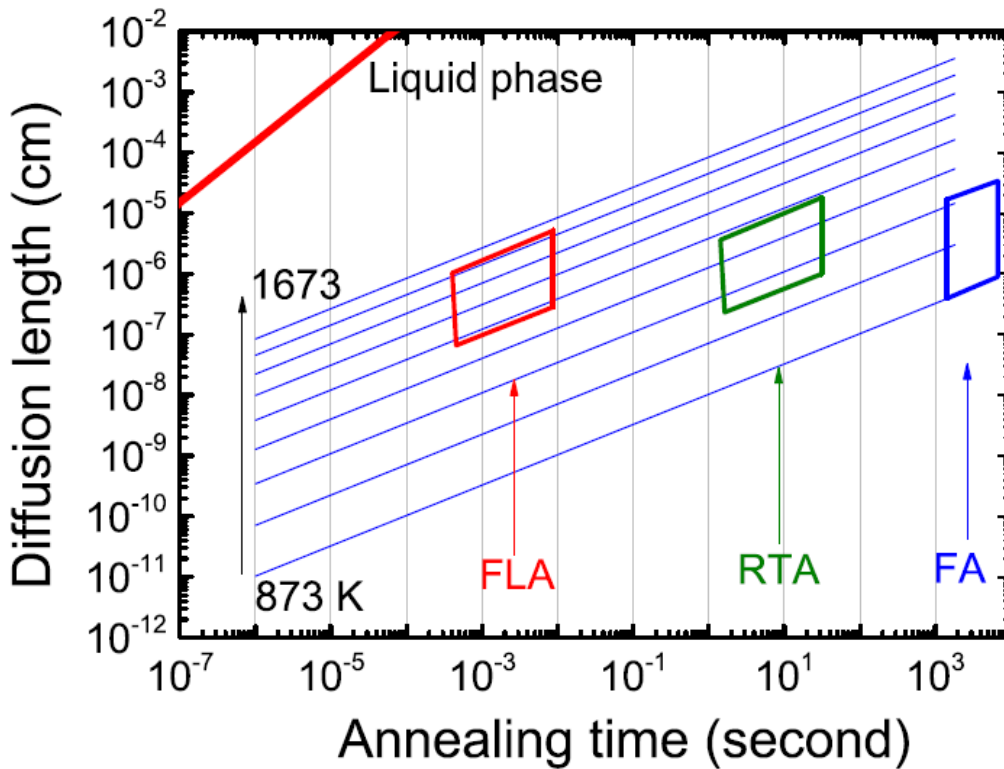


Figure 1.5 Selenium diffusion length (L) in Si at different temperature vs. time duration. The three boxes indicate the working regime of different thermal process in solid phase: low temperature furnace annealing (FA) for more than 1000 second, rapid thermal annealing (RTA) for seconds and flash lamp annealing (FLA) for milliseconds at high temperature. The diffusion length of selenium in liquid phase is also shown for comparison. From ref. [21].

Another criterion to be considered is the annealing duration. In the regrown metastable layer, the impurity concentration is much above the thermal equilibrium solubility limit. During the prolonged annealing to finish the regrowth completely, the metastable solubility returns to the equilibrium value as dopants come out of their substitutional positions. This has been observed in sulfur hyperdoped Si [22]. The decrease in the substitutional fraction with increasing dopant concentration is due to

incipient precipitation [23]. For a first approximation, the metastable phase does not precipitate if the mean diffusion length of the impurity at the annealing temperature is less than their average distance. For a diffusion length larger than the average impurity distance, there is a finite probability of nucleation of a secondary phase or dimers. Therefore, the diffusion length $L = (2Dt)^{1/2}$, D being the diffusion coefficient [14] and t the annealing time, must be relatively short in order to achieve a high concentration of dopants on the substitutional sites. We illustrate the estimated results in figure 1.5, in which the working regimes of furnace annealing (FA), rapid thermal annealing (RTA) and flash lamp annealing (FLA) are indicated. In the case of FA at low temperature (around 500 °C), an annealing duration more than 1000 s is needed to regrow the whole layer. A longer annealing time and a slightly higher annealing temperature strongly increase the diffusion length. From figure 1.5, an annealing processing in millisecond or microsecond while keeping the system in solid phase could result in a minimized diffusion length.

1.4 Previous work

1.4.1 Transition metal in Si

Recently, hyperdoped silicon with Ti has been studied extensively and has emerged as a promising candidate for the so-called intermediate band solar cell [20, 24-26] and infrared photodetectors [20, 27] since it can form an IB. Ion implantation with pulsed laser annealing (PLA) is usually used to introduce Ti into Si and can overcome the equilibrium solid solubility limit. The structural and electrical properties of Ti implanted Si annealed by PLA have been studied by several groups. For instance, Olea *et al.* found evidence for the existence of IB in the Si implanted with Ti at doping concentration above the Mott limit [28]. In their work, n-type single crystal Si wafers ($\rho = 200 \Omega \text{ cm}$; $\mu = 1250 \text{ cm}^2 \text{ V}^{-1} \text{ s}^{-1}$; $n = 2.2 \times 10^{13} \text{ cm}^{-3}$ measured at 300 K) were implanted with Ti ions at 30 keV, with three different doses: 10^{15} , 5×10^{15} and 10^{16} cm^{-2} . Then, the implanted Si samples were annealed by PLA with one 20 ns long pulse of a KrF excimer laser (248 nm) at energy densities from 0.2 to 0.8 J cm^{-2} . The temperature-dependent sheet resistance for samples unimplanted and implanted with different fluences before and after PLA is shown in figure 1.6. The sheet resistance of all implanted samples is higher than that of Si substrate at temperatures

below 180 – 190 K. They attributed this phenomenon to the appearance of an electrical decoupling between the substrate and the Ti implanted layer in this temperature range. They assumed that IB exists in the Ti implanted layer and the critical impurity density needs to be above the Mott transition limit of $5.9 \times 10^{19} \text{ cm}^{-3}$. The Ti doping concentration exceeds the Mott limit for all implanted samples in this work. The delocalization of the electron wavefunctions of impurity happens, resulting in the formation of IB in the Ti implanted layer.

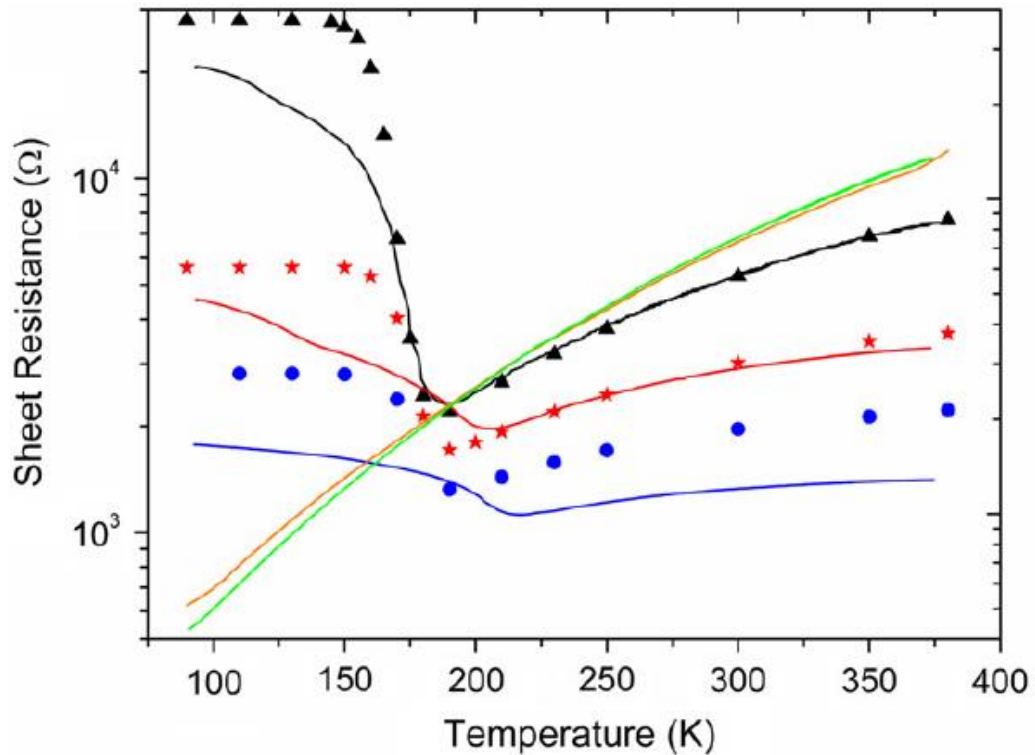


Figure 1.6 Sheet resistance as a function of the measured temperature for the n-Si substrate (yellow line), for a PLM annealed n-Si substrate (green line) and double sheet Ti implanted layer (TIL)/n-Si substrate for different implantation doses: 10^{15} cm^{-2} (black line: experimental; ▲ Argonne Tandem Linear Accelerator System (ATLAS) simulation); ★ $5 \times 10^{15} \text{ cm}^{-2}$ (red line: experimental; ATLAS simulation) and 10^{16} cm^{-2} (blue line: experimental; ● ATLAS simulation). From ref. [28]

Pastor *et al.* reported that Ti atoms are located at interstitial lattice sites in Ti-hyperdoped Si [29]. They used ion implantation followed by pulsed laser annealing to fabricate Si doped with Ti in concentrations exceeding the equilibrium solid solubility limit. In this work, the implantation was done at 33 keV with Ti fluences of 10^{15} , 5×10^{15} , 10^{16} , and $5 \times 10^{16} \text{ cm}^{-2}$, respectively. After implantation, samples were PLA

processed with a KrF excimer laser (248 nm) at 0.2 and 0.8 J/cm² with a single pulse of 20 ns. The authors were using channeling Rutherford backscattering spectrometry (cRBS) to detect the lattice location. The RBS spectra about the Ti related peaks for the Ti implanted samples with fluence of 10¹⁵ cm⁻² and PLA annealed at 0.2 and 0.8 J/cm² at random and channeling condition are shown in Figure 1.7. As can be clearly seen, there is no significant difference for the Ti peaks between the random and channeling configurations, pointing out that most of the Ti atoms are located at interstitial lattice sites in the host Si matrix. The Ti interstitial fraction is more than 95%. Moreover, theoretical calculations predict that the formation of IB inside the Si requires the Ti impurities to be in interstitial lattice sites [30].

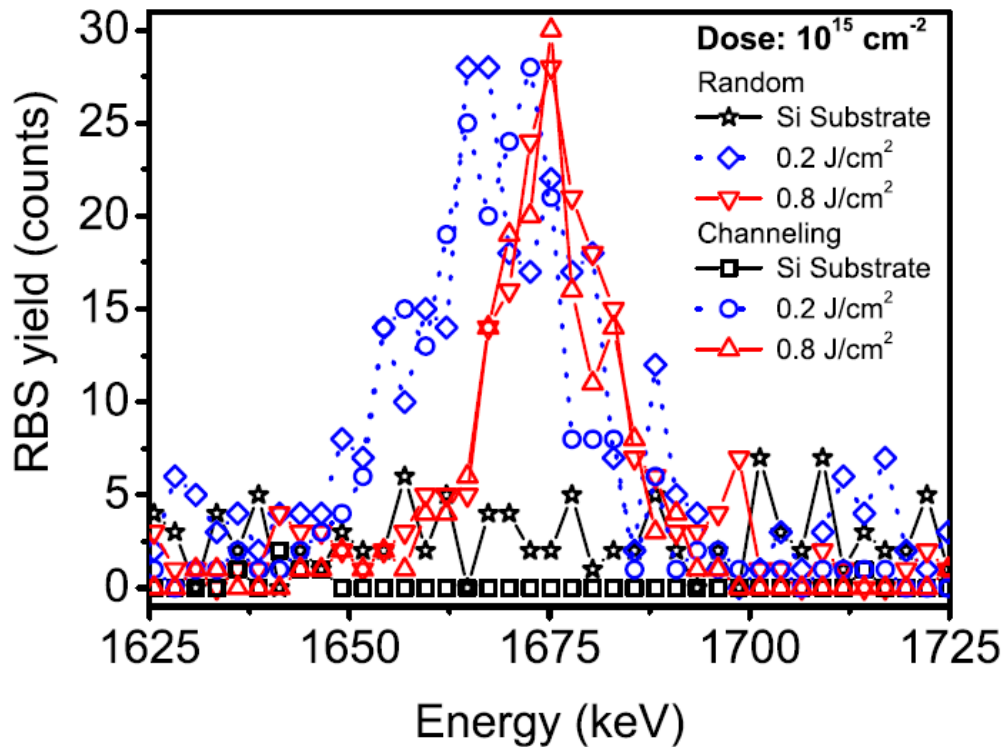


Figure 1.7 RBS spectra centered at the Ti peak signal for the Si samples implanted with 10¹⁵ cm⁻² at energy of 33 keV and PLM processed at 0.2 and 0.8 J/cm² at random and channeling configuration. RBS spectra of the Si substrate sample are also shown. From ref. [29].

Mathews *et al.* pointed out that the intrinsic incorporation limit of the Ti concentration in Si is around 1~2×10²¹ cm⁻³ without phase separation [31]. In their experiment, p-Si (111) layers with Ti levels well above the solid solubility limit was achieved via ion implantation of 15 keV ⁴⁸Ti at fluences of 10¹² to 10¹⁶ cm⁻² followed by PLA using a Nd:YAG laser (FWHM = 6 ns) operating at 355 nm. All implanted

layers were examined by transmission electron microscopy (TEM) as shown in figure 1.8. For the sample with doping fluence of $3 \times 10^{15} \text{ cm}^{-2}$ the implanted layer can be well recrystallized which can be seen in figure 1.8 (b). It shows a single crystalline structure with stacking faults. However, for the sample with the high doping fluence of $1 \times 10^{16} \text{ cm}^{-2}$, a cellular breakdown instead of stacking faults is formed in the implanted layer due to the interface instability during resolidification, which is shown in the figure 1.8 (a). Therefore, an incorporation limit for Ti incorporated into the single-crystalline Si matrix. If the doping concentration is too high, the cellular breakdown will occur. The incorporated concentration will not be able to exceed the Mott limit due to the diffusion of Ti atoms.

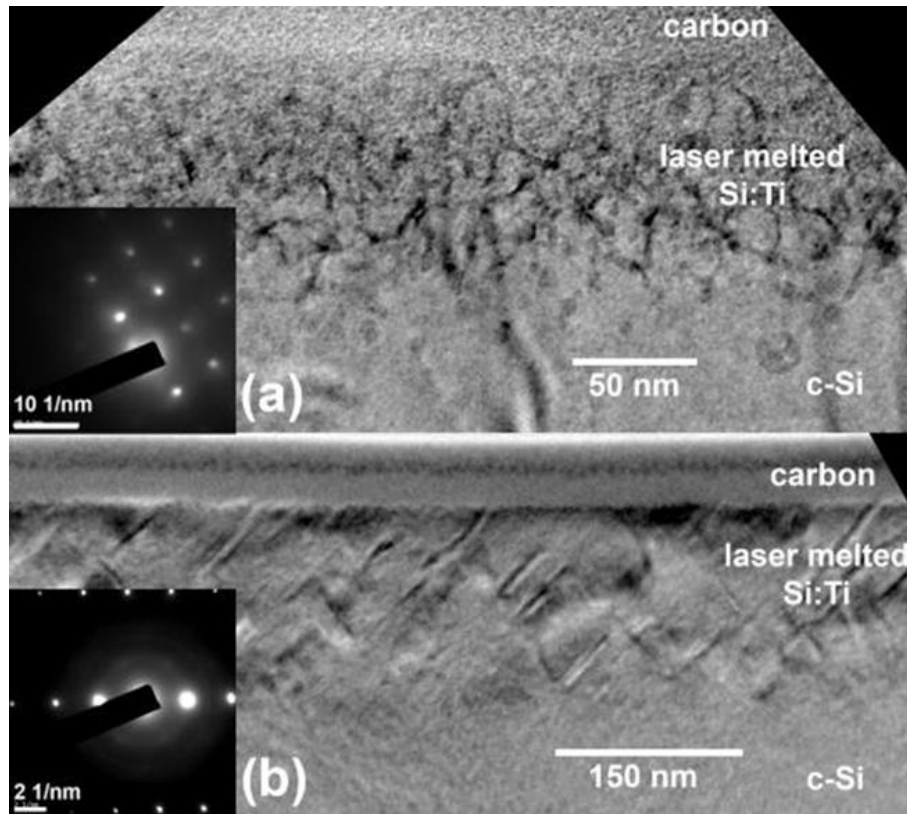


Figure 1.8 Cross-section TEM micrographs of p-Si (111) implanted with 15 keV Ti at doses of $1 \times 10^{16} \text{ cm}^{-2}$ (a) and $3 \times 10^{15} \text{ cm}^{-2}$ (b) and laser melted at a fluence of 0.75 J/cm^2 . Insets are their respective diffraction patterns. From ref. [31].

1.4.2 Chalcogens in Si

Silicon supersaturated with chalcogens has shown great potential application in infrared photodetectors [32-34] and IB solar cells [26, 35-37] by virtue of their unique

optical and electrical properties. These applications require the formation of an IB inside Si. The extra electrons introduced through doping can extend the absorption wavelength. Insulator-to-metal transition (IMT) provides an evidence for the formation of IB.

Kim *et al.* found a strong sub-band gap absorption in the wavelength range 1200–2500 nm in Si supersaturated with S which was fabricated by ion implantation and subsequently pulsed laser melting [27]. In their work, Si (111) (n-type, P-doped, 1.2 k Ω cm, 300 μ m thick) wafers were implanted with S at 200 keV to a fluence of 1×10^{16} cm⁻². The ion implanted samples were laser annealed by a spatially homogenized pulsed XeCl⁺ excimer laser beam [308 nm, 25 ns of full width at half maximum (FWHM), 50 ns total pulse duration] with fluences of 1, 1.4, or 1.8 J/cm². The optical absorption spectra of the bare Si, as-implanted, and implanted samples irradiated by PLA are shown in figure 1.9. A strong and broad sub-band-gap absorption over the wavelength range 1200 – 2500 nm is observed in all samples irradiated by PLA. Compared with samples irradiated with lower or higher fluences, the 1.4 J/cm² irradiated sample has the largest absorptance. They determined the sulfur concentration-depth profiles by secondary ion mass spectroscopy (SIMS). They found that the 1.4 J/cm² irradiated sample can result in the largest sulfur concentration at 3×10^{20} at. /cm³ which is far exceeding the maximum solubility limit. They concluded that the occurrence of sub-band-gap optical absorption is due to the formation of an impurity band at high S doping concentration.

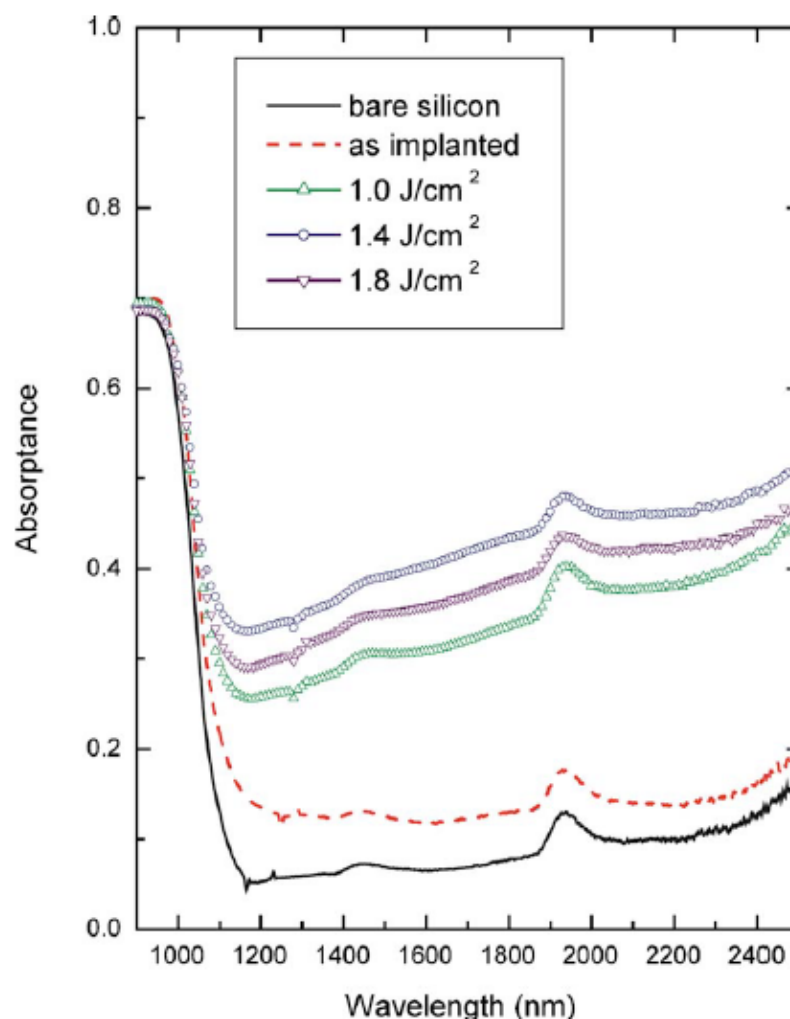
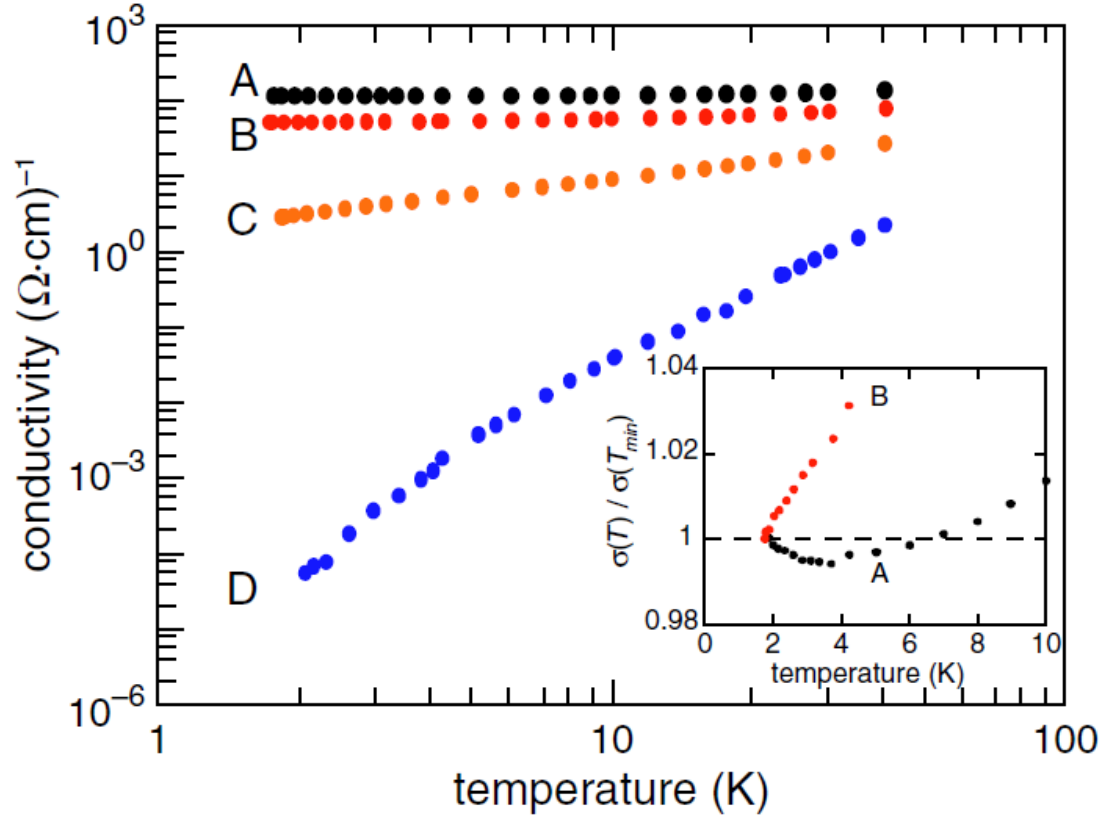


Figure 1.9 IR absorbance data from samples irradiated with 1.0, 1.4, and 1.8 J /cm²; as implanted (---) and bare silicon (—). The peak at ~1900 nm is from water. Si was implanted with S for fluence of 1×10^{16} cm⁻² at energy of 200 keV. From ref. [27].

Winkler *et al.* reported that the insulator to metal transition (IMT) occurs in crystalline silicon doped with sulfur at concentration above the Mott limit by ion implantation and pulsed-laser melting [38]. In this work, p-type single-crystal Si wafers (boron doped, $\rho \approx 25 \Omega \cdot \text{cm}$) were ion-implanted, nominally with S ions at 95 keV to fluences of $(3, 7, 9, \text{ and } 10) \times 10^{15} \text{ cm}^{-2}$. The implanted samples were melted using XeCl⁺ excimer laser pulses (fluence=1.7 J·cm⁻², $\lambda=308 \text{ nm}$, pulse duration 25 ns full-width at half-maximum) in ambient conditions. The temperature dependent conductivity for all samples is shown in figure 1.10. The conductivities of sample C and D sharply increase with the increasing of temperature at low temperature region, indicating that they are thermally activated and are insulators. For samples A and B, their conductivities only slightly change with the change of

temperature. They show finite conductivities and exhibit a metallic-like behavior as the temperature approaches zero. As shown in the inset to figure 1.10, a slightly negative temperature coefficient which is expected to appear in the metal is clearly seen for sample A. A positive temperature coefficient occurs in sample B, indicating that it is a just-metallic semiconductor and not a typical metal. Therefore, IMT happens between sample A and B. Moreover, Ertekin *et al.* proved that the IMT occurs in selenium-hyperdoped Silicon at Se peak concentrations between $1.4 \times 10^{20} \text{ cm}^{-3}$ and $4.9 \times 10^{20} \text{ cm}^{-3}$ by combining theory and experiment [39]. Figure 1.11 shows the temperature-dependent conductivities for the two samples with peak Se concentrations of $1.4 \times 10^{20} \text{ cm}^{-3}$ and $4.9 \times 10^{20} \text{ cm}^{-3}$, respectively. The conductivity of the sample with low doping concentration is very sensitive to temperature, which is almost 5 orders of magnitude smaller than that of the sample with high doping concentration at 1.8 K. However, the conductivity shows almost no change as the temperature approaching 0 K for the highly doped sample. Therefore, an IMT occurs at a concentration between $1.4 \times 10^{20} \text{ cm}^{-3}$ and $4.9 \times 10^{20} \text{ cm}^{-3}$. The inset in figure 1.10 shows the analysis using density functional theory (DFT). The defect bands become broader with the increase of doping concentration. Defect bands are combined with the conduction bands when the Se content is larger than 0.25%, indicating that IMT arises in Se highly doped Si. The theoretical prediction corresponds well to the experimental results.



Sample	Φ (10^{15} cm^{-2})	c_{pk} (10^{20} cm^{-3})	d_{eff} (nm)	T_0 (K)	σ_0 ($\Omega \cdot \text{cm}$) $^{-1}$
A	9 ± 2	3.6 ± 0.7	250
B	10 ± 2	3.8 ± 0.8	260
C	4.3 ± 0.9	2.2 ± 0.4	250	9.05	3.20
D	3.0 ± 0.6	1.2 ± 0.2	260	326.5	2.46

Figure 1.10 Conductivity of S-doped Si for temperatures $1:7 \text{ K} < T < 40 \text{ K}$. Sample properties are given in Table I. Inset, sample A exhibits a negative temperature coefficient. From ref. [38]. In the table, Φ : sulfur fluence, c_{pk} : peak sulfur concentration, and $d_{\text{eff}} = \Phi/c_{\text{pk}}$: effective layer depth.

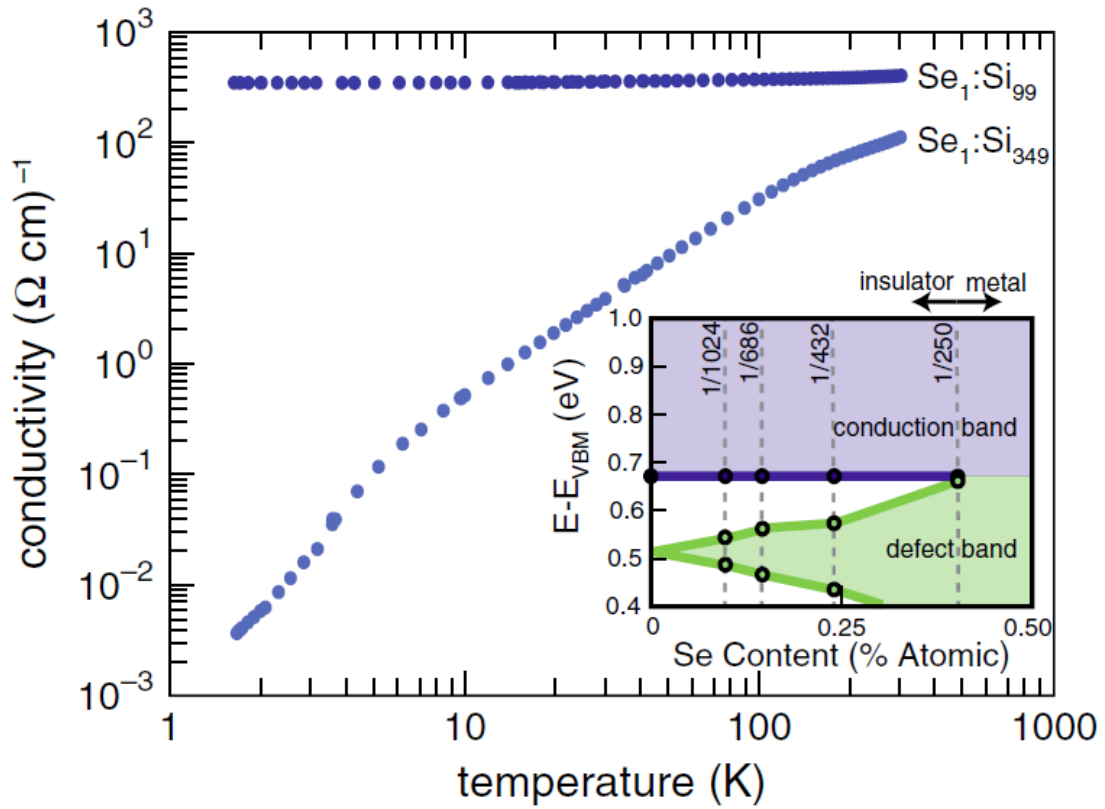


Figure 1.11 Temperature-dependent conductivity of Se-hyperdoped silicon. At peak Se concentrations of $\text{Se}_1\text{:Si}_{349}$ ($1.4 \times 10^{20} \text{ cm}^{-3}$) hyperdoped Si exhibits strongly temperature-dependent conductivity, indicative of the insulating phase. At higher concentrations of $4.9 \times 10^{20} \text{ cm}^{-3}$ ($\text{Se}_1\text{:Si}_{99}$), the conductivity is comparatively insensitive to temperature down to $T = 1.8 \text{ K}$, indicating a dopant-induced transition to the metallic state. Inset: Analysis using density functional theory (DFT) indicates that the conduction and defect bands cross as the Se-dopant concentration increases. Conduction and defect band edges are demarked by DFT's Kohn-Sham eigenvalues for the insulating systems; with energies referenced to the valence band maximum E_{VBM} . From ref. [39].

1.5 The organization of this thesis

In this thesis, we mainly discuss the fabrication of Ti and Se hyperdoped Si by ion implantation followed by pulsed laser annealing or flash lamp annealing. These two kinds of materials have promising applications in infrared photodetectors and high-efficient solar cells due to their novel optical and electrical properties. As mentioned above, in the previous research work, Ti could already be incorporated in a concentration above the Mott limit by liquid phase epitaxy. However, there are still problems, e. g. when the doping concentration is high, the dopant segregation and

cellular break down will happen due to the interface instability during liquid phase epitaxy. FLA in millisecond range can render the temperature of the sample just slightly below the melting temperature leading to solid phase epitaxy. Thus, we think about the possibility of incorporating Ti into Si with high doping concentration by solid phase epitaxy. For the electrical properties of Ti doped Si, the published results show that electrical conduction from the intermediate band formed inside Si is due to the Ti incorporated into Si. However, the question is whether the electrical conduction is really from the dilute Ti doped Si? Even though hyperdoped Si with chalcogens prepared by ion implantation and followed by FLA has already been studied in several works, the detailed structural and electrical properties of chalcogen implanted Si processed by FLA are still not clear.

In Chapter 2, the experimental techniques used in this thesis are introduced, i.e., ion implantation combined with pulsed laser annealing or flash lamp annealing. Rutherford backscattering spectrometry measurements and Hall measurements are used to characterize the structural and electrical properties of the implanted layer are briefly reviewed.

In Chapter 3, we prepare the single crystalline Si doped with Ti concentration above the Mott concentration limit by ion implantation and followed by pulsed laser annealing or flash lamp annealing. The microstructures caused by liquid phase epitaxy and solid phase epitaxy are compared in this work.

In Chapter 4, we present the work about Ti-hyperdoped Si fabricated by ion implantation followed by PLA and FLA. In this work, we investigate the lattice location of Ti in Si sites and the influence of the cellular breakdown on the electrical properties. The results show that Ti atoms locate at neither interstitial nor substitutional sites in Si and the conduction percolation at high Ti concentration is responsible for the metallic-like conductivity.

In Chapter 5, we investigate the structural and electrical properties of Se-hyperdoped Si layers. We find that most Se atoms are incorporated on substitutional Si sites. We observe an IMT at the Se doping concentration above a critical concentration.

In Chapter 6, we present the degree of crystalline lattice recovery of Se implanted layers after FLA and the relationship between the Se substitutional fraction and the pulse duration of FLA. We also show a correlation between the structural and the electrical properties under different annealing processes.

In Chapter 7, I summarized all the results. In addition, I also gave some ideas worth being further investigated.

Chapter 2 Experimental methods

2.1 Ion implantation

During ion implantation, a beam of ions is directed to a solid material in vacuum. The ions slow down with losing energy and eventually stay in the solid material. Impurities introduced by ion implantation can change the optical and electrical properties of the solid. Compared with equilibrium techniques, ion implantation works in the non-thermal-equilibrium regime. Ion implantation has become an industry-standard method in semiconductor manufacturing due to its advantages in practical applications, for instance, very high reproducibility, good homogeneity, good control of doping concentration and implantation depth. However, ion implantation is a highly destructive process. The energy loss by the energy transfer between ion and host atoms induces a large number of defects, e.g. vacancies and interstitials. Therefore, the pre-existing crystal order is seriously damaged and the implanted layer can become amorphous and a thermal post-preheating is needed.

2.1.1 Basic principle of ion implantation

Ions with certain charges are accelerated by the acceleration field. The direction of the movement of the ions is changed under the action of the magnetic field. After the high energy ions are injected into the target, a series of collisions occur between the ions and the host atoms. The energy of ions gradually reduces and loses finally with ions stopping in the host matrix. Therefore, a certain impurity distribution can be formed. The distribution depth of impurities is related to the particle fluence and the crystal orientation of the substrate. The implantation depth of impurity depends on the implanted energy and the mass of impurity. The concentration of impurities is proportional to the implanted fluence.

2.1.2 Ion implantation equipment

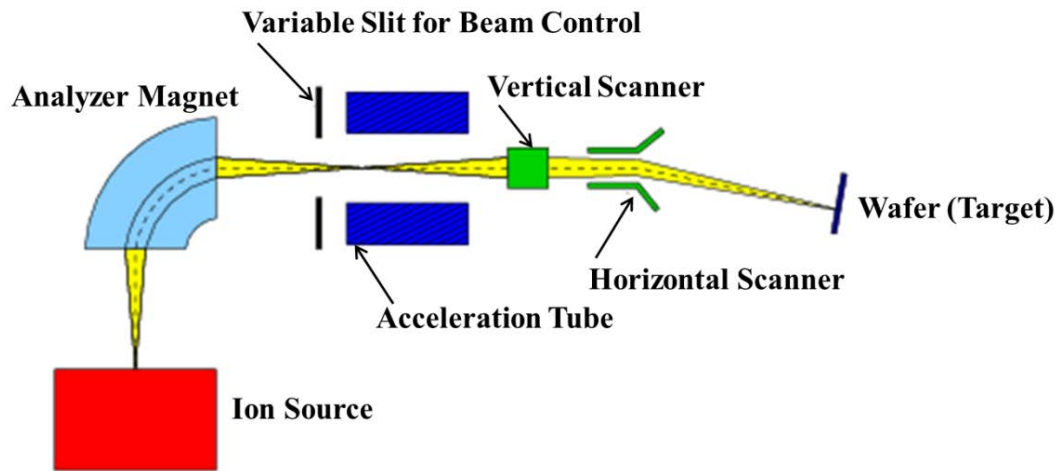


Figure 2.1 Schematic of ion implantation equipment. The figure is from ref. [40].

A general schematic of ion implantation process is shown in Figure 2.1. The ion implanter is mainly composed of the following parts: (1) an ion source; (2) an analyzer magnet; (3) a variable slit for beam control; (4) an acceleration tube; (5) a vertical scanner and a horizontal scanner; (5) a target chamber; and (6) a vacuum system.

The ion source can be used to isolate impurities and generate the desired positive or negative ion species. The mixed ion beam deflects after passing through the analyzer magnet which is used for ion screening and is the main component of the ion implantation system. The ions with large charge-to-mass ratio are bombarded to the outer wall of the analyzer magnetic field. Ions with too small or large charge-to-mass ratio are bombarded to the inner wall of the analyzer magnetic field and only ions with a specific charge-to-mass ratio can pass through this region. The ions with charge are accelerated by the high electric field to obtain a certain amount of energy and then go towards the target. The accelerated ions are focused on an ion beam with several millimeters of diameter by a variable slit for beam center. On the way to the target, the horizontal and vertical scanning systems scan the ion beam in a certain area of x and y directions. The target is placed in a chamber. The whole device of ion implantation is maintained in vacuum.

The parameters of ion implantation are the ion species, the implantation fluence, the implantation energy, tilt and twist angles and temperature. The implantation energy is chosen depending on the required depth of the implanted ions. The angle

between the wafer surface normal and the ion beam should be finite in order to avoid channeling effects in crystalline silicon.

2.1.3 Energy loss

When an energetic ion penetrates a solid, the ion will undergo a series of collisions with the host atomic nuclei and electrons. Energy is lost in two mechanisms during this process. Through elastic nuclear interaction, the energy is transferred from incoming ions to host atoms. In inelastic collisions, the energy is transformed by the lattice vibration and the ionization of the host atoms.

The incident ion loses its energy and stops at certain depth in the host matrix due to the collision mentioned above. The energy loss per unit penetration depth is given by the stopping force.

$$S(E) = \frac{dE}{dx}, \quad (2.1)$$

where E is the energy of the incident ion, and x is the path length. $S(E)$ is the average delivered energy when summed over all probabilities of each scattering process.

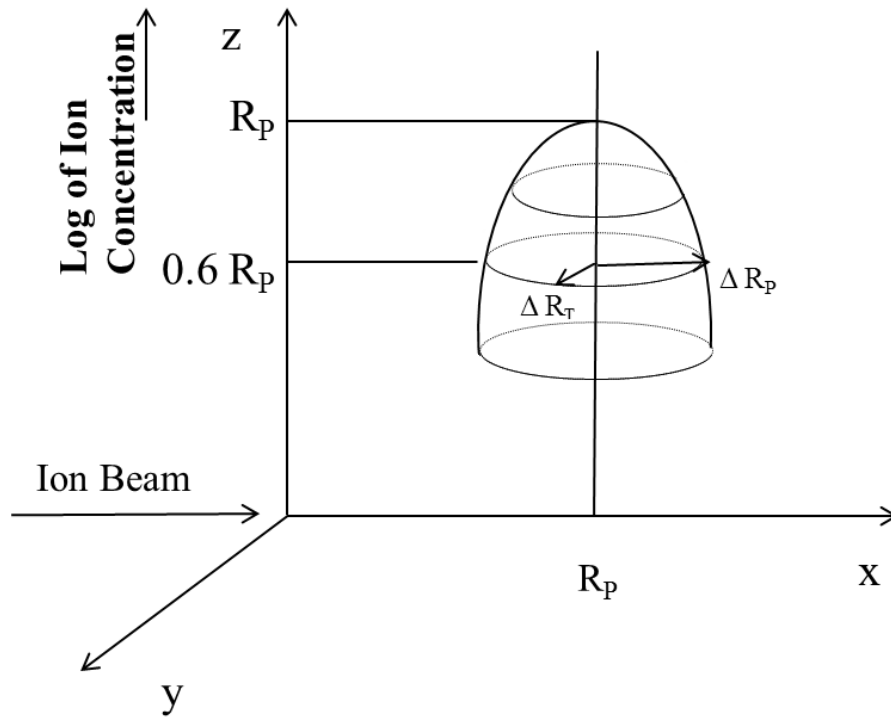


Figure 2.2 Schematic of the Gaussian concentration distribution for ion implantation. From ref. [41].

In 1963 Lindhard, Scharff and Schiott first established a theory of ion distribution in a target during ion implantation, referred to as LSS theory [42]. The LSS theory mainly described the depth profile of the implanted ions in a Gaussian range distribution in an amorphous target. The related parameters are the average projected range R_p and the standard deviation ΔR_p .

Figure 2.2 shows a Gaussian range distribution profile for implanted ions. The equation of the Gaussian concentration distribution for implanted ions in the amorphous target can be expressed as:

$$N(x) = \frac{\Phi}{\sqrt{2\pi}\Delta R_p} \exp\left[-\frac{(x-R_p)^2}{2(\Delta R_p)^2}\right], \quad (2.2)$$

where x is the depth of penetration from the sample surface, Φ is the implantation fluence, R_p is the average projected range, ΔR_p is a projected straggle, and ΔR_T is transverse straggle.

The maximum doping concentration of ion implantation N_{max} can be calculated as:

$$N_{max} = \frac{\Phi}{\sqrt{2\pi}\Delta R_p} \approx \frac{0.4\Phi}{\Delta R_p}, \quad (2.3)$$

From the above formula, it can be seen that the peak concentration of the implanted ions is related to the implantation fluence. The maximum concentration is located at R_p , which is shown in the concentration profile.

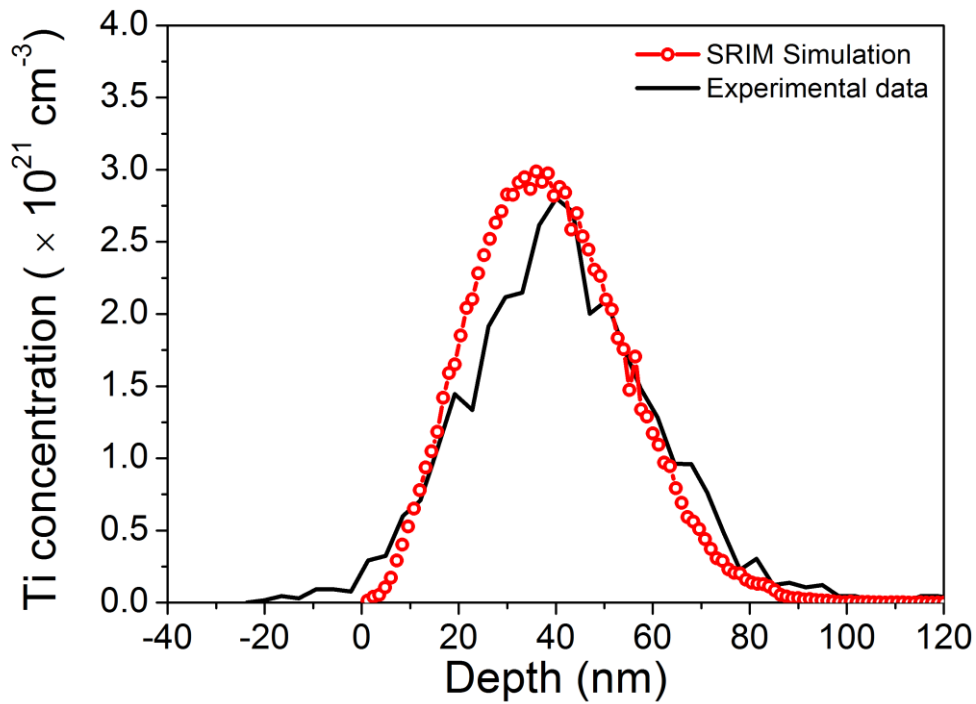


Figure 2.3 Ti depth profile in Ti implanted Si sample with a fluences of $1.2 \times 10^{16} \text{ cm}^{-2}$ at an implanted energy of 35 keV. We used the SRIM program to simulate the result [43]. Experimental result is the depth profile of Ti in Si, which is calculated by using Rutherford Universal Manipulation Program (RUMP) [44].

Stopping and Range of Ions in Matter (SRIM) can be used to calculate the depth profile of implanted ions. Figure 2.3 shows Ti depth profile in Ti implanted Si sample with fluence of $1.2 \times 10^{16} \text{ cm}^{-2}$ at implanted energy of 35 keV. As we can see from figure 2.3, the depth profile of SRIM simulations is well in agreement with experimental results. However, the Ti concentration from simulation is slightly larger than that from experimental results, which is due to the evaporation of some Ti ions during ion implantation.

A series of collisions with the host atoms will occur when ions with high energy are implanted into a target, causing the target atoms to shift. The target atoms transfer energy to other atoms during the movement, resulting in a series of vacancies and interstitial atoms and other types of disorder distribution in the crystal lattice. This kind of defects caused by ion implantation is called lattice damage.

The implanted ions which are lighter than the target atoms may cause damages in a large volume and small density due to the smaller energy transferred to the target atoms. The implanted ions which have large masses may cause damages in a

small volume damage and large density. With the increase of the implantation fluence, the isolated damage regions overlap and finally form a disordered amorphous layer.

The implanted ions are located at disordered lattice sites and have no contribution to the transport of carriers. Lattice damage leads to the decrease of carrier mobility. In order to recover the crystal order and activate the dopants, it is necessary to remove the lattice damage caused by ion implantation.

The implanted samples need to be heat-treated for an appropriate time. Then the lattice damage can be partly or largely removed, and the dopants also can be activated. This process is called annealing.

Furnace annealing (FA) and rapid thermal annealing (RTA) are common annealing techniques. The time of FA can range from several minutes to several hours. RTA works in the time range of 1-100s. The partially damaged crystal structure can be restored by both annealing methods and the dopants also can be activated. However, both methods have some drawbacks: (1) cannot completely remove the defects; (2) have small activation rate of the dopants; (4) the dopant diffusion; (5) segregate from the host material to form clusters. Therefore, FA and RTA are not suitable for silicon doped with deep level impurities.

In our work, we use both pulsed laser annealing and flash lamp annealing. A more detailed description of both annealing methods is presented in the following part.

2.2 Pulsed laser annealing (PLA)

Pulsed laser annealing was used to repair the damaged semiconductor materials (especially Si) caused by the implanted ions. Traditional melting techniques cannot completely remove the defects, resulting in the degradation of material properties, contaminations, etc. Pulsed laser annealing uses a broad range of wavelengths from UV to IR. Also there are a lot of operation modes, for instance, ns single laser pulse or repeated laser pulses. In our case, we used a Coherent XeCl excimer laser with 308 nm wavelength and 28 ns pulse duration.

Pulsed laser annealing is an ultra-fast heating process without causing chemical reactions on the surface of the materials. When the laser beam irradiates the surface of the solid semiconductor, the material undergoes a phase change due to the

energy of high density photons. The general order of the phase change is solid-liquid-solid, resulting in the conversion of the amorphous state into a polycrystalline or single crystalline state.

The mechanism of PLA for a semiconductor is as follows. Electrons can be excited from the valence band to the conduction band through absorbing photons with energy higher than the band gap, generating electron-hole pairs during this process. The electrons in higher energy levels excited from lower energy levels in the conduction band will relax to a meta-stable level by transitions in small steps. There is no photon generation during this process, so this is called non-radiative transition. The excited electrons finally fall down through the bandgap to the ground state and recombine with holes. This transition can be radiative or non-radiative. Normally, indirect bandgap semiconductors have larger probabilities of non-radiative transitions than direct bandgap semiconductors.

2.3 Flash lamp annealing (FLA)

PLA on the nanosecond time scale has been shown to be a promising tool to repair damage caused by the ion implantation for semiconductor materials. The surface layer can be molten and recrystallized via liquid-phase epitaxy in the nanosecond range when PLA is applied. Some defects can be induced by liquid-phase epitaxy, such as dopant segregation, surface evaporation, and cellular breakdown. However, FLA in millisecond range can render the temperature of the sample just slightly below the melting temperature leading to solid-phase epitaxy.

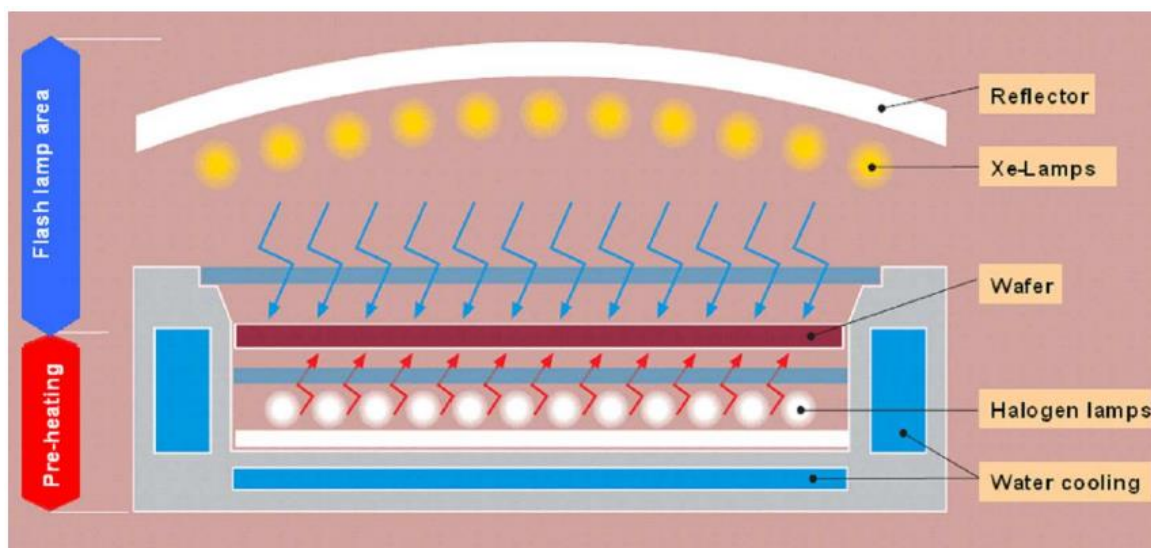


Figure 2.4 Schematic views of the FLA system. Adapted from ref. [45].

The FLA system consists of a reflector, a bank of Xe flash lamps, a wafer holder, two pieces of quartz plate and a preheating module is shown in figure 2.4. FLA includes 12 side-by-side connected Xe lamps, which can provide a large area of uniform flash. That makes FLA suitable for large-scale processing. Normally, the flash lamp and the actual processing chamber are separated because on the one hand the lamps cannot be affected by sublimated or evaporated materials, and on the other hand, samples can be protected even if the bulb explodes or breaks. In order to obtain a wafer with uniform temperature, a suitable shaped reflector is designed. A preheating system consisting of a continuous halogen array is installed under the sample processing chamber. When the temperature gradient between front and backside is reduced, the preheating system enables high peak temperatures. This reduction prevents the accumulation of harmful stress levels in the substrate due to different thermal expansion of the front and backside. The sample processing chamber consists of two sheets of quartz panels for near ultraviolet and visible light, which separates the air and the protective atmosphere filled inside. The water-cooled annealing chamber can introduce different gases and the annealing can be carried out under different ambient gases.

The high voltage charging capacitor provides pulsed energy for FLA. The flash pulse duration depends on the discharge R-C circuit. The voltage applied to the parallel connected flash lamps decays exponentially. The formula is as follows:

$$V(t) = V_0 \cdot e^{-t/RC}, \quad (2.4)$$

where V_0 is the capacitor voltage at $t = 0$, R is the resistance of the discharge circuit, C is the capacitance of the discharge circuit. The discharge time can be extended by enhancing the resistance and / or capacitance in the circuit. The pulse duration range is $100 \mu s < t < 100 \text{ ms}$. Two pulse durations of 3 ms and 20 ms are used in this thesis. The energy fluences of FLA for 3 ms and 20 ms flash are about 100 J/cm^2 and 250 J/cm^2 , respectively. The final temperature of the annealed surface layer could reach more than 2000°C depending on the intensity of the light flash and the optical properties of the annealed material. For most of the semiconductor materials, the temperature can reach to the melting point. However, the diffusivity of impurities is much larger in the liquid than in the solid phase. Thus, the redistribution and segregation of the dopants happen during liquid phase epitaxy for Si based materials. Therefore the actual annealing temperature on the sample surface can be controlled to stay below its melting point.

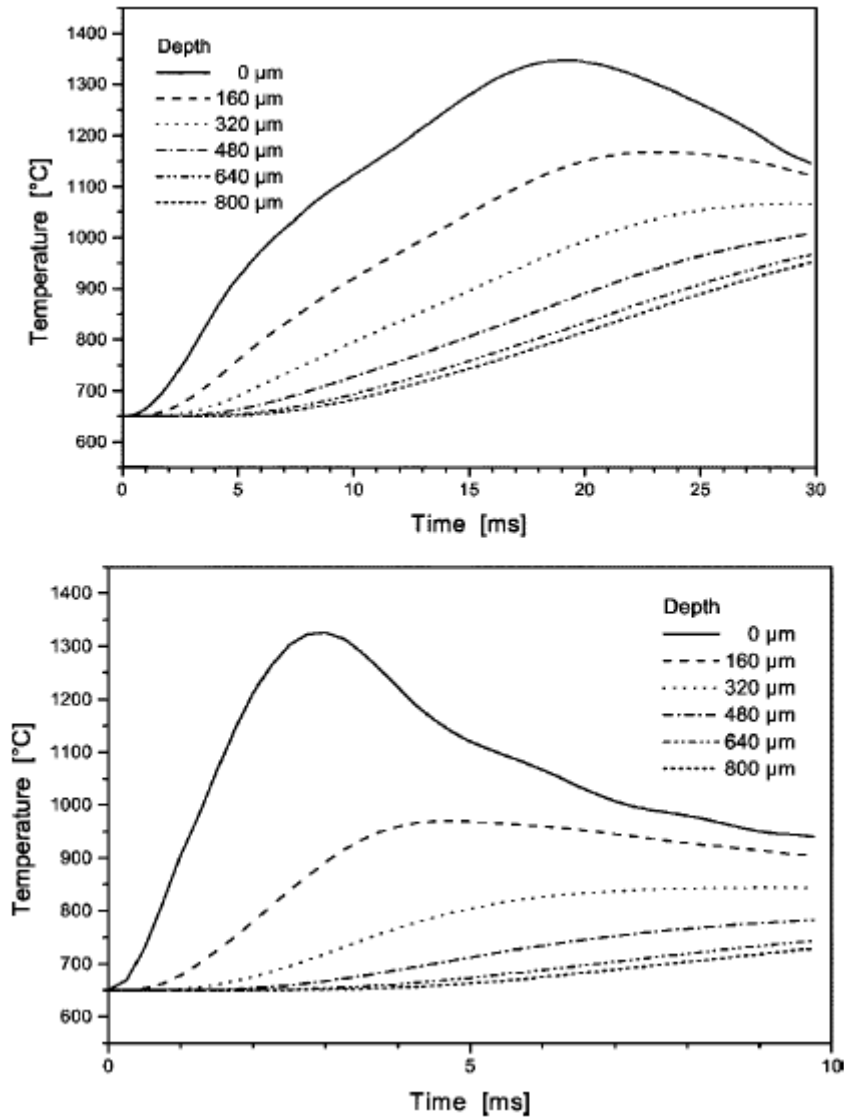


Figure 2.5 Temperature vs. time for different depths for a 800 μm thickness silicon wafer during FLA to 1300 $^{\circ}\text{C}$ at a preheating temperature of 650 $^{\circ}\text{C}$ for a time pulse duration of 20 ms (upper part) and 3 ms (lower part). From ref. [46].

The time-dependent temperature for a pure silicon wafer with 800 μm thickness for different depths during flash lamp annealing with time pulse duration of 3 ms and 20 ms is given in Figure 2.5. The depth of 800 μm at the backside of Si wafer can be heated up to 800 $^{\circ}\text{C}$ for the 20 ms pulse, which is 150 $^{\circ}\text{C}$ higher than the preheating temperature. The preheating temperature of backside remains up to 650 $^{\circ}\text{C}$ for the 3 ms pulse. Some thermal induced negative effects (oxidation, decomposition, and defect generation) can be avoided by FLA. Thus, FLA is considered as a low temperature processing technique.

The influence of PLA and FLA on the recrystallization of the implanted layer, the incorporation of impurities, and the redistribution of impurities in Si will be discussed in the following.

2.4 Rutherford backscattering and channeling spectrometry (RBS/C)

In order to check the recovery of crystal order after annealing, we performed Rutherford backscattering and channeling spectrometry (RBS/C) experiments. RBS is a simple and reliable ion beam analysis technique and can be mostly used to investigate the composition of films, the thickness of films, the implantation profiles, and the impurity diffusion profiles. RBS combined with channeling is used to determine the structural properties of the implanted layer, for example, the quality of epitaxial growth, the degree of implantation damage and the lattice location of impurities in host semiconductor. The detailed information will be described in the following sections.

2.4.1 Basic principles

A $^4\text{He}^+$ ion beam with energy in the MeV-range is shot on a target. Ion beams collide with the target atoms. Some ions are scattered by surface atoms, while the rest ions can penetrate into the target. Ions lose some energy through inelastic collisions with electrons and are backscattered in different paths. The energy of the backscattered ions is recorded by a sensitive electronic detector. We can obtain the following information through the energy spectrum of the backscattering ions. The first one is the mass of various elements contained in the target. The second one is the depth distribution which can be achieved by the amount of electronic energy loss.

2.4.2 Analysis of the elements in the target

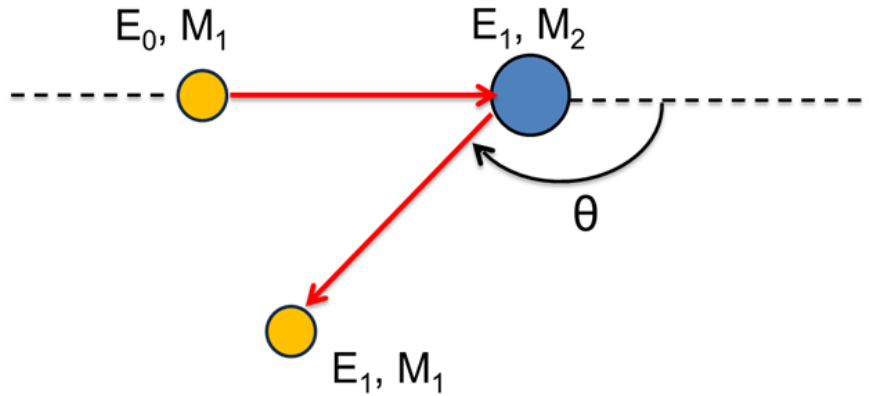


Figure 2.6 Basic principles of Rutherford backscattering analysis. Adapted from ref. [47].

We use RBS to determine the elements that exist in target by distinguishing the atomic masses of the elements. The elastic collision process between ion beam and the surface atoms is shown in Figure 2.6. Before the collision, the energy of the ion is E_0 . The energy of the backscattered ion is E_1 , which is smaller than the initial energy E_0 :

$$E_1 = k \cdot E_0, \quad (2.5)$$

where k , the kinematic factor, is the ratio of the energy of the backscattered ions (E_1) to the initial energy E_0 . k depends on scattering angle (θ), incident ion mass (M_1) and target mass (M_2).

$$k = \left[\frac{\cos \theta + \sqrt{\left(\frac{M_2}{M_1}\right)^2 - \sin^2 \theta}}{1 + \frac{M_2}{M_1}} \right]^2, \quad (2.6)$$

Generally, in order to increase the mass resolution, the angle of the detector is fixed at around 180° , since the energy loss is maximal during the scattering in this angle. Therefore, at $\theta = 180^\circ$ one obtains:

$$k = [(M_2 - M_1)/(M_2 + M_1)]^2, \quad (2.7)$$

When the mass of the element present in the target is heavy and the incident ion is light, k goes to one. Thus, the mass separation on the RBS spectrum decreases as the target mass increases. When M_1 and E_0 are constant, E_1 is only related to the target mass M_2 ($M_1 < M_2$). Thus, the elements contained in the target can be analyzed by the RBS energy spectrum.

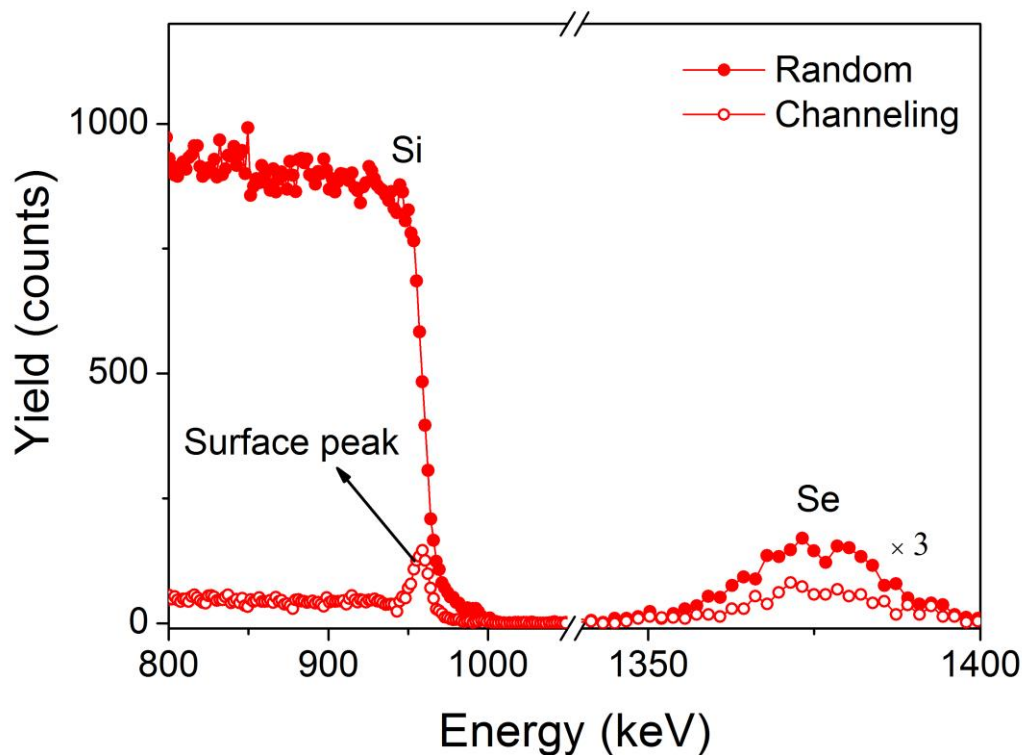


Figure 2.7 RBS spectra of Se implanted Si sample with fluence of $2.5 \times 10^{15} \text{ cm}^{-2}$ at random and channeling configuration after FLA annealing.

The RBS measurements can be used to analyze the heavy element impurities in the sample within a thickness of hundreds of nanometers by different backscattering energy.

Figure 2.7 illustrates the RBS spectra of Se implanted Si sample which is a typical application of this principle. The measurements were performed with a collimated 1.7 MeV $^4\text{He}^+$ beam at 170° backscattering angle. Due to the different masses of Si and Se, k is different. The backscattering energy of helium particles after colliding with Se is larger than that with Si. As shown in figure 2.7 the peak of Se is well separated on the Si substrate.

2.4.3 Channeling and RBS/C

When the ion beams is incident along a crystal axis of the target, the possibility of collision between incoming ions and the lattice atoms decreases in the channel or plane, resulting in a sharp reduction of backscattering yield. The ions have a higher

probability to enter a deeper position from the sample surface. This phenomenon is called channeling effect. The incident ions will stay in this open channel until they lose almost all of their energy or until they encounter an obstruction.

From the channeling spectra, we can determine the crystalline quality of the lattice after implantation and the lattice location of the impurities in the host lattice. The structural properties of the implanted layer can be investigated by RBS in channeling geometry (RBS/C). When the ion beam is incident along a crystal axis of a high-quality single crystal, the channeling ions will not be scattered and will continue going along the channel.

RBS spectra of Se implanted single crystalline Si are shown in figure 2.7. The random spectrum is defined when the ion beam is incident on the sample in random directions, while the channeling spectrum is defined when the ion beam is incident along the crystal axis or crystal plane of a single crystal. As expected, the yield of the channeling spectrum is much lower than that of the random spectrum. To evaluate the crystalline quality, the normalized minimum backscattering yield χ_{\min} , which is defined as the ratio of backscattering yield of channeling and random spectra, is calculated. χ_{\min} also shows the overall level of the lattice quality. If the sample is fully amorphous, the χ_{\min} is 100%, whereas a high-quality single crystal may have a χ_{\min} as low as 1–2%. The χ_{\min} value of Se implanted Si sample with fluence of $2.5 \times 10^{15} \text{ cm}^{-2}$ after FLA annealing is around 3%, which indicates a high degree of lattice recrystallization. The channeling spectrum shows a weak peak at around 960 keV, which is called the surface peak. When the $^4\text{He}^+$ beam bombards the sample, the collision of the incident ions with the first layer atoms near the sample surface leads to the interaction between the positive nuclei and the surface atoms. These ions will be backscattered, resulting in the formation of the surface peak.

Some defects will exist inside the host crystal due to the impurities induced after implantation, such as interstitial impurities, self-interstitials and dislocations. These defects will increase the backscattering yield. In contrast, the backscattering yield will decrease when the impurities are located at substitutional lattice sites in the host crystal. Therefore, we can obtain information about the crystalline quality of the target and the lattice location of impurities in the host materials.

2.4.4 Analysis of the impurity lattice location

It is important to determine the lattice location of impurities in crystalline semiconductors after doping. Generally, the impurities can be activated only when they are located in the substitutional lattice sites inside the host materials. We can use the channeling technique to directly determine the location of impurities in the crystal. When the ion beam is incident along a crystal axis of the substrate and the impurity atoms are not located at the lattice position (interstitial), the ion beam can be scattered on the impurity atoms and the backscattering yield increases. In contrast, if the impurity atoms are located at the lattice position (substitutional) of the crystal, the impurity atoms cannot be observed on the ion beam. Therefore, no scattering occurs on the impurity atoms.

According to the random channeling spectrum, we can calculate the substitutional fraction (f) of impurities in the crystal. f can be given by the following formula[48]:

$$f = [1 - \chi_{\min(I)}] / [1 - \chi_{\min(h)}], \quad (2.8)$$

Where $\chi_{\min(I)}$ is the minimal backscattering yield on impurity atoms, $\chi_{\min(h)}$ is the minimal backscattering yields on host atoms.

In order to determine the lattice location of impurities in the crystal, instead of one axial two or more axial results are required. For instance, if impurities cannot be observed either in the (100) or in the (111) crystal direction, therefore we say the impurities located at the substitutional position.

2.5 Hall measurements

In order to investigate the electronic properties of the implanted layer after annealing, we performed resistivity and Hall effect measurements. This measurement can be carried out in van der Pauw geometry using a commercial Lakeshore Hall System which can measure the resistivity of a flat sample. However, there are some condition limits when using this method, such as the width and length of the sample must be larger than the sample thickness; the sample should be uniform without any holes; and the contacts must be small enough compared with the size of the sample.

2.5.1 Sample preparation

For the van der Pauw method, we need to make electrical contact to four points on the sample surface. The preparation steps are as follows: First, in order to remove the oxide layer on the sample surface, it is necessary to immerse the sample in a 5% HF solution for 1 minute. Next, the sample of $5 \times 5 \text{ mm}^2$ was covered with aluminum foil and only four corners were exposed. Finally, the gold (Au) was deposited onto the four corners of the sample by magnetron sputtering.

2.5.2 Resistivity

The resistivity is determined by using the van der Pauw technique which is a common method for measuring resistivity of semiconductor samples [49].

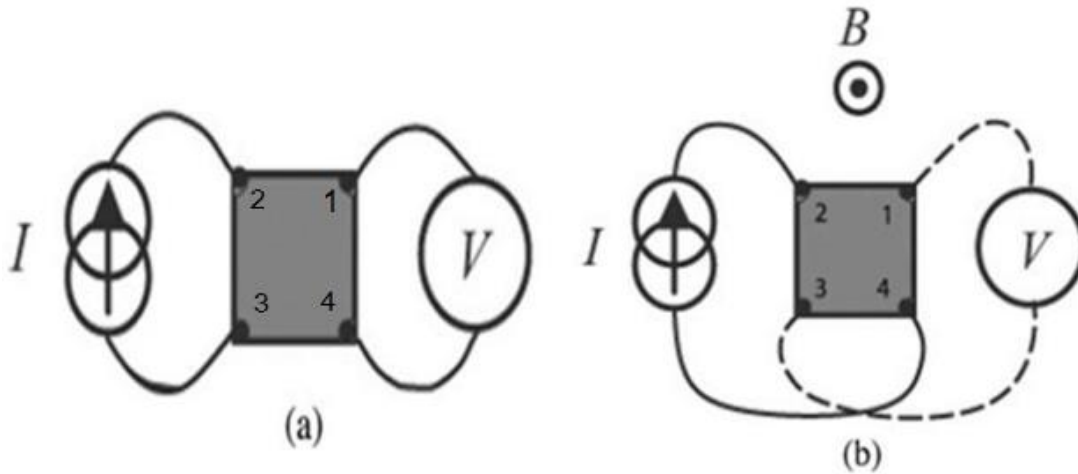


Figure 2.8 A schematic diagram of the Van der Pauw square connection for resistivity and Hall measurement without magnetic field (a) with magnetic field (b). Adapted from ref. [50].

Figure 2.8 shows a schematic diagram for a square Van der Pauw sample. For resistivity measurements (see figure 2.8 (a)), a current is applied from corner 3 to corner 2, while the voltage is measured from corner 4 to corner 1 (V_{41}). Due to symmetry, we repeat the reverse polarity measurement (apply I_{23} and measure V_{14}). Similarly, we repeat measurement for the remaining six voltages (V_{21} , V_{12} , V_{23} , V_{32} , V_{43} , and V_{34}). Eight resistances are calculated as follows:

$$R_{32, 41} = V_{41}/I_{32}, R_{23, 14} = V_{14}/I_{23}, \quad (2.9)$$

$$R_{34, 21} = V_{21}/I_{34}, R_{43, 12} = V_{12}/I_{43}, \quad (2.10)$$

$$R_{41, 23} = V_{23}/I_{41}, R_{14, 32} = V_{32}/I_{14}, \quad (2.11)$$

$$R_{12, 43} = V_{43}/I_{12}, R_{21, 34} = V_{34}/I_{21}, \quad (2.12)$$

We calculate two characteristic resistances R_A and R_B by these four measured resistances.

$$R_A = (R_{32, 41} + R_{23, 14} + R_{41, 23} + R_{14, 32})/4, \quad (2.13)$$

$$R_B = (R_{34, 21} + R_{43, 12} + R_{12, 43} + R_{21, 34})/4, \quad (2.14)$$

R_A and R_B are related to the sheet resistance R_S by the Van der Pauw equation:

$$e^{-\pi R_A/R_S} + e^{-\pi R_B/R_S} = 1 \quad (2.15)$$

from which R_S can be calculated numerically.

The bulk electrical resistivity ρ can be obtained through the following equation;

$$\rho = R_S d, \quad (2.16)$$

where d is the thickness of the sample.

2.5.3 Hall measurements

The moving electrons (or holes) are subjected to a force which is perpendicular to both the direction of flow and the direction of the applied field. The force of the motion charge in the magnetic field is called the Lorentz force. The direction of the deflection depends on the charge state. For a current flowing through a semiconductor with a strong magnetic field, the charge accumulates on one side of the semiconductor caused by the Lorentz force. A voltage is generated across the sample in the direction of carrier deflection, which is called Hall voltage. The Hall voltage can be determined by experimental measurement as shown in Figure 2.8 (b). The sign of the carrier and the sheet carrier density (p_s for holes and n_s for electrons) also can be determined. The bulk carrier density is then simply expressed as the ratio of the sheet carrier density (n_s or p_s) and the sample thickness (d). The Hall mobility (μ) can be calculated combined with resistivity measurements as follows:

$$\mu = \frac{1}{qn_s R_S}, \quad (2.17)$$

The unit of the Hall mobility is $\text{cm}^2\text{V}^{-1}\text{s}^{-1}$.

Chapter 3 Suppressing the cellular breakdown in silicon supersaturated with titanium

This chapter has been published:

F. Liu, S. Prucnal, R. Hübner, Y. Yuan, W. Skorupa, M. Helm, and S. Zhou, ***Suppressing the cellular breakdown in silicon supersaturated with titanium***, J. Phys. D: Appl. Phys. 49, 245104 (2016).

Hyper doping Si with up to 6 at.% Ti in solid solution was performed by ion implantation followed by pulsed laser annealing and flash lamp annealing. In both cases, the implanted Si layer can be well recrystallized by liquid phase epitaxy and solid phase epitaxy, respectively. Cross-sectional transmission electron microscopy of Ti-implanted Si after liquid phase epitaxy shows the so-called growth interface breakdown or cellular breakdown owing to the occurrence of constitutional supercooling in the melt. The appearance of cellular breakdown prevents further recrystallization. However, the out-diffusion and cellular breakdown can be effectively suppressed by solid phase epitaxy during flash lamp annealing due to the high velocity of amorphous-crystalline interface and the low diffusion velocity for Ti in the solid phase.

3.1 Introduction

Impurities play an important role in determining the electrical and optical properties of semiconductors. Recently it was demonstrated that deep level impurities can create an impurity band inside the gap of semiconductors if the doping concentration is high enough, e.g. for titanium (Ti) or chalcogens in Si [20, 51, 52]. The insertion of an impurity band can enhance the near infrared light absorption and leads to applications in the so-called intermediate band solar cell [20, 22, 23] or as infrared photodetectors [20, 26]. To form such an impurity band instead of isolated levels, one needs to have doping concentrations far exceeding the Mott transition limit, which is $\sim 5 \times 10^{19} \text{ cm}^{-3}$ for Ti [9]. Unfortunately, most deep level impurities (Ti, S and Se) have relatively low solubility in silicon [8, 6, 14]. As an industry-standard

method, ion implantation works in non-thermal-equilibrium regime and can overcome the thermal solubility limit. However, high-fluence ion implantation damages the crystalline order. Pulsed laser annealing (PLA) has been widely used to anneal Ti and chalcogen-ion-implanted Si [24, 27, 38, and 39]. Using PLA, the surface layer can be molten in the nanosecond range and recrystallized via liquid-phase epitaxy [53, 54]. In order to attain supersaturation, the solidification rate must be larger than the diffusive speed of the impurities [21, 55, and 56]. However, the challenge of PLA is to avoid dopant segregation and cellular breakdown at high doping concentration, preventing supersaturation. Regarding Ti-implanted Si, Pastor et al. reported that Ti ions massively occupy interstitial sites in the host semiconductor in highly Ti-implanted Si layers followed by PLA [28]. Recently, Mathews et al. pointed out that the intrinsic limit of the Ti concentration in Si is around $1...2 \times 10^{21} \text{ cm}^{-3}$ (2-4 at.%) [57]. This is attributed to the fact that during pulsed laser annealing and rapid solidification the impurities diffuse to the surface of the implanted layer and form a cellular breakdown microstructure, preventing further recrystallization [57].

In our work, single crystalline Si wafers have been implanted with Ti concentration above the concentration limit ($1...2 \times 10^{21} \text{ cm}^{-3}$) mentioned in ref. 56. The implanted layers were annealed by PLA and flash lamp annealing (FLA). Different from PLA, FLA in millisecond range can render the sample just slightly below the melting temperature leading to solid-phase epitaxy [58]. Our results indicate that Ti-implanted Si with a concentration above the equilibrium solid solubility limit can be recrystallized by both PLA and FLA. In terms of preventing surface segregation, FLA is superior to PLA because the cellular breakdown can be avoided leading to a much higher incorporation concentration.

3.2 Experimental

Intrinsic (001) Si wafers with a thickness of 525 μm ($R > 10^4 \Omega\cdot\text{cm}$ measured at room temperature) were implanted with a Ti^+ fluence of $1.2 \times 10^{16} \text{ cm}^{-2}$ at 35 keV. After implantation, the wafers were cut into pieces of $5 \times 5 \text{ mm}^2$ for PLA and FLA. The FLA was performed with a 3 ms light pulse in Ar ambient and the optical energy fluence was varied from 20 to 100 J/cm^2 . The estimated peak temperatures at the sample surface were below 1300 $^\circ\text{C}$. For comparison, some samples were annealed using a Coherent XeCl excimer laser ($\lambda=308 \text{ nm}$) at 0.6-1.0 J/cm^2 with a single pulse

of 28 ns in air atmosphere. The structural properties were investigated by channeling Rutherford backscattering spectrometry (cRBS) and Raman spectroscopy. For RBS measurements, 1.7 MeV He^+ ions were used at a backscattering angle of 170° . The RBS spectra were measured along random and channeling geometry. The Raman scattering spectra were recorded in the backscattering geometry using a 532 nm Nd:YAG laser with a charge coupled device camera cooled with liquid nitrogen. To locally analyze the microstructure of the Ti-implanted and subsequently annealed Si films, cross-sectional transmission electron microscopy (TEM) images were taken using an image-corrected FEI Titan 80-300 microscope operated at 300 kV. Element mapping based on energy-dispersive X-ray spectroscopy (EDXS) was performed using a FEI Talos F200X microscope operated at 200 kV and equipped with a Super-X EDXS detector system. In this manuscript, we only show the results annealed under the optimized conditions, i.e. obtaining the best recrystallization of Si, which are 0.8 J/cm^2 for PLA and 55.5 J/cm^2 for FLA, respectively.

3.3 Results

In figure 3.1, we show the Raman spectra of Ti-implanted Si samples with a fluence of $1.2 \times 10^{16} \text{ cm}^{-2}$ before and after PLA or FLA. The Raman spectrum of the single crystalline Si substrate is depicted for reference. The spectrum of the as-implanted sample exhibits a weak band at around 460 cm^{-1} , which is a typical feature of the amorphous silicon formed by the ion implantation process [59]. In addition, the as-implanted sample also shows a weak peak at around 520 cm^{-1} corresponding to the transverse optical phonon (TO) mode of single crystalline Si substrate beneath the implanted amorphous layer. After PLA or FLA, the weak band at 460 cm^{-1} which is related to the amorphous Si layer vanishes. The TO mode at 520 cm^{-1} appears as a sharp peak with similar intensity and linewidth of that from virgin single crystalline Si. The peak at 303 cm^{-1} corresponds to the two transverse acoustic (2TA) phonon mode of Si, which indicates that the crystalline order can be well recovered.

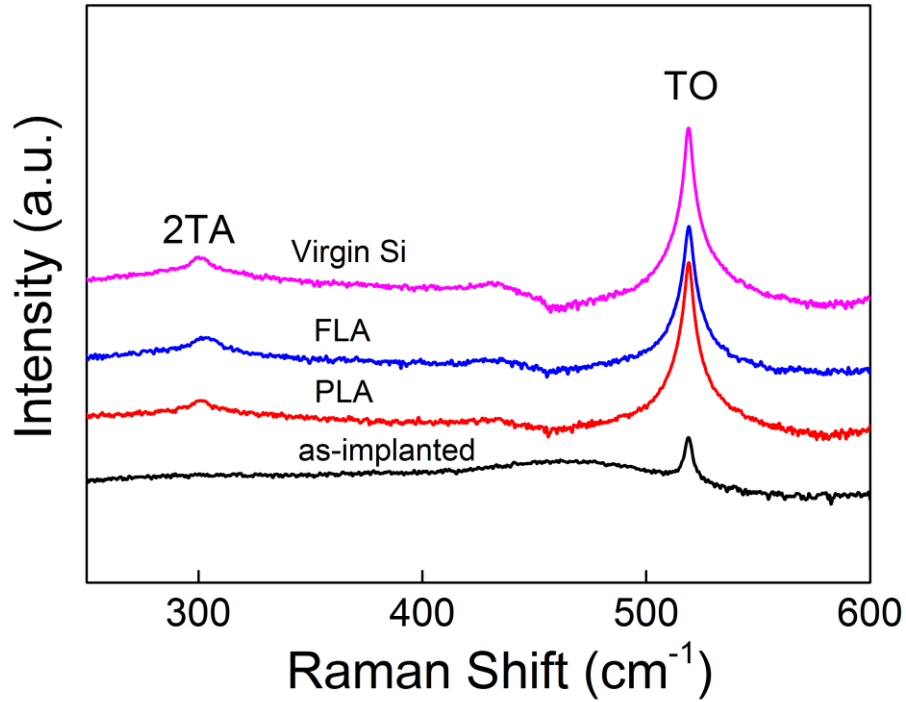


Figure 3.1 Raman scattering spectra of Ti-implanted Si samples with a fluence of $1.2 \times 10^{16} \text{ cm}^{-2}$ and subsequently annealed by PLA and FLA. For comparison, the results of as-implanted and virgin Si are also shown.

To study in more detail the crystallization process, RBS/Channeling measurements were performed on the samples before and after annealing. Figure 3.2 shows the RBS spectra of the implanted samples in both random and channeling configurations. As we can see, the as-implanted sample displays a broad damage peak at around 940 keV, pointing out that a highly disordered or amorphous Si layer has been formed during ion implantation. However, after annealing (by both PLA and FLA), the channeling spectra of the annealed samples with a very low backscattering yield are similar to that of virgin Si, indicating that the crystal order can be quite well reconstructed with considerable lattice quality. This is in a good agreement with the results obtained by Raman spectroscopy.

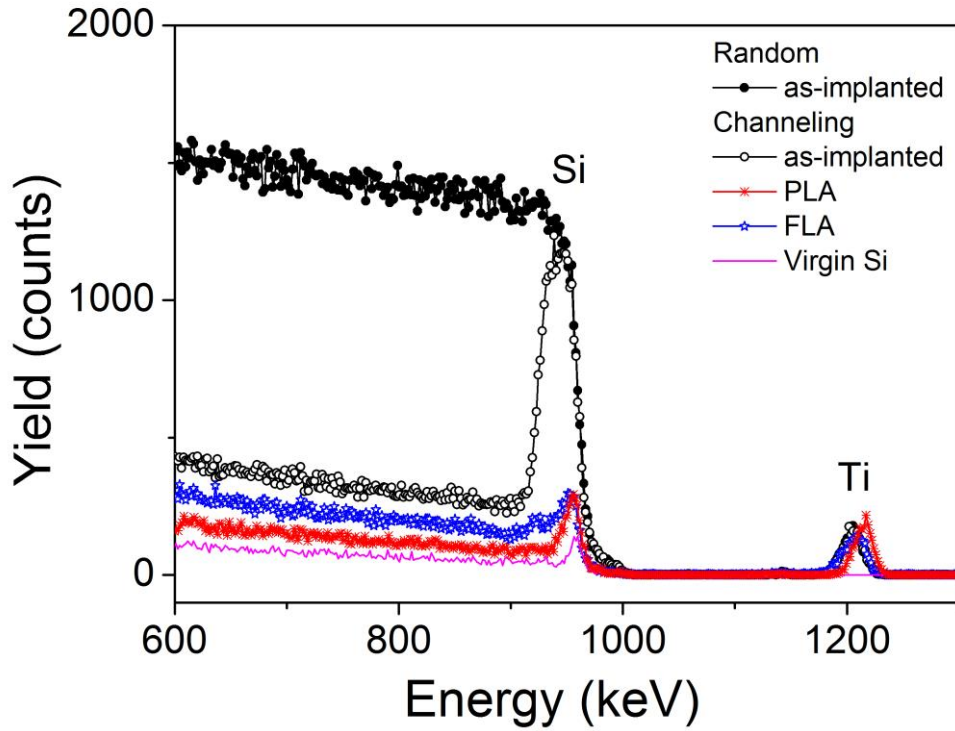


Figure 3.2 RBS spectra of Ti-implanted Si samples with a fluence of $1.2 \times 10^{16} \text{ cm}^{-2}$ at random and channeling configuration after annealing (0.8 J/cm^2 for PLA and 55.5 J/cm^2 for FLA). The spectra of as-implanted and virgin Si are also included for comparison.

In addition to prove the crystalline nature of implanted Si by FLA or PLA, RBS can be used to determine the depth distribution of Ti. We show in figure 3.3 (a) the magnified RBS spectra corresponding to the as-implanted sample and the annealed samples. Compare with the as-implanted sample, the Ti-related peak of the sample annealed by PLA shifts to higher energy, which indicates that Ti atoms diffuse towards the surface. In contrast, there is no significant difference before and after FLA. Figure 3.3 (b) shows the depth profile of Ti calculated from the RBS data by using the program RUMP. The Ti concentration in the FLA sample is well above the Mott limit and also above the concentration limit obtained by liquid phase epitaxy (the range between the two dashed lines in the figure) in Ref. 57. From the results shown in figure 3.3 (a) and (b), it is concluded that Ti impurities diffuse to the surface of the implanted layer during the PLA while there is no such diffusion during FLA treatment. The limit of impurity incorporated into the single crystalline Si matrix can be enhanced by FLA.

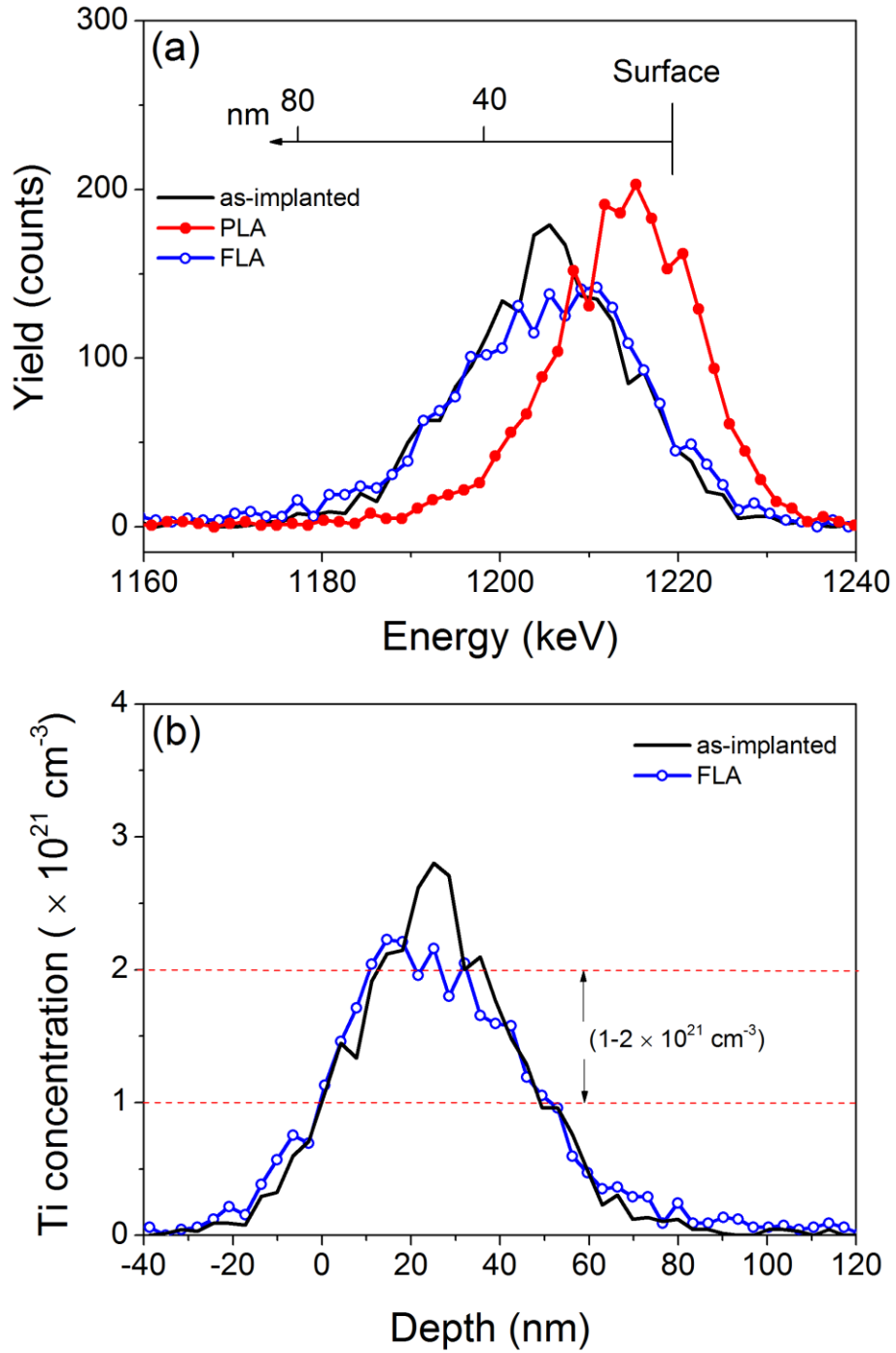


Figure 3.3 (a) RBS spectra of Ti-implanted Si samples with a fluence of $1.2 \times 10^{16} \text{ cm}^{-2}$ before and after annealing. A depth scale is indicated in the figure. (b) The depth profile of Ti in Si implanted with a fluence of $1.2 \times 10^{16} \text{ cm}^{-2}$ before and after FLA, which is calculated by using RUMP [44]. The Mott transition limit is around $5 \times 10^{19} \text{ cm}^{-3}$ for Ti in Si (Ref. 9). The range between the two dashed lines in the figure is the Ti concentration limit obtained by liquid phase epitaxy [57].

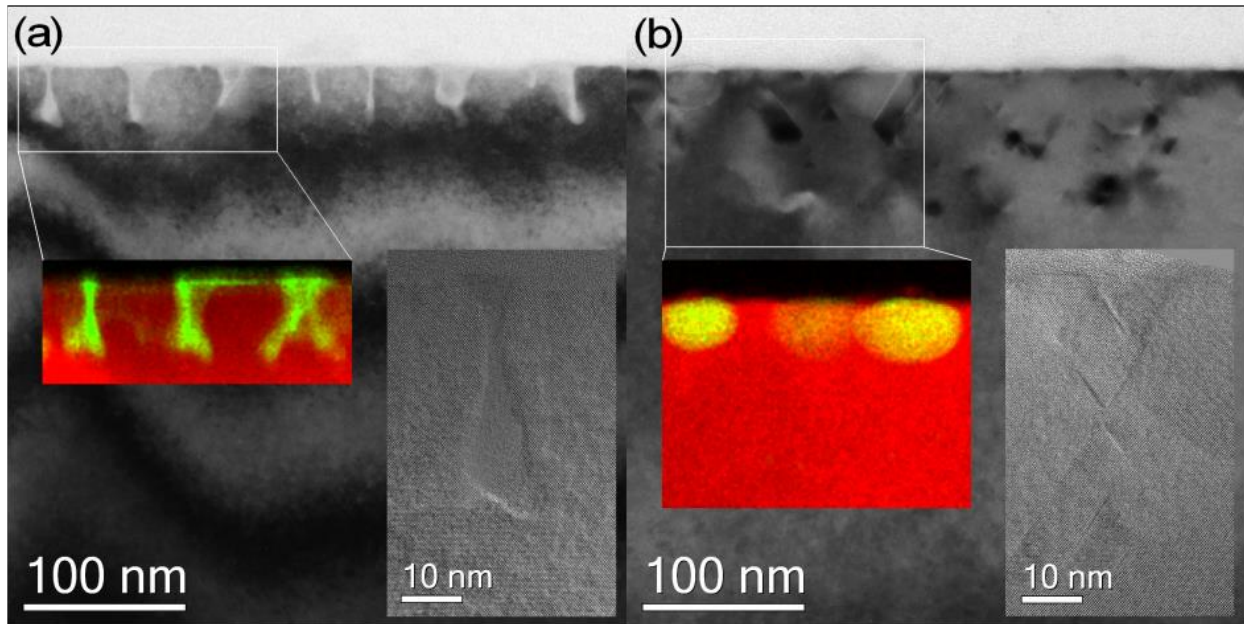


Figure 3.4 Cross-sectional bright-field TEM and high-resolution TEM micrographs (right insets) together with EDXS mappings (Ti: green, Si: red) of the indicated rectangular regions of Ti-implanted Si samples with a fluence of $1.2 \times 10^{16} \text{ cm}^{-2}$ (a) after PLA: 0.8 J/cm^2 and (b) after FLA: 55.5 J/cm^2 .

Figure 3.4 (a) shows a cross-sectional bright-field TEM micrograph of Ti-implanted Si after PLA. According to comparable diffraction contrast extending from the Si substrate to the sample surface, single crystalline regrowth of the Ti-implanted layer occurs during pulsed laser annealing. There are, however, amorphous “walls” with a lateral separation of about 50 nm extending from the sample surface almost perpendicularly to a depth of up to 50 nm. HRTEM imaging (right inset of figure 3.4 (a)) confirms the amorphous microstructure of these walls and the defect-free single-crystalline regrowth alongside. According to EDXS mapping (left inset of figure 3.4 (a)), titanium is mainly observed within the walls and partially at the sample surface. The measured Ti signal in the neighboring areas can be explained by a projection effect of the 2d mapping probing not only the regrown Si areas but also a Ti-containing wall lying at least partially in the plane of the TEM lamella. The TEM results indicate that a cell structure has formed during the rapid solidification process after PLA. It is the so-called growth interface breakdown or cellular breakdown due to the occurrence of constitutional supercooling in the melt [60-63]. At high enough impurity concentrations, a morphological instability occurs at the liquid-solid interface, resulting in the lateral segregation of Ti impurities and leading to a cellular

solidification microstructure [60-63]. At low impurity concentration, the planar interface can still be kept but with surface segregation [28]. As shown in figure 3.4 (a), the average lateral cell dimension in Ti-implanted Si after PLA is around 50 nm. The interior of each cell is defect-free silicon with Ti segregating at the cell walls. The cell size is proportional to the ratio between the impurity diffusion coefficient in the liquid silicon and the velocity of solidification [64]. The appearance of cellular breakdown prevents impurity incorporation into the single crystalline Si matrix.

In comparison, figure 3.4 (b) shows a bright-field TEM image of Ti-implanted Si after FLA. Again, single crystalline regrowth occurs during annealing. However, defects, such as stacking faults (right inset of figure 3.4 (b)), are incorporated into Si. The formation of such stacking faults is due to the high solidification speed during the rapid recrystallization of Si [65, 66]. Additionally, hemispherical particles beneath the sample surface are seen in figure 3.4 (b). They are of single crystalline nature, partially misaligned compared to the Si substrate and composed of Ti and Si, as shown by EDXS mapping in the left inset of figure 3.4 (b). Compared to PLA treatment, there is no cellular breakdown during flash lamp annealing for Si implanted with the same Ti concentration.

The impurity incorporation of Ti implanted Si was interpreted by Continuous Growth Model (CGM) for solute trapping [55],

$$k = \frac{k_e + \frac{v}{v_D}}{1 + \frac{v}{v_D}} \quad (3.1)$$

where k is the partition coefficient, which is the ratio of the dopant concentration in the solid and in the liquid at the interface, k_e is the equilibrium partition coefficient, v is the solidification velocity, and v_D is the diffusive velocity.

We try to interpret how to incorporate the impurities into Si during rapid solidification. The supersaturation is due to solute trapping at the moving amorphous/crystalline interface when the solidification velocity is larger than the diffusive velocity [15, 67]. The out-diffusion of impurities happens when the diffusive velocity is larger than the solidification velocity during recrystallization. The value of k is an important indicator to determine how many impurity atoms are incorporated into the semiconductor. If $k \ll 1$, the impurity atoms have more probability of redistribution and have less probability of incorporation. The redistribution means that the dopant diffuses deep into the host semiconductor or towards the surface. If $k \approx 1$ (v is comparable to or larger than v_D), the impurity atoms have less chance of

redistribution and have more probability of incorporation [67]. During liquid phase epitaxy the diffusive velocity of transition metals is typically 10^2 – 10^4 m/s [60], and the crystallization velocity is 1–10 m/s [68]. The value of k is below 10^{-2} for transition metals in Si [69], which is far below 1. So Ti has more chance of redistribution in Si after PLA. This can be the explanation of Ti diffusion towards the surface after annealing, which is shown in figure 3.3 (a). Solute concentration profile shows a spike due to the larger v_D in the liquid at the solidification front [57], which is caused by dramatically solute partitioning at the liquid-solid interface. This spike increases the chance of cellular breakdown, the morphologically instability happens at the liquid-solid interface, resulting in the lateral segregation of Ti impurities and leading to a cellular breakdown microstructure in figure 3.4 (a). However, the cellular breakdown cannot be observed in sample after FLA. FLA is a solid-phase process and it has a millisecond range processing time. The metastable solubility is the competition between the diffusive velocity of the impurity in the amorphous phase and the velocity of solid phase epitaxy, both of which depend on the temperature [69, 70]. The impurities can be trapped into Si in this process, due to the high velocity (10^{-1} – 10^{-3} m/s) of the amorphous-crystalline interface and the low diffusion velocity (10^{-2} – 10^{-4} m/s) for FLA (for temperatures below 1300 °C) [14, 71]. Thus, we can obtain the metastable solubility which is around one to two orders of magnitude larger than the maximum equilibrium solubility [67]. This is also why Ti redistribution can be suppressed in the FLA sample, as shown in figure 3.3 (a) and figure 3.4 (b). Burton *et al.* discussed the distribution of impurity in the crystal grown from melt [72]. In their model the impurity distribution also strongly depends on the comparison between the solidification front velocity and the impurity diffusion velocity.

3.4 Conclusions

In conclusion, we have used FLA in the millisecond time scale to incorporate titanium into the Si matrix well above the solid solubility limit. Our results indicate that a very high degree of lattice recrystallization has been attained after FLA. In terms of preventing surface segregation and cellular breakdown, FLA is superior to the nanosecond laser annealing. This approach of combining ion implantation and FLA is not limited to the case of Ti in Si only and should be generally valid for other deep

level impurities, such as Au and Zn, after carefully optimizing the annealing parameters.

Chapter 4 On the insulator-to-metal transition in titanium-implanted silicon

This chapter has been published:

F. Liu, M. Wang, Y. Berencén, S. Prucnal, M. Engler, R. Hübner, Y. Yuan, R. Heller, R. Böttger, L. Rebohle, W. Skorupa, M. Helm, and S. Zhou, ***On the insulator-to-metal transition in titanium-implanted silicon***, Scientific Reports 8, 4164 (2018).

Hyperdoped silicon with deep level impurities has attracted much research interest due to its promising optical and electrical properties. In this work, single crystalline silicon supersaturated with titanium was fabricated by ion implantation followed by both pulsed laser melting and flash lamp annealing. The decrease of sheet resistance with increasing Ti concentration is attributed to a surface morphology effect due to the formation of cellular breakdown at the surface and the percolation conduction at high Ti concentration is responsible for the metallic-like conductivity. The insulator-to-metal transition does not happen. However, the doping effect of Ti incorporation at low concentration cannot be excluded, which might be responsible for the observed optical properties reported in literature.

4.1 Introduction

Hyperdoping Si with deep level impurities is one of the most effective approaches to form an intermediate band (IB). IB materials are candidates for infrared photodetectors and highly efficient solar cells [31, 32-35, 29, 37, 73]. The strong optical absorbance by transitions in the near-infrared range from 1100 to 2500 nm was observed in S-, Se-, and Te-hyperdoped silicon [32, 74, 75]. Insulator-to-metal transition (IMT) has been observed in S- and Se-hyperdoped silicon [29, 38, 39], which is a direct evidence for the formation of an IB. Titanium is another deep-level impurity candidate for forming an IB in Si [25, 76, 77]. Theoretical calculations predict that an IB can be formed in Si when Ti ions are at either interstitial or substitutional sites [28]. Indeed, Pastor *et al.* have shown that Ti impurities are located at interstitial lattice sites in Ti-hyperdoped Si fabricated by ion implantation

and pulsed laser annealing (PLA) [29]. On the other hand, Markevich *et al.* found evidence for the existence of substitutional Ti atoms in the Si lattice for samples implanted with Ti at very low fluences [78]. Nevertheless, Olea *et al.* observed a strong sub-bandgap absorption in Ti-implanted Si samples, suggesting the potential for optoelectronic applications [24, 79]. Regarding the electrical properties of Ti-hyperdoped Si, it is believed that Ti behaves as a deep donor [28]. Several reports claim that with increasing Ti concentration a Mott-type insulator-to-metal transition occurs which is accompanied by the formation of an IB [25, 29, 52, 77]. However, it is worth mentioning that the interface instability in form of a cellular breakdown [60,62] occurs when the Ti doping concentration reaches $1\text{--}2 \times 10^{21} \text{ cm}^{-3}$ (2–4 at. %) during rapid solidification [31]. In a recent paper, we have also reported that the cellular breakdown takes place in Ti-implanted Si samples after pulsed laser annealing (PLA), but it can be effectively suppressed by millisecond flash lamp annealing (FLA) [80]. The appearance of cellular breakdown prevents Ti incorporation into the single-crystalline Si matrix. Moreover, the inhomogeneous distribution of Ti impurities also complicates the interpretation of the electrical properties. Therefore, it still remains unclear whether the IMT in Ti-hyperdoped Si happens or not.

In the present work, Ti-hyperdoped Si was fabricated by ion implantation followed by PLA and FLA, respectively. We have investigated the structural and electrical properties in the fabricated Ti-hyperdoped Si samples. After FLA, the samples remain insulating even with the highest Ti implantation fluence, whereas the sheet resistance decreases with increasing Ti concentration after PLA. According to the results from conductive atomic force microscopy (C-AFM), the decrease of the sheet resistance after PLA is attributed to the percolation of Ti-rich cellular walls and not the insulator-to-metal transition due to Ti-doping.

4.2 Experimental section

Single-side polished, semi-insulating (100) Si wafers (resistivity $> 10^5 \Omega \cdot \text{cm}$) with a thickness of 525 μm were implanted with Ti ions at an energy of 35 keV and fluences of $1.2 \times 10^{16} \text{ cm}^{-2}$, $6 \times 10^{15} \text{ cm}^{-2}$ and $2 \times 10^{15} \text{ cm}^{-2}$ at room temperature. In order to avoid channeling effects, samples were tilted by 7° with respect to the incident beam axis. The average thickness of the doped layer was about 60 nm [80]. After ion implantation, wafers were cut into pieces with a size of $5 \times 5 \text{ mm}^2$. Two

annealing methods, viz. millisecond-range FLA [58] for ms-range or PLA for ns-range were performed. The FLA was done in Ar ambient with an energy density in the range between 50 and 60 J/cm², corresponding to a surface temperature between 1100 and 1300 °C. A homogeneous flash was provided by the installed array of Xe-lamps connected in parallel with a reflector behind and a pre-heating module. The PLA was carried out in ambient using a XeCl excimer laser beam (Coherent COMPexPRO201, $\lambda = 308$ nm wavelengths, 28 ns pulse duration). A homogenized 5 × 5 mm² laser beam was produced with the help of a VarioLas optical system. During the PLA, a single laser pulse with an average energy density ranging from 0.2 to 0.8 J/cm² was applied to irradiate the as-implanted layers.

Raman spectroscopy was performed to investigate the crystalline quality of implanted and annealed samples. The Raman scattering spectra were obtained using a 532 nm Nd:YAG laser with a charge-coupled device camera cooled with liquid nitrogen. The crystallinity of the Si matrix after annealing and the location of the Ti impurities within the Si lattice were analyzed by channeling Rutherford backscattering spectrometry (cRBS). cRBS measurements were performed with a collimated 1.7 MeV He⁺ beam at a 170° backscattering angle. The optimized energy densities for FLA and PLA were determined according to the structural properties after annealing, i.e. the narrowest Raman peak and the lowest channeling yield in RBS.

Electrical properties of implanted samples were examined using a commercial Lakeshore Hall System in van-der-Pauw-geometry between 2 and 300 K. The usage of a semi-insulating Si wafer makes the electrical measurements and data interpretation easier, since the parallel conductance from the thick insulating substrates can be neglected [28]. Scanning electron microscopy (SEM) using secondary electrons and backscattered electrons was applied to characterize the surface morphology and to qualitatively analyze the lateral compositional distribution, respectively. C-AFM was performed using tips with approx. 100 nm thick conductive diamond-like carbon coating to correlate the electrical conduction with the surface morphology.

4.3 Results

4.3.1 Recrystallization of Ti-implanted Si

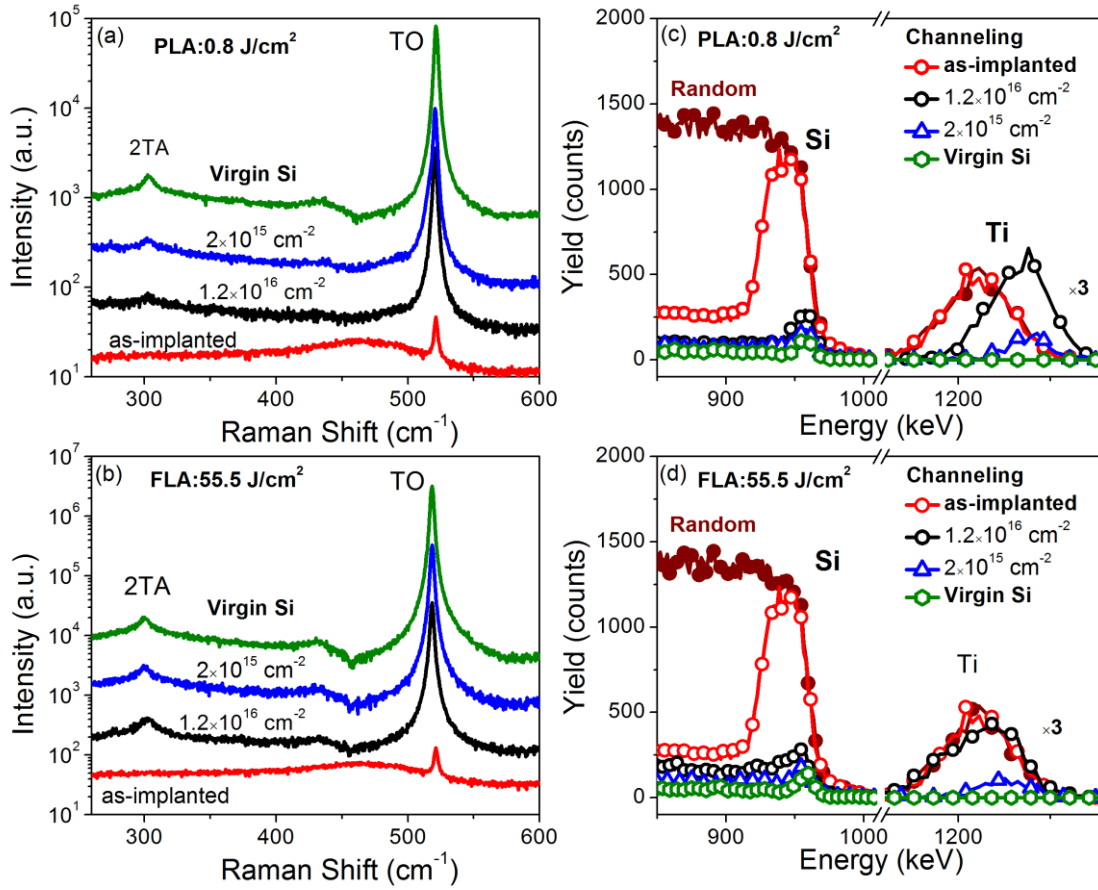


Figure 4.1 Raman scattering (a, b) and Rutherford backscattering spectrometry/channeling (cRBS) (c, d) spectra of Ti-implanted Si samples with fluences of $1.2 \times 10^{16} \text{ cm}^{-2}$ and $2 \times 10^{15} \text{ cm}^{-2}$ are shown in (a, c) after PLA at 0.8 J/cm^2 and (b, d) FLA at 55.5 J/cm^2 . Both Raman and RBS spectra for virgin Si as well as the as-implanted samples with the fluence of $1.2 \times 10^{16} \text{ cm}^{-2}$ are shown for comparison.

Figures 4.1 (a) and (b) show Raman spectra of Ti-implanted samples with fluences of $1.2 \times 10^{16} \text{ cm}^{-2}$ and $2 \times 10^{15} \text{ cm}^{-2}$ after PLA with an energy density of 0.8 J/cm^2 and after FLA at 55.5 J/cm^2 , respectively. For comparison, the Raman spectra obtained from the as-implanted sample and the virgin Si are added. The Raman spectrum of virgin Si shows a narrow peak at around 520 cm^{-1} which corresponds to the transverse optical (TO) phonon mode of single-crystalline Si. A weak band at around 460 cm^{-1} is observed in the as-implanted sample due to amorphous layer

formation upon ion implantation [59, 81]. The weak peak at around 520 cm^{-1} for the as-implanted sample is coming from the substrate which is not affected by the ion beam. After annealing, the band associated with the amorphous layer vanishes and the strong phonon mode at 520 cm^{-1} corresponding to crystalline Si dominates the Raman spectra. The results prove that the crystal order, even in heavily implanted Si, can be well restored by both FLA and PLA.

RBS spectra obtained in both random and channeling configurations are shown in Figures 4.1 (c) and (d), respectively. The channeling minimum yield (χ_{\min}) which measures the degree of lattice damage in the host semiconductor is defined as the ratio of the backscattering yield of the channeling and the random spectra. If the implanted layer is completely damaged after implantation, χ_{\min} is 100%. On the contrary, a high-quality single crystal is expected to have a χ_{\min} of 1–2%. The as-implanted sample shows a broad damage peak at around 940 keV and its χ_{\min} is calculated to be about 92%, showing that the implanted region becomes amorphous. After FLA or PLA, the backscattering yields in channeling condition are very close to that of the virgin Si, pointing out that the crystal order can be restored and thus a high-lattice quality is obtained. However, the channeling backscattering yield increases slightly with increasing ion fluence from $2 \times 10^{15}\text{ cm}^{-2}$ to $1.2 \times 10^{16}\text{ cm}^{-2}$ for both PLA and FLA samples. From the RBS results, the out-diffusion of Ti after PLA is clearly observed. As shown in figure. 4.1 (c), the Ti peak significantly shifts to higher energies. The detailed results have been reported in Ref. 80.

4.3.2 Lattice location of Ti impurities

To determine the location of the Ti atoms within the Si lattice, we show magnified RBS spectra corresponding to the Ti-related signal for the samples implanted with fluences of $2 \times 10^{15}\text{ cm}^{-2}$ Fig. 4.2 (a) and $1.2 \times 10^{16}\text{ cm}^{-2}$ Fig. 4.2 (b) being FLA-processed at 55 J/cm^2 . As can be seen from these figure, there are no differences between the random and channeling RBS configuration for the Ti signal, indicating that most of the Ti atoms are not located at substitutional sites. In order to further investigate the position of the Ti atoms within Si, we performed angular scans about the [001] axis of Si. The normalized scattering yield for Si and Ti atoms at the same depth is plotted in Fig. 4.2 (c). There are significant differences between the angular scans for Ti and for Si. When the sample is tilted about Si [001], the channeling

behavior for Si is clearly observed, but no change is detected for Ti. This indicates that Ti atoms are not located at the substitutional sites based on the detection sensitivity of our technique [82, 83]. According to cross-sectional TEM analysis, FLA leads to single-crystalline regrowth of the implanted region with the incorporation of defects, such as stacking faults. Additionally, hemispherical particles of single-crystalline nature, partially misaligned compared to the Si substrate and composed of Ti and Si are formed beneath the sample surface [80]. The RBS/channeling results can also be understood if the majority of the Ti atoms form polycrystalline secondary phases.

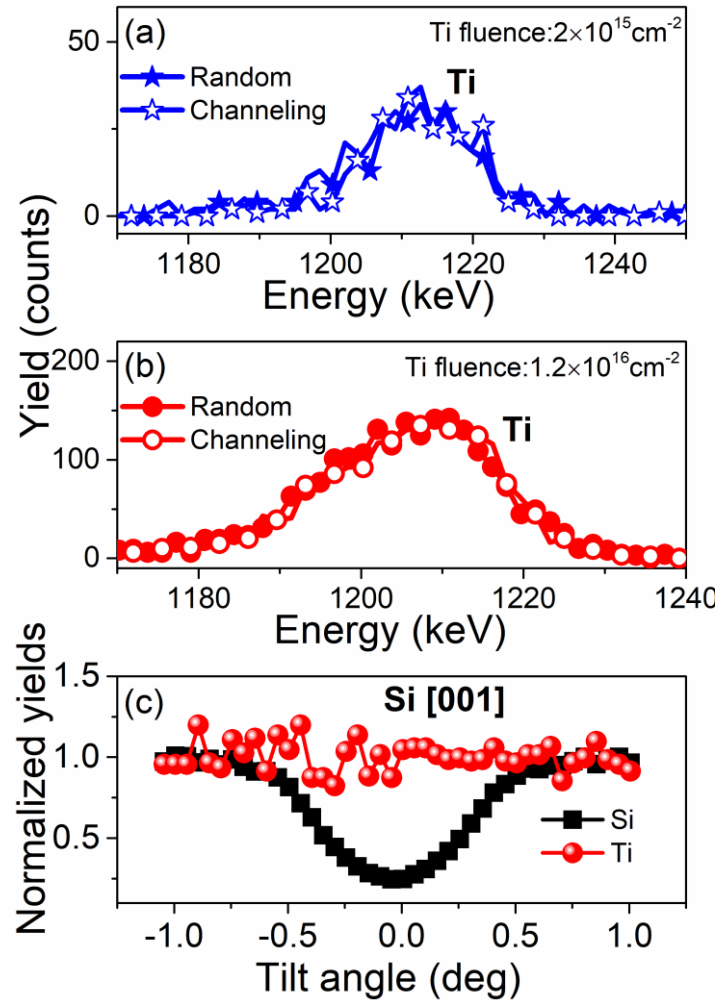


Figure 4.2 RBS spectra of Ti-implanted Si samples with fluences of $2 \times 10^{15} \text{ cm}^{-2}$ (a) and $1.2 \times 10^{16} \text{ cm}^{-2}$ (b) in random and channeling configuration for the Ti-related signal. Angular scans about the [001] direction for the Ti-implanted Si sample with a fluence of $1.2 \times 10^{16} \text{ cm}^{-2}$ (c). All samples shown here are flash lamp annealed.

4.3.3 Electrical conduction

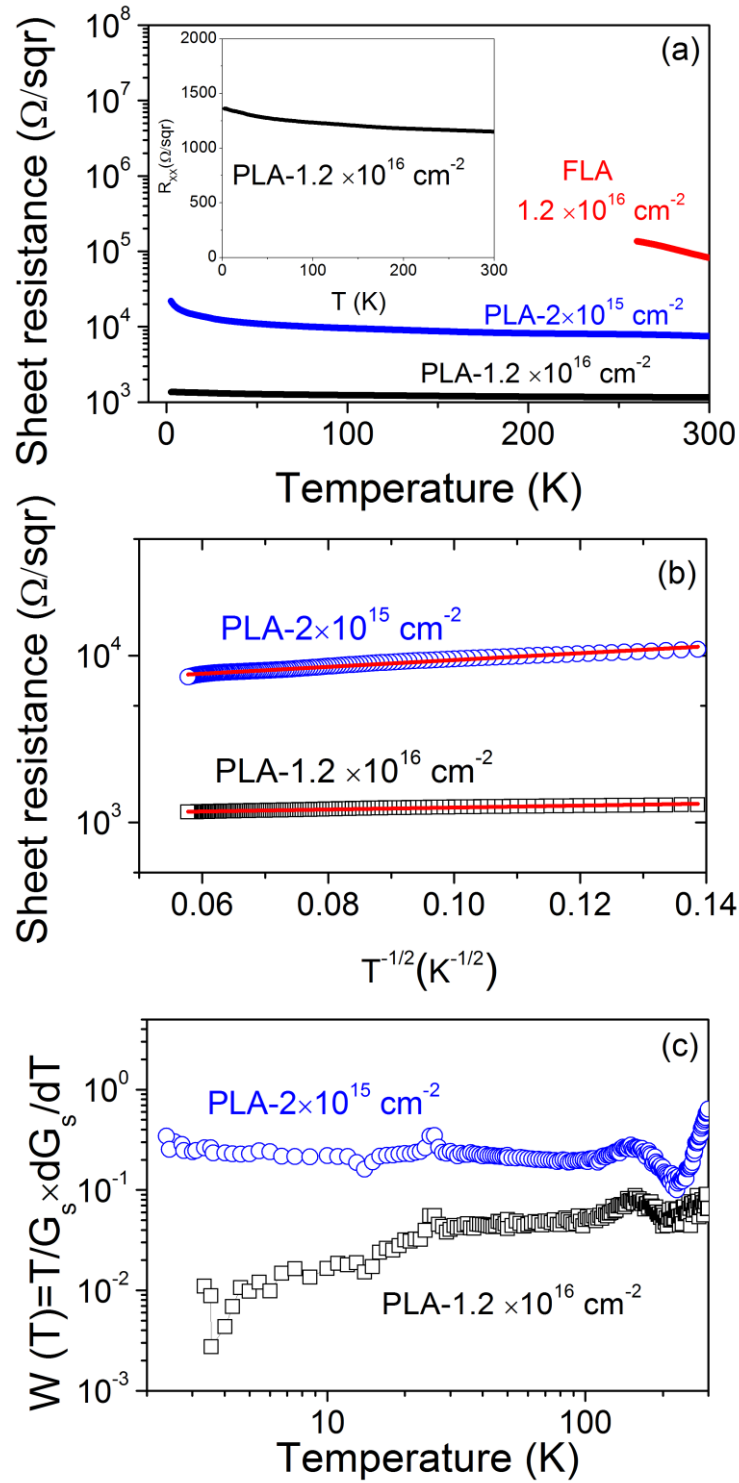


Figure 4.3 (a) Temperature-dependent sheet resistance of Ti-implanted Si after PLA and FLA. The inset shows the sheet resistance, in a linear scale, of the PLA-treated sample with a fluence of $1.2 \times 10^{16} \text{ cm}^{-2}$. (b) Analysis of transport properties for PLA samples showing the sheet resistance values as a function of $T^{-1/2}$. (c) Reduced activation energy W of the conductance versus temperature for the PLA samples.

Figure 4.3 (a) shows the temperature-dependent sheet resistance over the temperature range 2.5–300 K for samples after different annealing conditions. The inset in Fig. 4.3 (a) shows a linear scale representation of the sheet resistance as function of temperature for sample PLA- $1.2 \times 10^{16} \text{ cm}^{-2}$. For the PLA samples, the sheet resistance decreases with increasing Ti doping. In case of samples with lower Ti concentration, the sheet resistance significantly increases with decreasing temperature, showing semiconducting behavior. However, the sheet resistance in samples with high Ti concentration shows only very weak temperature dependence [see the inset to figure 4.3 (a)], similar to a metal with a low conductivity. The sheet resistance of the FLA-treated samples was found to be higher compared with the one measured in PLA-treated samples at the same implantation fluence of $1.2 \times 10^{16} \text{ cm}^{-2}$. This suggests that the electrical conductivity of those samples has a different origin. Note that the as-implanted and the virgin samples are highly resistive with a sheet resistance larger than $10^6 \Omega/\text{sqr}$ at room temperature.

As shown in Fig. 4.3 (b), the temperature dependence of PLA samples can be scaled as:

$$R = R_0 \exp\left(\frac{T_0}{T}\right)^{\frac{1}{2}} \quad (4.1)$$

where R_0 is a pre-exponential constant and T_0 is a characteristic temperature related with the material properties. The characteristic parameter T_0 extracted from the experimental data fitting was found to be 22.6 K ($\sim 1.96 \text{ meV}$) and 1.9 K ($\sim 0.16 \text{ meV}$) for sample PLA- $2 \times 10^{15} \text{ cm}^{-2}$ and sample PLA- $1.2 \times 10^{16} \text{ cm}^{-2}$, respectively. This logarithmic scale of sheet resistance values as a function of $T^{-1/2}$ is characteristic of granular metals when transport is governed by tunneling among isolated metal grains [84-86], which refers to Ti cellular breakdown in the present case. Moreover, the magnitude of T_0 is greatly reduced with increasing Ti implantation fluences seen in Fig. 4.3 (b). In comparison with results reported in ref. [86], sample PLA- $1.2 \times 10^{16} \text{ cm}^{-2}$ lies at the percolation threshold. In addition, Fig. 4.3 (c) shows the reduced activation energy of the conductance at various temperatures for the PLA samples, which is derived from the potential law [87] modelled as:

$$W = \frac{d \ln G_s}{d \ln T} = \left(\frac{T}{G_s}\right) \frac{d G_s}{dT} \quad (4.2)$$

where G_s is the sheet conductance deduced from sheet resistance. As shown in Fig. 4.3 (c), the reduced activation energy W is nearly zero for the sample PLA- $1.2 \times 10^{16} \text{ cm}^{-2}$. This means that it exhibits a relatively finite conductivity as temperature tends

to zero [88]. The decrease of W at low temperature for the sample $\text{PLA-}1.2 \times 10^{16} \text{ cm}^{-2}$ indicates that this sample lies in the metallic regime.

4.3.4 Surface morphology

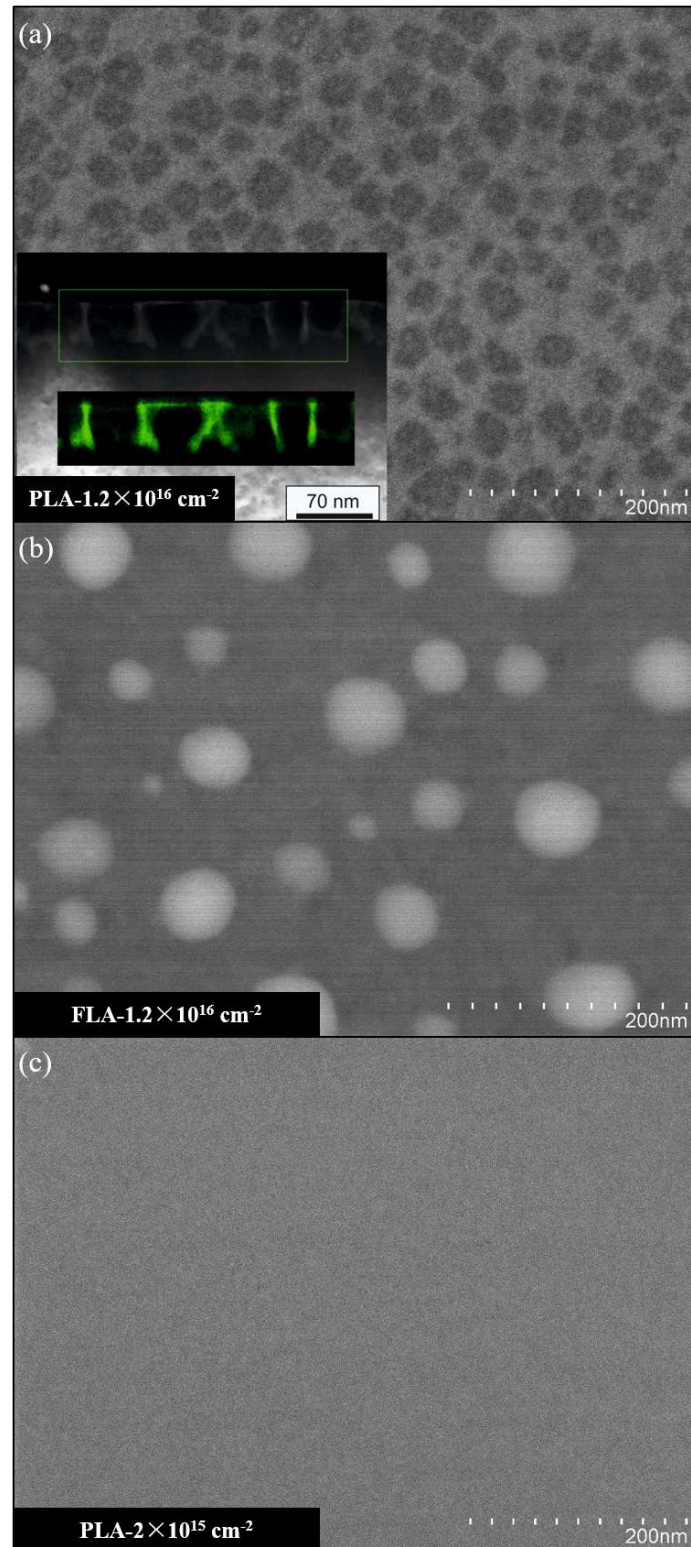


Figure 4.4 Top-view SEM image of the metallic sample PLA- $1.2 \times 10^{16} \text{ cm}^{-2}$ (a), the insulating sample FLA- $1.2 \times 10^{16} \text{ cm}^{-2}$ (b) and the insulating sample PLA- $2 \times 10^{15} \text{ cm}^{-2}$ (c). The light-grey dots (sample FLA- $1.2 \times 10^{16} \text{ cm}^{-2}$) and nets (sample PLA- $1.2 \times 10^{16} \text{ cm}^{-2}$) are Ti-rich phases as identified by energy-dispersive X-ray spectroscopy. The inset in (a) displays a cross-sectional HAADF-STEM micrograph together with a Ti map (green color) obtained by energy-dispersive X-ray spectroscopy for the region marked by the green rectangle.

Figure 4.4 (a) shows a typical SEM micrograph of Ti-implanted Si with a fluence of $1.2 \times 10^{16} \text{ cm}^{-2}$ after PLA at 0.8 J/cm^2 . Besides almost round dark-grey areas, light-grey regions are observed in the SEM micrograph. The inset in Fig. 4 (a) shows the atomic-number contrast and the corresponding Ti map (green color) visualized by the high-angle annular dark-field scanning TEM (HAADF-STEM). The light-grey regions in the SEM micrograph belong to a Ti-rich cellular network structure. This network structure consists of (1) walls reaching from the sample surface to around 50 nm in depth and (2) a thin surface layer covering some of the cells formed by the walls mentioned above. According to high-resolution TEM analysis, the Ti-rich walls are characterized by an amorphous microstructure [80]. Hence, for the sample implanted at the highest fluence of $1.2 \times 10^{16} \text{ cm}^{-2}$, a complete cellular breakdown appears at the sample surface, which is due to the occurrence of constitutional supercooling in the molten stage [60, 31, 64]. At high enough impurity concentrations a morphological instability occurs at the liquid-solid interface, resulting in the lateral segregation of Ti impurities and leading to a cellular solidification microstructure. In contrast, there is no cellular breakdown occurring for FLA-treated samples even at the highest Ti fluence as shown in Fig. 4 (b). The light-grey dots correspond to a Ti-rich phase and are isolated from each other. For the sample PLA- $2 \times 10^{15} \text{ cm}^{-2}$, there is no detectable phase separation within the measurement sensitivity. Note that both FLA- $1.2 \times 10^{16} \text{ cm}^{-2}$ and PLA- $2 \times 10^{15} \text{ cm}^{-2}$ are insulating as shown in Fig. 3 (a).

4.3.5 Spatially resolved conduction

The topographical images and the corresponding current maps of Ti-implanted Si samples with fluence of $1.2 \times 10^{16} \text{ cm}^{-2}$ after PLA or FLA are shown in figure 4.5. The solidified cellular microstructure of the PLA sample can be observed in Fig. 4.5 (a). The average cell size, determined to be $\sim 65 \text{ nm}$, is slightly larger than the size obtained from TEM image ($\sim 50 \text{ nm}$) [80]. Instead of cellular microstructures, in Fig.

4.5 (c), the topography of the sample after FLA shows bright spots corresponding to Ti-rich particles on the sample surface according to our TEM analysis [80]. Figure 4.5 (b) and (d) show the overlay of current maps and topography, which provide the information about the local electrical properties of the surface layer. The current maps were measured with a sample bias voltage of +4V. The significant dark blue areas imply current values of 0.3 nA or less. The current map shows cellular breakdown denoted as red spots in Fig. 4.5 (b), pointing out that the surface electrical conductivity is not uniform. The red spots in the current map are almost connected with each other. The dark blue area shows insulating background region. The current maps are well correlated with the topography for both samples. We can clearly observe that the conductive regions are mostly connected after PLA, whereas they are still isolated after FLA. We do believe that in Fig. 4.5 (b) the conducting areas are associated with the cell structure formed during the rapid solidification process after PLA.

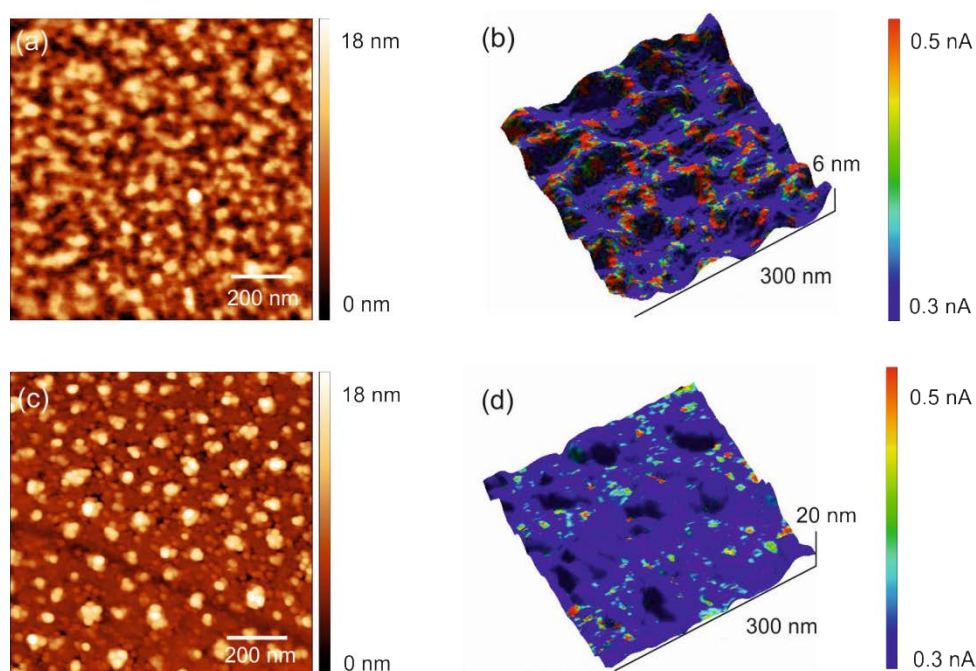


Figure 4.5 C-AFM analysis: (a, c) topography for the PLA/FLA samples, (b, d) overlay of current map and topography for the PLA/FLA samples. Both PLA and FLA sample are implanted with Ti at a fluence of $1.2 \times 10^{16} \text{ cm}^{-2}$.

4.4 Discussion

For the PLA-treated sample, Ti impurities diffuse to the surface and form Ti-rich cell walls. In case of the FLA-treated sample, however, the out-diffusion of Ti is less pronounced (see Fig. 4.1) and hemispherical particles of single-crystalline nature containing Ti and Si are formed beneath the sample surface [80]. For those Ti impurities beneath the surface of the FLA sample, we deduced by using cRBS technique that the majority of the Ti impurities are neither located at the substitutional nor in the interstitial sites with high symmetry. This is actually in agreement with the quantum calculations based on density-functional theory [30]. Neither interstitial nor substitutional Ti implantation process is energetically favorable, however, interstitial Ti is less unstable by 0.65 eV. Experimentally however, we do not exclude the possibility of having Ti atoms located at the interstitial site with a low symmetry [83], i.e. Ti atoms are displaced from the symmetric interstitial site.

The change of the electrical transport properties shown in Fig. 4.3 may be due to the presence of percolation transition. A continuous conduction pathway spanning the sample's dimensions is initially formed at the threshold where the percolation takes place in conducting random networks. Therefore, our results exclude the presence of a Mott-type insulator-to-metal transition in Ti-implanted Si. The metal-like conduction in samples after PLA is ascribed to the percolation of Ti-rich cell walls. Recently, atom probe tomography investigation on Co-implanted Si after PLA revealed that the phase separation does not lead to detectable silicides, but to a single-phase Si highly supersaturated with at least 10% atomic Co [89]. Moreover, our result do not exclude the fact that the infrared optical absorption reported in Ti implanted Si [79, 24] likely comes from the region of Si doped with Ti at very low concentrations, which is far below the cellular breakdown threshold. Our qualitative analysis of the absorption properties by Fourier transform infrared spectroscopy (not shown) demonstrates a near- and mid- infrared optical absorption for both PLA and FLA samples. The measured optical absorption is comparable to that reported for Ti-implanted Si infrared photodetectors [90, 91].

4.5 Conclusion

In summary, we have investigated the structural and electrical properties of Si implanted with Ti at very high concentrations followed by PLA or FLA. We have demonstrated that the implanted samples are recrystallized after both PLA and FLA. C-AFM results exhibit conducting networks associated with cell structures which have been formed during the rapid solidification process during PLA. Temperature-dependent Hall effect measurements have revealed that the sheet resistance decreases with increasing Ti doping concentration for the PLA samples, which is in good agreement with the percolation transition. Our results exclude the occurrence of a Mott-type insulator-to-metal transition in Ti-implanted Si. However, the dilution of Ti ions into the Si matrix at very low concentrations is not discarded, which might be responsible for the infrared optical absorption.

Chapter 5 Realizing the insulator-to-metal transition in Se-hyperdoped Si via non-equilibrium material processing

This chapter has been published:

F. Liu, S. Prucnal, Y. Berencén, Z. Zhang, Y. Yuan, Yu Liu, R. Heller, R. Böttger, L. Rebohle, W. Skorupa, M. Helm, and S. Zhou, ***Realizing the insulator-to-metal transition in Se hyperdoped Si via non-equilibrium material processing***, J. Phys. D: Appl. Phys. 50, 415102 (2017).

We report on the insulator-to-metal transition in Se-hyperdoped Si layers driven by manipulating the Se concentration via non-equilibrium material processing, i.e. ion implantation followed by mill-second flash lamp annealing. Electrical transport measurements reveal an increase of carrier concentration and conductivity with increasing Se concentration. For the semi-insulating sample with Se concentrations below the Mott limit, quantitative analysis of the temperature dependence of conductivity indicates a variable-range hopping mechanism with an exponent of $s = 1/2$ rather than $1/4$, which implies a Coulomb gap at the Fermi level. The observed insulator-to-metal transition is attributed to the formation of an intermediate band in the Se-hyperdoped Si layers.

5.1 Introduction

Recently, many efforts have been focused on exploring intermediate band (IB) materials [92]. The IB permits photons with a low energy below the band gap of the semiconductor to be absorbed, yielding a high optical absorbance in the low energy part of the solar spectrum [93-96]. For deep impurities, like S and Se in Si with a binding energy of around 300 meV [97, 98], the insulator-to-metal transition is a direct evidence for the formation of an IB in host semiconductors [38, 99]. The insulator-to-metal transition controlled by doping occurs at a critical impurity concentration [100]. The growing electron density gives rise to the screening of the Coulomb potential and

results in metallic-like conductivity when the doping concentration is above the Mott limit [38, 100]. Most of the insulator-to-metal transitions are driven by doping semiconductors with shallow dopants, due to their low critical doping concentrations of around 10^{18} cm^{-3} [101]. In contrast, deep-level dopants provide more tightly bound electrons, but need a higher critical doping concentration of $10^{19} \sim 10^{20} \text{ cm}^{-3}$ [9]. However, under thermal equilibrium conditions the solid solubility limits of deep-level dopants are only about 10^{16} cm^{-3} in silicon, which are much lower than those for shallow dopants, viz. around 10^{21} cm^{-3} [7]. In order to overcome the solid solubility limits of deep level dopants in Si, non-equilibrium techniques are needed. Ion implantation is a non-equilibrium technique which can introduce dopants into semiconductors beyond the solid solubility limit. To electrically activate the dopants and to repair the lattice damage induced by energetic ions, a post-implantation annealing is necessary. Both pulsed laser annealing in the nanosecond range [38, 39] and furnace annealing in the minute one [102, 103] have been used to activate S and Se dopants in Si introduced by ion implantation. However, the long-time process required for furnace annealing or even few seconds for rapid thermal annealing will cause large possibilities for impurity diffusion, resulting in a low substitutional fraction [102] or a deactivation of dopants [20]. During pulsed laser annealing the surface temperature exceeds the melting point, subsequently leading to liquid-phase epitaxial regrowth. The main problem of liquid-phase epitaxy is the redistribution of impurities [13] and the cellular breakdown [60]. Alternatively, it has recently been demonstrated that millisecond range flash-lamp annealing (FLA) induces solid phase epitaxy which accounts for a complete recrystallization of the implanted layer at annealing temperatures below the melting point of substrate [104-106]. During this process, the impurities have more probability to be incorporated into the semiconductor lattice due to i) the high velocity of the solidification during recrystallization after FLA and ii) the low diffusion velocity of impurities in the solid phase [71, 107]. It has been shown that FLA is superior to laser annealing in preventing the surface segregation of dopants and in suppressing the cellular breakdown for semiconductors with high impurity concentration [19, 80]. The structural and electrical properties of Se-hyperdoped Si depending on different annealing parameters have been reported in Ref. 21.

In this work, Se-hyperdoped Si samples with different Se concentrations have been fabricated by ion implantation followed by FLA. The insulator-to-metal transition is shown to occur at a Se peak concentration of around $6.3 \times 10^{20} \text{ cm}^{-3}$. Variable-

range hopping with an exponent of $s = 1/2$ is found to be the main electrical transport mechanism for the semi-insulating sample with Se concentrations below the Mott limit. The existence of a Coulomb gap at the Fermi level is also inferred.

5.2 Experimental

Semi-insulating (100) Si wafers with a thickness of 525 μm and a resistivity as large as $10^4 \Omega\cdot\text{cm}$ were used for this investigation. The 4-inch wafers were implanted at energy of 60 keV with Se fluences (Φ) of 1.0×10^{15} , 2.5×10^{15} , and $5 \times 10^{15} \text{ cm}^{-2}$, which results in three different Se peak concentrations (c_{pk}) of 2.5×10^{20} , 6.3×10^{20} , and $1.3 \times 10^{21} \text{ cm}^{-3}$, respectively. c_{pk} is calculated by the following equation: $c_{pk} = \frac{\Phi}{\sqrt{2\pi}\Delta R_p}$, where ΔR_p is the longitudinal straggle [39,108]. The Se peak concentration is chosen to cover the range of the insulator-to-metal transition predicted by density function theory (DFT) [39], Quantum Monte Carlo (QMC) calculations [39] and hybrid functional method [109]. The as-implanted samples were annealed by FLA with fixed pulse duration of 1.3 ms and an energy density of around 20 J/cm^2 in N_2 ambient. Prior to the flash, the samples were preheated up to 400°C for 30 s. The estimated peak temperatures at the sample surface were in the range of $1100\text{-}1200^\circ\text{C}$. Hereafter, the samples will be denoted by their Se peak concentrations unless otherwise stated.

The Raman scattering spectra were obtained using a 532 nm Nd:YAG laser and a charge coupled device camera cooled with liquid nitrogen. The Rutherford backscattering spectrometry (RBS) spectra were measured in both random and channeling geometries. The lattice location of Se in the Si matrix was analyzed by means of channeling Rutherford backscattering spectrometry (cRBS). cRBS measurements were performed with a collimated 1.7 MeV He^+ beam at a 170° backscattering angle. The electrical properties of Se-implanted samples were examined by the van der Pauw configuration using a commercial Lakeshore Hall System in the temperature range of $2.5\text{--}300 \text{ K}$.

5.3 Results

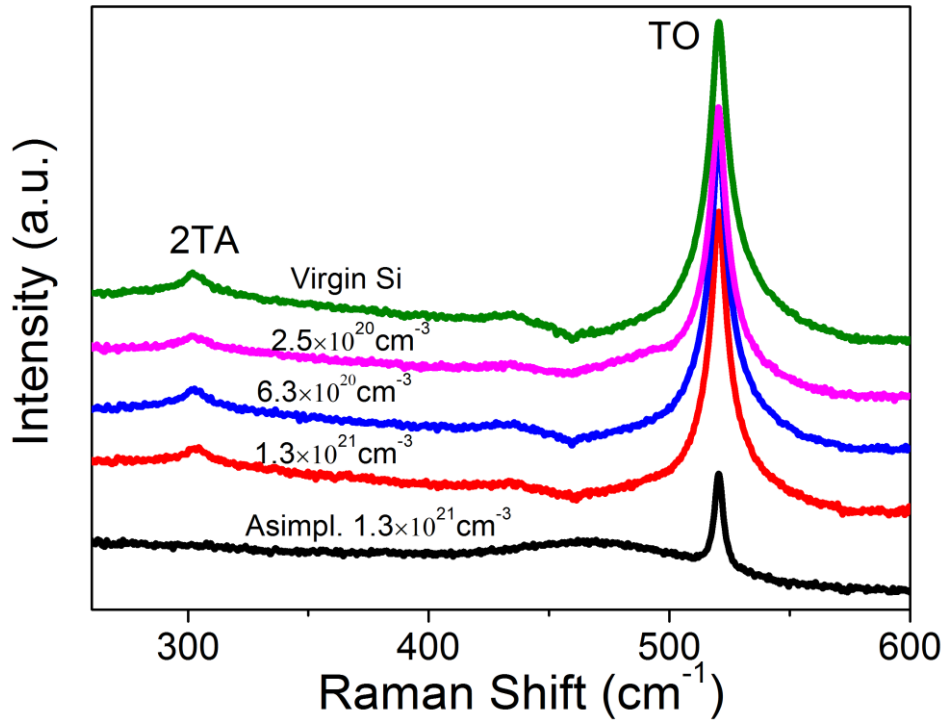


Figure 5.1 Room-temperature Raman spectra of Se implanted Si samples (Se concentrations of 2.5×10^{20} , 6.3×10^{20} , and $1.3 \times 10^{21} \text{ cm}^{-3}$) annealed at 1.3 ms with an energy density of 20 J/cm^2 . For comparison, the spectrum of the virgin Si is also shown.

The regrowth quality of the Se-implanted layers was determined by Raman spectroscopy. Figure 5.1 shows the Raman spectra of the as-implanted and FLA treated samples with different Se peak concentrations. The spectrum of the virgin Si is also included for comparison. The Raman spectrum of virgin Si exhibits a narrow peak at around 520 cm^{-1} which corresponds to the transverse optical (TO) phonon mode of single-crystalline Si. A weak band at around 460 cm^{-1} can be observed in the as-implanted sample, which indicates the formation of an amorphous silicon layer during ion implantation [59, 105]. The peak at around 520 cm^{-1} of the as-implanted sample is from the Si substrate beneath the implanted amorphous layer. However, after FLA the weak band associated with the amorphous layer vanishes, while the intensity of the 520 cm^{-1} Raman peak of crystalline Si restores to that of the virgin Si. The peak observed at 303 cm^{-1} corresponds to the second-order two transverse

acoustic phonon (2TA) scattering mode of single-crystalline Si. Thus, Raman results prove that the crystal order can be well restored using FLA.

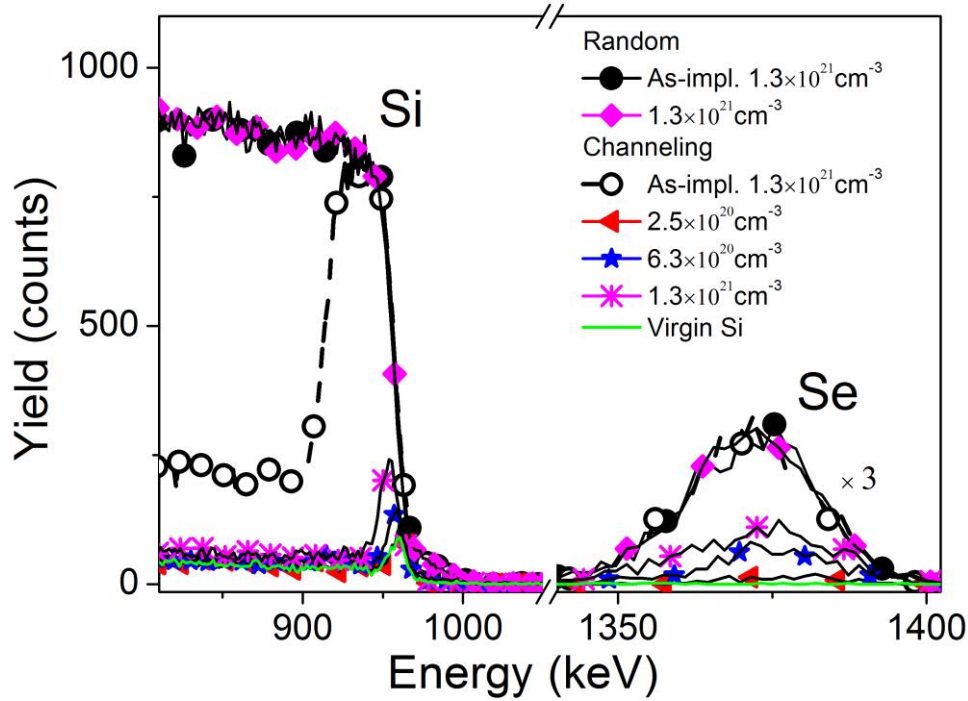


Figure 5.2 RBS spectra of Se implanted Si samples with peak concentration of 2.5×10^{20} , 6.3×10^{20} , and $1.3 \times 10^{21} \text{ cm}^{-3}$ after FLA at 1.3 ms. The spectra for virgin Si are also included for comparison.

In order to further analyze the crystalline properties of Se implanted Si samples after annealing, we performed cRBS measurements. Figure 5.2 shows the RBS spectra of the as-implanted, un-implanted and implanted samples followed by FLA. The channeling spectra were measured along the [100] axis for all samples. The minimum yield χ_{\min} is defined as the ratio of the backscattering yield of the channeling and random spectra, which is an important indicator of the lattice quality [19]. If the implanted layer is fully amorphous, χ_{\min} is 100%, while the χ_{\min} value of 1–2% stands for a high-quality single crystal material. The cRBS spectrum of the as-implanted sample shows a broad damage band located between 900 and 970 keV. The χ_{\min} for the as-implanted sample is calculated to be around 94.3%. The lattice was significantly damaged after Se implantation compared with a fully amorphous layer ($\chi_{\min} \sim 100\%$). After FLA, however, the backscattering yield of all samples is similar to the virgin Si sample, which indicates that of lattice recrystallization has been obtained.

To investigate the lattice location of the Se atom, we show the Se-related peak in figure 5.2. For the sample with the largest Se concentration, the channeling spectrum is significantly reduced in backscattering yield compared to the random spectrum, indicating that around 70% of Se atoms are on a substitutional lattice location [21].

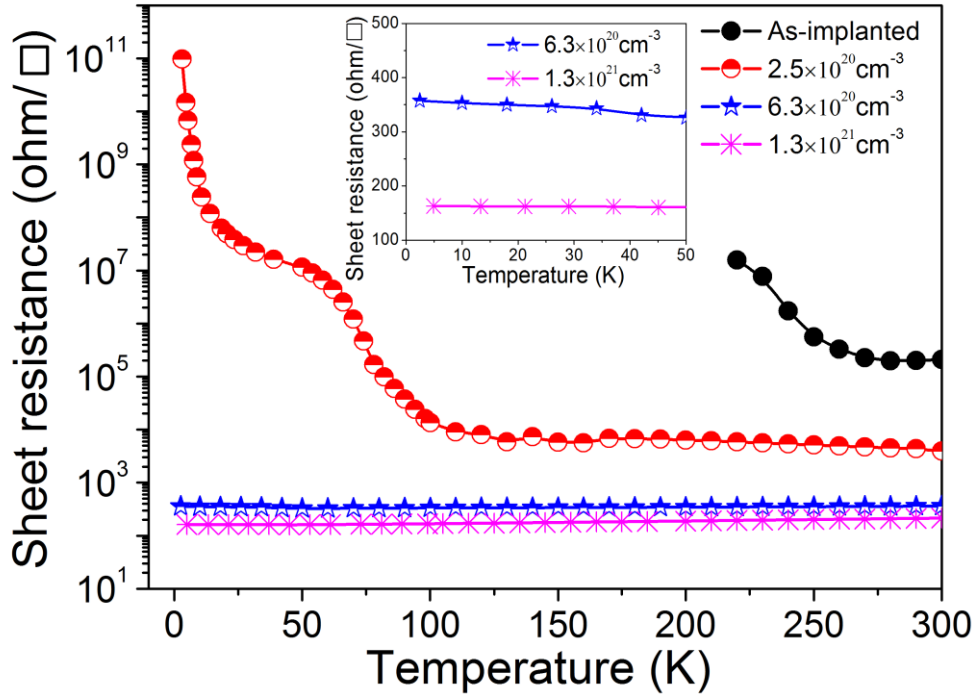


Figure 5.3 Temperature-dependent sheet resistance of Se-hyperdoped Si after FLA. The result for the as-implanted sample ($1.3 \times 10^{21} \text{ cm}^{-3}$) is also shown for comparison. The inset shows the low temperature sheet resistance for samples with Se concentrations of $6.3 \times 10^{20} \text{ cm}^{-3}$ and $1.3 \times 10^{21} \text{ cm}^{-3}$, which is consistent with the prediction in Ref. 21.

In figure 5.3, we present the temperature-dependent sheet resistance over a temperature range of 2.5–300 K for samples with different implantation fluences. A dramatic difference was observed in the sheet resistance for different samples. The sheet resistance of the as-implanted sample ($1.3 \times 10^{21} \text{ cm}^{-3}$) is added for comparison. The sheet resistance of the sample implanted with $2.5 \times 10^{20} \text{ cm}^{-3}$ Se sharply increases at low temperatures, viz. by up to 9 orders of magnitude compared to the sample with higher Se peak concentration ($1.3 \times 10^{21} \text{ cm}^{-3}$). The conductivity of this sample is thermally activated. The sample with the Se peak concentration of $6.3 \times 10^{20} \text{ cm}^{-3}$ shows finite conductivity as the temperature approaches zero and exhibits a metallic-like behavior. However, the sheet resistance of this sample slightly

increases at low temperatures (see inset in figure 5.3). The sample with the Se peak concentration of $1.3 \times 10^{21} \text{ cm}^{-3}$ has the lowest sheet resistance and its value does not increase at low temperatures (see inset in figure 5.3). The insulator-to-metal transition in FLA-processed samples occurs at a Se peak concentration around $6.3 \times 10^{20} \text{ cm}^{-3}$. From DFT calculations performed by Ertekin *et al.* [39] a critical Se concentration of 1/249 (around $2.0 \times 10^{20} \text{ cm}^{-3}$) has been obtained. On the other hand, QMC calculations conducted by the same group predict a critical concentration of 1/128 (around $3.9 \times 10^{20} \text{ cm}^{-3}$). The relatively large discrepancy implies that the electron correlation effect should be considered. Additionally, Shao *et al.* [109] have employed a hybrid functional method for Se-hyperdoped Si and predicted a critical concentration of $5.09 \times 10^{20} \text{ cm}^{-3}$ at which the defect states merge into the conduction band. Our experimental results are in line with the critical values obtained by different theory approaches.

According to Hall Effect measurements at room temperature, we calculate the carrier concentration by taking into account the effective thickness (d_{eff}) defined as $d_{\text{eff}} = \Phi/c_{\text{pk}}$ [38], which is 40 nm for all samples. The deduced carrier concentrations are 5.1×10^{18} , 7.3×10^{19} , and $9.0 \times 10^{19} \text{ cm}^{-3}$ for samples with Se peak concentrations of 2.5×10^{20} , 6.3×10^{20} , and $1.3 \times 10^{21} \text{ cm}^{-3}$, respectively. So apparently the activation fraction (the ratio between the carrier concentration and the Se concentration) is only between 2% and 11%, a fact which is the subject of further investigation. The Mott criterion can be calculated from the equation $n_c^{1/3} a_B = 0.26 \pm 0.05$. The effective Bohr radius of a_B is around 0.3 nm calculated by using the binding energy 200 meV for Se in Si [97, 98]. Thus, the critical concentration n_c is around $6 \times 10^{20} \text{ cm}^{-3}$, which is larger than the measured carrier concentration for the metallic-like sample. The discrepancy can be due to the low-estimated carrier concentration from the experimental data, i.e., the peak carrier concentration can be higher. It also can be due to the shrinking of the binding energy of Se in Si with increasing the impurity concentration. According to the results mentioned above, we can conclude that the insulator-to-metal transition occurs in Se-hyperdoped Si fabricated by ion implantation and FLA. The conductivity of the sample with the Se peak concentration of $6.3 \times 10^{20} \text{ cm}^{-3}$ is around 700 $\Omega^{-1}\text{cm}^{-1}$ at low temperatures (2.5 K), which is comparable with the value of 600 – 800 $\Omega^{-1}\text{cm}^{-1}$ for the laser annealed sample with the Se peak concentration of $1.0 \times 10^{21} \text{ cm}^{-3}$, reported in Ref. 39.

In order to gain further insight into the underlying physics behind the electrical properties of our samples, an experimental data modelling was performed by taking into account the Mott's theory about conduction mechanisms in insulating materials [38]. According to this theory, the conduction of Mott insulators proceeds by electron hopping between localized states at low-temperatures [111]. The insulating samples can therefore be modelled in terms of the conductivity as a function of temperature as follows:

$$\sigma(T) = \sigma_0 \exp [-(T_0/T)^s], \quad (5.1)$$

being σ_0 a prefactor, T_0 the activation temperature and s an exponent that defines the different hopping transport regimes. In detail, $s = 1$ corresponds to nearest-neighbor hopping, $s = 1/2$ implies a variable range hopping with a Coulomb gap in the density of states (DOS) and $s = 1/4$ stands for a Mott's variable range hopping [112].

Our experimental data were fitted by using Eq. (5.1) with the exponent of $s = 1$, $1/2$, and $1/4$, respectively. Only $s = 1/2$ exponent was found to provide a good agreement at temperatures above 10 K as seen in Fig. 5.4. The activation temperature T_0 is also deduced to be 519 K (44 meV).

Alternatively, Zabrodskii [111] proposed a graphical differentiation procedure to readily identify the different hopping transport regimes. This lies on introducing a $W(T)$ defined as

$$W(T) = \frac{d \ln(\sigma)}{d \ln(T)} \quad (5.2)$$

Hence, the equation (5.3) is obtained by inserting (5.1) into (5.2):

$$W(T) = s \left(\frac{T_0}{T} \right)^s \quad (5.3)$$

From this equation, the value of s can easily be inferred from the slope of the $\text{Log}(W) - \text{Log}(T)$ representation. Based on this, a value of 0.53 ± 0.01 is obtained as shown in inset in figure 5.4. This suggests the presence of a Coulomb gap at the Fermi level giving rise to a variable range hopping mechanism [112]. The Coulomb gap vanishes as the Se-hyperdoped Si layers become more conducting.

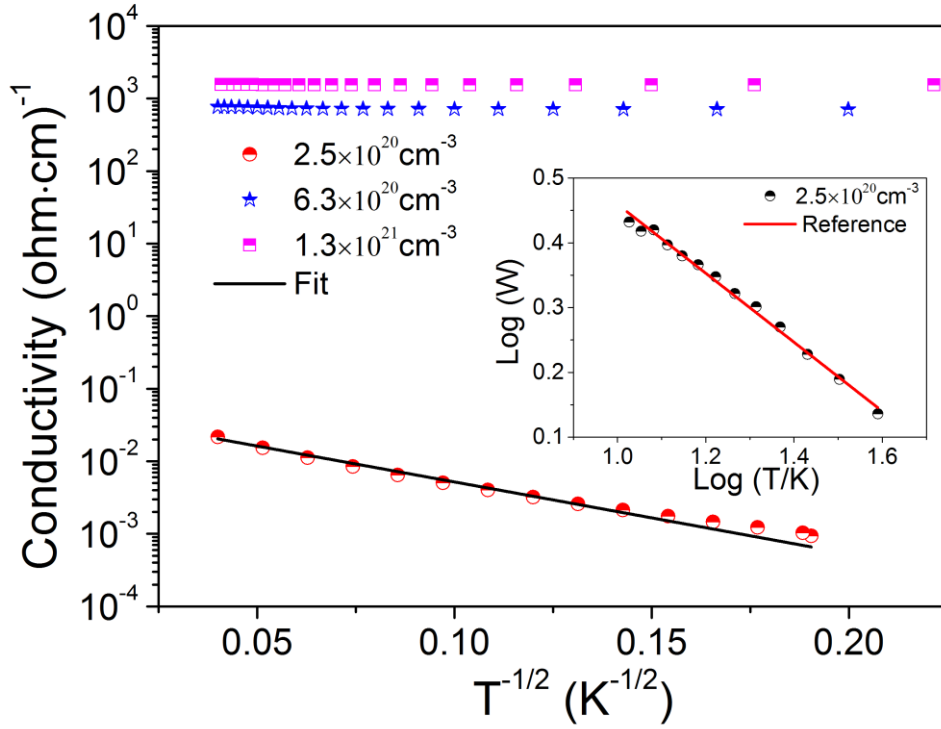


Figure 5.4 Conductivity of the semi-insulating sample as a function of $T^{-1/2}$: the solid line is a fit of the experimental data to Eq. (1) with $s = 1/2$. The fitting range is $10 \text{ K} < T < 50 \text{ K}$. The fit for the insulating sample yields $s = 0.53 \pm 0.01$. The inset shows the value of s identified by the slope of $W(T) = \frac{d \ln(\sigma)}{d \ln(T)}$ versus T on a log scale. The red solid line shows $s = 0.50$ for reference.

5.4 Conclusions

We have investigated the structural and electrical properties of single-crystalline Si implanted with Se followed by FLA. From Raman and RBS/C results, it has been demonstrated that high crystalline quality of the implanted samples has been achieved after FLA. Increasing the Se doping concentration from 2.5×10^{20} to $6.3 \times 10^{20} \text{ cm}^{-3}$ (less than 3 times) resulted in a conductivity enhancement of several orders of magnitude, leading to metallic-like behavior and demonstrating an insulator-to-metal transition among these values. This is in quantitative agreement with the values predicted from DFT and QMC calculations. Based on the temperature-dependent electrical measurements, the semi-insulating samples have revealed variable-range-hopping conduction with a Coulomb gap at the Fermi level. It is worth to note that the whole processing (ion implantation + flash lamp annealing) is

compatible with the Si-based chip technology and can be easily integrated with the existing production line.

Chapter 6 Structural and electrical properties of Se-hyperdoped Si via ion implantation and flash lamp annealing

This chapter has been published:

F. Liu, S. Prucnal, Y. Yuan, R. Heller, Y. Berencén, R. Böttger, L. Rebohle, W. Skorupa, M. Helm, and S. Zhou, ***Structural and electrical properties of Se-hyperdoped Si via ion implantation and flash lamp annealing***, Nuclear Inst. and Methods in Physics Research B. 424, 52-55 (2018).

We report on the hyperdoping of silicon with selenium obtained by ion implantation followed by flash lamp annealing. It is shown that the degree of crystalline lattice recovery of the implanted layers and the Se substitutional fraction depend on the pulse duration and energy density of the flash. While the annealing at low energy densities leads to an incomplete recrystallization, annealing at high energy densities results in a decrease of the substitutional fraction of impurities. The electrical properties of the implanted layers are well-correlated with the structural properties resulting from different annealing processing.

6.1 Introduction

Silicon hyperdoped with chalcogens with the doping concentration far exceeding the solid solubility limits has recently gained much attention due to its unique optical and electrical properties. This new class of materials is obtained by introducing chalcogens into Si at concentrations far above the solid solubility limit, which gives rise to the formation of an impurity band (IB). This fact allows for a strong sub-band photoresponse [113, 114] and an insulator-to-metal transition [38, 39]. Such properties can be used for developing intermediate band solar cells [34-36] and infrared photodiodes [33, 31, and 73]. However, the formation of the IB in Si with chalcogens is very challenging due to the following reasons: (1) The solid solubility limits of chalcogens such as S and Se in Si are lower than 10^{16} cm^{-3} [7], which is far below the Mott limit of $\sim 5.9 \times 10^{19} \text{ cm}^{-3}$ [9] and (2) chalcogens have a large diffusion

coefficients in Si [115], resulting in the redistribution and segregation of impurities on the sample surface. Ion implantation followed by either pulsed laser annealing (PLA) or flash lamp annealing (FLA) is known as non-equilibrium method to introduce impurity into the semiconductors well above the solubility limit. The resulting hyperdoped materials formed by ion implantation and pulsed laser annealing show an insulator-to-metal transition, which provides a powerful proof for the formation of IB in Si [38, 39, and 99].

In this paper, we present the structural and electrical properties of Si hyperdoped with Se by ion implantation and FLA. The millisecond time duration of FLA induces a solid phase epitaxy of the implanted layer and the incorporation of Se into Si lattice sites. The structural properties of the Se-hyperdoped Si layers are investigated by Raman spectroscopy and Rutherford backscattering spectrometry/channeling (RBS/C). A correlation between the structural and the electrical properties under different annealing processes is established.

6.2 Experimental

Semi-insulating Si (001) wafers with a thickness of 525 μm , (resistivity larger than $10^4 \Omega\cdot\text{cm}$; single-side polished) were implanted at energy of 60 keV with Se ions at a fluence (Φ) of $5 \times 10^{15} \text{ cm}^{-2}$ at room temperature, which results in a Se peak concentration (c_{pk}) of $1.3 \times 10^{21} \text{ cm}^{-3}$, c_{pk} is calculated by the following equation: $c_{\text{pk}} = \frac{\Phi}{\sqrt{2\pi}\Delta R_P}$, where ΔR_P is the longitudinal straggle [39, 116]. The depth profile of selenium in Si after FLA or PLA was calculated from RBS spectra [21]. The profile of selenium in FLA samples is in a reasonable agreement with Stopping and Range of Ions in Matter (SRIM) simulation. Subsequent FLA [46, 117] was performed to recrystallize the amorphous layers after implantation. The as-implanted samples were annealed with pulse durations of 1.3, 3 or 20 ms. Right prior to the flash, the samples were preheated up to 400 °C for 30 s. The preheating prior the FLA process was used to reduce the temperature gradient in the sample during ms-range pulse annealing. The estimated peak temperatures at the sample surface were in the range from 1100 °C to 1200 °C. The optimized annealing energy densities for 1.3, 3, and 20 ms were 20, 27, and 36 J/cm^2 , respectively. We optimized annealing parameters based on the data obtained by both Raman spectroscopy and RBS/C by considering the best crystalline quality and the largest dopant substitutional fraction.

Raman spectroscopy was carried out to determine the crystallinity degree of the implanted layers using a 532 nm Nd:YAG laser and a charge coupled device camera cooled with liquid nitrogen. RBS/C was performed in order to investigate the degree of lattice reconstruction of the samples and the lattice location of Se in the Si matrix after annealing. For RBS/C measurements a collimated 1.7 MeV He⁺ primary beam was used, while the detector was placed at a backscattering angle of 170°. The RBS spectra were measured along random and channeling directions. Electrical properties were investigated by van der Pauw measurements using a commercial Lakeshore Hall System at temperatures ranging from 3 to 300 K.

6.3 Results

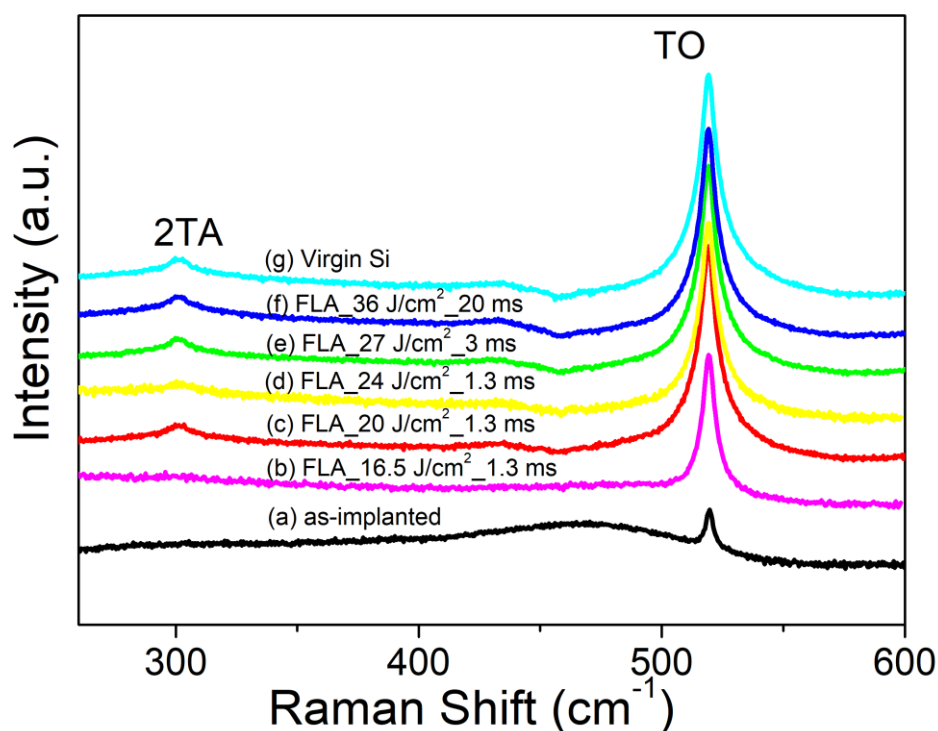


Figure 6.1 Room-temperature Raman spectra of virgin Si (g), as-implanted Si (a), and Se-hyperdoped Si samples with a fluence of $5 \times 10^{15} \text{ cm}^{-2}$ annealed at different pulse duration and different energies: (b) 16.5 J/cm², 1.3 ms; (c) 20 J/cm², 1.3 ms; (d) 24 J/cm², 1.3 ms; (e) 27 J/cm², 3 ms; (f) 36 J/cm², 20 ms. Samples right prior to the flash were preheated to 400 °C for 30 s.

Raman spectra obtained from samples annealed at different energy densities and FLA pulse durations are shown in Fig. 6.1. A spectrum of a virgin Si wafer is displayed for comparison. The Raman spectrum of virgin Si shows a narrow peak at about 520 cm^{-1} which corresponds to the transverse optical (TO) phonon mode in single-crystalline Si. The spectrum of the as-implanted sample shows a peak at around 520 cm^{-1} with a relatively low intensity, which relates to the TO mode of single crystalline Si substrate beneath the implanted amorphous layer. The observation of a weak band at around 460 cm^{-1} in the as-implanted sample indicates the formation of an amorphous silicon layer during ion implantation process [59]. In Fig. 6.1 (b), the weak band at 460 cm^{-1} is still observed in the sample annealed at 16.5 J/cm^2 for 1.3 ms, suggesting that the used energy density was not enough for the entire solid-phase epitaxial regrowth. However, the weak band vanishes in the spectra of the sample annealed at 20 and 24 J/cm^2 . The sample shows a peak at around 520 cm^{-1} which is similar to the single crystalline Si. In addition, another peak located at 303 cm^{-1} corresponds to the two transverse acoustic (2TA) phonon mode of single crystalline Si. From the above-mentioned results, a full lattice reconstruction is obtained by flash pulse duration of 1.3 ms and energy densities of 20 or 24 J/cm^2 . From spectra c, e and f shown in Fig. 6.1, we observe that Se-hyperdoped Si can be recrystallized using any pulse duration if the energy density is properly chosen. The optimized energy density which was selected according to Raman spectroscopy and RBS/C for FLA pulse durations of 3 ms and 20 ms is 27 J/cm^2 and 36 J/cm^2 , respectively. The TO and 2TA modes of single crystalline Si are visible in all the samples annealed by different FLA pulse durations, which are similar to the virgin Si in terms of intensity. Raman results indicate that implanted samples can be well-recrystallized by the proper adjustment of FLA pulse duration and energy density.

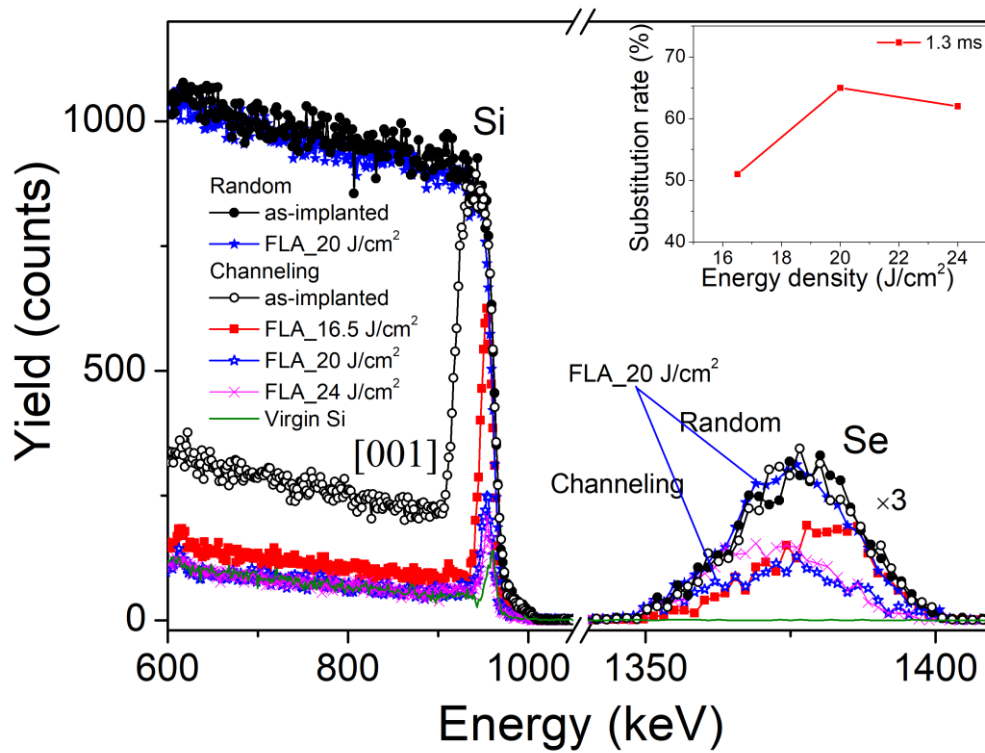


Figure 6.2 RBS spectra of Se implanted Si samples with a fluence of $5 \times 10^{15} \text{ cm}^{-2}$ at random and channeling configuration before and after annealing. The RBS spectra for virgin Si are also included for comparison. The inset shows the substitutional fraction of samples annealed at different energy densities.

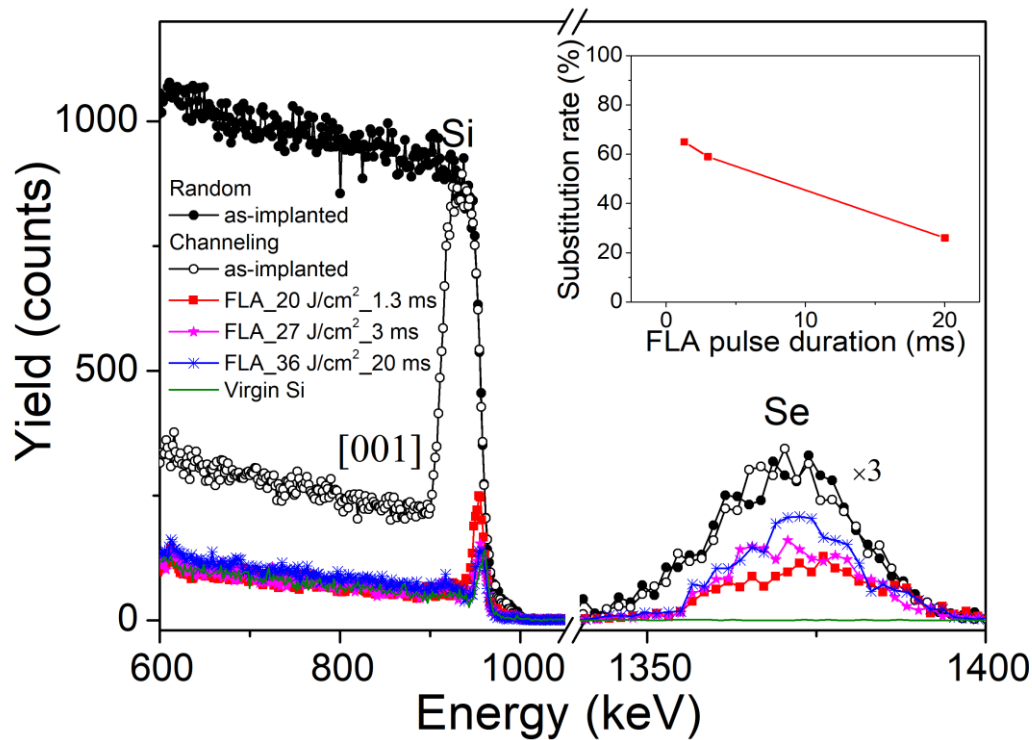


Figure 6.3 RBS spectra of Se implanted Si samples with a fluence of $5 \times 10^{15} \text{ cm}^{-2}$ and FLA at energy densities of 20, 27, and 36 J/cm^2 with the pulse duration of 1.3, 3, 20 ms, respectively. The spectrum of the virgin Si is shown for comparison. The inset shows the substitutional fraction of implanted Se under different FLA pulse durations.

The crystalline quality and lattice location of the Se implanted Si samples after FLA were determined by RBS/C. Fig. 6.2 shows the random and channeling spectra of implanted samples after FLA at energy densities of 16.5, 20, and 24 J/cm^2 with the pulse duration of 1.3 ms. A minimum yield χ_{\min} is defined as the ratio of the backscattering yield of channeling to that of random spectra, which exhibits the overall level of the lattice quality [110]. If the sample is fully amorphous, χ_{\min} is 100%, and then a high-quality single-crystal has a χ_{\min} as low as 1–2%. The as-implanted sample shows a χ_{\min} of 94.3%, which is indicative of the formation of amorphous Si layers. The yield of the damage peak decreases as the flash lamp energy density increases. In the case of samples annealed for 1.3 ms with energy densities below 16.5 J/cm^2 only partial recrystallization was observed with χ_{\min} of around 15%. There is no significant difference in the value of χ_{\min} when the energy density rises to 20 J/cm^2 and 24 J/cm^2 . The channeling spectra obtained from samples annealed at 20 J/cm^2 and 24 J/cm^2 look very similar to the virgin Si. The χ_{\min} values of samples

annealed at 20 J/cm² and 24 J/cm² are around 4%, which indicates a high degree of lattice recovery. The channeling spectra were also measured along the <110> axis for selected samples (not shown) and the Se signal also shows channeling behavior with a similar χ_{\min} .

The inset of Fig. 6.2 shows the substitutional fraction of samples annealed at different energy densities. The substitution of selenium into the Si lattice can be demonstrated by the presence of the channeling behavior. The substitutional fraction f of Se in Si can be calculated by $f = \frac{1-\chi_{\min(I)}}{1-\chi_{\min(h)}}$, where $\chi_{\min(I)}$ and $\chi_{\min(h)}$ are the minimum yield for Se and Si atoms, respectively [48]. Thus the corresponding substitutional fractions of samples annealed at 16.5, 20, and 24 J/cm² are 51%, 65% and 62%, respectively. The sample annealed at 20 J/cm² exhibits the largest substitutional fraction due to the high degree of lattice recrystallization. Alternatively, for the sample annealed at 24 J/cm², the substitutional fraction is slightly lower than that of the sample annealed at 20 J/cm². This is attributed to the fact that the sample is overheated and Se atoms start to segregate. When the energy density is below 20 J/cm², amorphous Si layers cannot be fully recrystallized, resulting in the lowest substitutional fraction of the Se.

RBS/C spectra of Se implanted Si samples are shown in Fig. 6.3 for FLA at energy densities of 20, 27, and 36 J/cm² with the pulse duration of 1.3, 3, 20 ms, respectively. The minimum yield χ_{\min} of samples annealed at 1.3, 3 and 20 ms is 4, 3.3 and 3.1%, respectively. The crystal order is well recovered by different FLA pulse durations. As shown in inset of Fig. 6.3, the substitutional fraction decreases with the increasing FLA pulse duration from 1.3 to 20 ms. This probably can be explained by the diffusion of Se during the FLA process where the diffusion length is defined as $L = (2Dt)^{1/2}$, D is the diffusion coefficient [14] and t the annealing time. If the sample is annealed for a longer time, then the diffusion length is expected to be larger. However, from our RBS measurement we do not see the diffusion of Se within our detection limit. Nevertheless, a relatively short annealing time should be chosen to have high impurity concentrations on the substitutional sites.

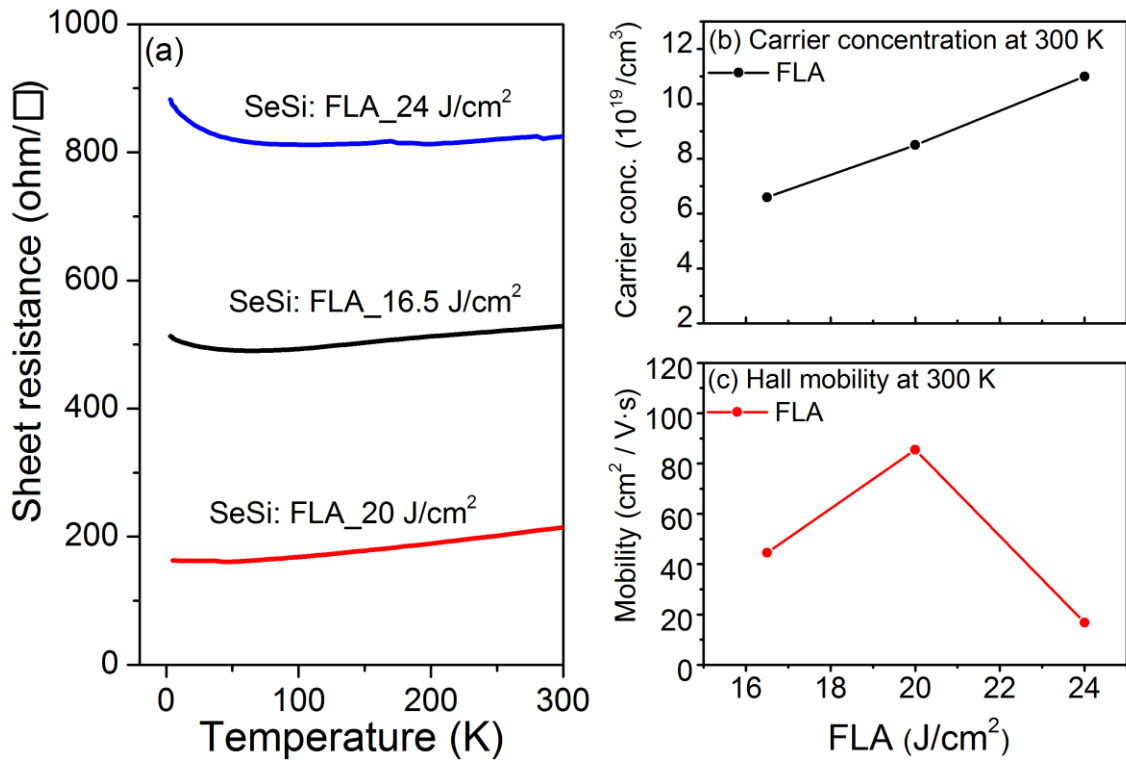


Figure 6.4 (a) Temperature-dependent sheet resistance, (b) The carrier concentration and (c) Hall mobility of Se hyperdoped Si with a fluence of $5 \times 10^{15} \text{ cm}^{-2}$ after FLA at energy densities of 16.5, 20, and 24 J/cm². The FLA pulse duration was fixed at 1.3 ms.

Fig. 6.4(a) shows the sheet resistance as a function of the temperature in the range of 3–300 K for samples annealed at energy densities of 16.5, 20, and 24 J/cm². The amorphous layer is not well crystallized when the energy density is below 20 J/cm² (see Fig. 6.2). In comparison with the 20 J/cm² annealed sample, a higher resistance of around 500 Ω/sqr is observed for the 16.5 J/cm² annealed sample. It is worth noting that the highest resistance of 800 Ω/sqr is found for the 24 J/cm² annealed sample. The lowest resistance of the sample annealed at 20 J/cm² indicates that both the full crystallization and the large substitutional fraction are simultaneously achieved when annealed at such optimal conditions. The sheet resistance slightly increases at low temperatures for the other samples, while the weak temperature-dependent feature of the sample annealed at 20 J/cm² indicates a metallic-like behavior.

The carrier concentration and Hall mobility measured at 300 K of the samples annealed at different flash lamp energy densities are depicted in Fig. 6.4 (b) and (c), respectively. As shown in Fig. 6.4 (b), the carrier concentration increases with increasing annealing energy. We calculate the carrier concentration by taking into account the effective thickness (d_{eff}) defined as $d_{\text{eff}} = \Phi / c_{\text{pk}}$ [38], which is 40 nm for all samples. Consequently, the carrier concentration is in the range of $6.7\text{--}11.0 \times 10^{19} \text{ cm}^{-3}$. The Hall mobility of all samples is in the range of $17\text{--}85 \text{ cm}^2/\text{V}\cdot\text{s}$. The conductivity of the sample annealed at 20 J/cm^2 is the highest, due to the largest Hall mobility, although the carrier concentration is lower than that of the sample annealed at 24 J/cm^2 . This is due to the large substitutional fraction and the high degree of lattice recrystallization, which lead to a larger mobility in the sample annealed at 20 J/cm^2 . In addition, charge carrier scattering increases with increasing carrier concentration which contributes to the low mobility in case of 24 J/cm^2 . Note that the sample annealed at 24 J/cm^2 has a larger carrier concentration than the sample annealed at 20 J/cm^2 although it has a smaller substitutional fraction. It is very puzzling. Defects due to the overheating at larger energy density may contribute additional electrons with reduced mobility. However, this puzzling needs further exploration.

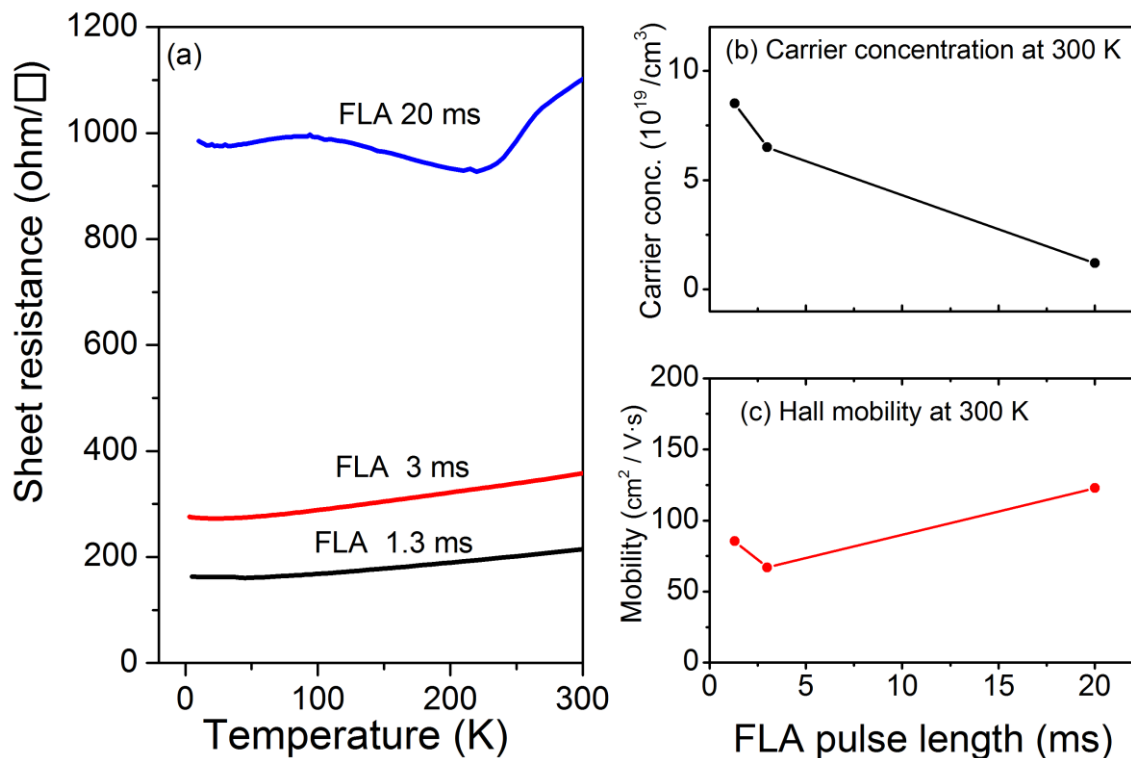


Figure 6.5 (a) Temperature-dependent sheet resistance, (b) The carrier concentration and (c) Hall mobility of Se implanted Si samples with a fluence of $5 \times 10^{15} \text{ cm}^{-2}$ annealed at various pulse duration of 1.3, 3, 20 ms with energy densities of 20, 27, and 36 J/cm^2 , respectively.

Temperature-dependent sheet resistance of Se implanted samples annealed at different pulse durations (1.3–20 ms) are shown in Fig. 6.5 (a). It can be seen that the sheet resistance increases with increasing the pulse duration from 1.3 to 20 ms. The evolution of the sheet resistance as a function of the temperature for both samples (FLA 1.3 ms and FLA 3 ms) show a similar behavior. At low temperatures, the sheet resistance of both samples slightly decreases with increasing temperature. As temperature approaches zero, both samples show finite conductivity. Therefore, the samples annealed at 1.3 and 3 ms exhibit the metallic-like behavior. However, the temperature dependence of the sheet resistance for the sample annealed at 20 ms shows completely different behavior compared with the other samples. The sheet resistance of this sample (FLA 20 ms) is roughly ten times larger than that of the other samples (FLA 1.3 ms). This is probably due to the fact that most Se atoms re-incorporated into clusters.

The carrier concentration and Hall mobility measured at 300 K of the samples annealed at different pulse durations of 1.3–20 ms are shown in Fig. 6.5 (b) and (c). In Fig. 6.5 (b), the carrier concentration decreases with increasing pulse duration. The carrier concentration and Hall mobility of FLA samples are in the range of $1.2\text{--}8.5 \times 10^{19} \text{ cm}^{-3}$ and $67\text{--}123 \text{ cm}^2 / \text{V}\cdot\text{s}$, respectively. The sample annealed at 1.3 ms has the largest conductivity due to the largest carrier concentration and relatively high Hall mobility resulting from the large substitutional fraction and high degree of lattice recovery.

6.4 Conclusions

We investigated the structural and electrical properties of the single crystalline Si samples implanted with Se at fluences as high as $5 \times 10^{15} \text{ cm}^{-2}$ followed by FLA. From Raman and RBS/C results, it was demonstrated that the epitaxial regrowth of the implanted sample can be achieved during ms-range FLA. The sample annealed at short pulse duration (1.3 ms) shows better conductivity than those ones annealed at long pulse durations (20 ms). The electrical properties of the hyperdoped layers

have been well-correlated with the structural properties resulted from different annealing processing.

Chapter 7 Summary and outlook

7.1 Summary

In this thesis, Ti and Se hyperdoped Si with doping concentration much above the solid solubility limits were fabricated by ion implantation followed by PLA and FLA, respectively. We presented the analysis of the surface morphology, structural and electrical properties of the implanted layers after annealing. The implanted layers were studied by Raman spectroscopy to investigate the recrystallization of the implantation-induced amorphous layer, confirming that the crystalline order can be well recovered after PLA or FLA. To study in details the crystallization process, RBS channeling spectroscopy was performed on the samples before and after annealing. The lattice location, and the depth distribution of the dopants in Si after sub-second annealing have been determined also by RBS channeling. SEM and TEM were applied to characterize the surface morphology and to qualitatively analyze the depth and lateral compositional distribution, respectively. C-AFM was performed using tips with approx. 100 nm thick conductive diamond-like carbon coating to correlate the electrical conduction with the surface morphology. Electrical properties of implanted samples were examined using a commercial Lakeshore Hall System in the van-der-Pauw geometry.

PLA has been widely used to anneal Ti and chalcogen-ion-implanted Si. Using PLA, the surface layer can be molten in the nanosecond range and recrystallized via liquid-phase epitaxy. The supersaturation is due to solute trapping at the moving amorphous/crystalline interface when the solidification velocity is larger than the diffusive velocity. The out-diffusion of impurities happens when the diffusive velocity is larger than the solidification velocity during recrystallization. Different from PLA, FLA in millisecond range can render the sample just slightly below the melting temperature, leading to a solid-phase epitaxy.

As discussed in Chapter 3, Ti implanted Si layer can be well realized by ion implantation followed by PLA and FLA. In both cases, the implantation concentrations of Ti are well above the solid solubility limit and also well above the Mott limit. We find that sample annealed by PLA shows the so-called growth interface breakdown or cellular breakdown owing to the occurrence of constitutional supercooling in the melt. At high enough impurity concentrations, a morphological

instability occurs at the liquid-solid interface, resulting in the lateral segregation of Ti impurities and leading to a cellular solidification microstructure. The appearance of cellular breakdown prevents impurity incorporation into the single crystalline Si matrix. In terms of preventing surface segregation, FLA is superior to PLA because the cellular breakdown can be avoided leading to a much higher incorporation concentration.

In order to determine the location of the Ti atoms within the Si lattice in the FLA treated samples, RBS/channeling measurements were performed on the samples as shown in chapter 4. We confirm that Ti atoms are located neither at substitutional Si sites nor bond-centered interstitial sites after either FLA or PLA treatment. The decrease of the sheet resistance with increasing Ti concentration is attributed to a surface morphology effect due to the formation of cellular breakdown at the surface. And the C-AFM results show that the surface electrical conductivity is not uniform in the PLA sample, and we believe that the conducting areas are associated with the cell structure formed during the rapid solidification process after PLA. Therefore, our results exclude the presence of a Mott-type insulator-to-metal transition in Ti-implanted Si. The metal-like conductivity in the PLA samples is due to the percolation associated with the cellular breakdown at the surface, while the conductive regions are still isolated after FLA. This is in a good agreement with the results obtained by TEM in chapter 3. In chapter 3, we found that Ti impurities diffuse to the surface and form Ti-rich cell walls in the PLA-treated sample. For the FLA-treated sample, the out-diffusion of Ti is less pronounced and hemispherical particles of single-crystalline nature containing Ti and Si beneath the sample surface are formed. In contrast, we cannot observe the redistribution of Ti in RBS spectra before and after FLA. This may result from only a few hemispherical particles of Ti located beneath the sample surface, and therefore RBS measurement is not able to detect them.

In Chapter 5, we presented the structural and electrical properties of single-crystalline Si implanted with Se followed by FLA. We determined that around 70% of Se atoms are on the substitutional lattice location by RBS/channeling. Increasing the Se doping concentration from 2.5×10^{20} to $6.3 \times 10^{20} \text{ cm}^{-3}$ (less than 3 times) resulted in a conductivity enhancement of several orders of magnitude, leading to metallic-like behavior and demonstrating an insulator-to-metal transition. The observed insulator-to-metal transition is attributed to the formation of an intermediate band in the Se-hyperdoped Si layers. For the semi-insulating sample with Se

concentrations below the Mott limit, quantitative analysis of the temperature dependence of conductivity indicates a variable-range hopping mechanism with an exponent of $s = 1/2$ rather than $1/4$, which implies a Coulomb gap at the Fermi level.

The relationship between the Se substitutional fraction and the pulse duration of FLA is described in chapter 6. The substitutional fraction decreases with the increasing FLA pulse duration from 1.3 to 20 ms. The sample annealed at short pulse durations (1.3 ms) shows larger conductivity than those annealed at long pulse durations (3 and 20 ms). The electrical properties of the hyperdoped layers have been well-correlated with the structural properties resulted from different annealing processing.

If we compare the results obtained for Ti and Se implanted Si, a question arises: why hyperdoping in Si could be reached for Se but not for Ti impurities?

The hyperdoping is due to solute trapping at the moving amorphous/crystalline interface when the solidification velocity is larger than the diffusive velocity. The out-diffusion of impurities happens when the diffusive velocity is larger than the solidification velocity during the recrystallization. The diffusion coefficient plays an important role during this process. For most of dopants, the diffusion coefficient is much larger in liquid phase than in solid phase. As we discussed in chapter 3, transition metals have larger diffusive velocity than the crystallization velocity in liquid phase epitaxy. This is the reason that Ti diffusion towards the surface and cellular breakdown occurs in PLA. FLA is a solid-phase process which has a relatively higher velocity of the amorphous-crystalline interface and a much lower diffusion velocity. This is why Ti redistribution can be suppressed in the FLA sample. However, RBS/channeling results show that Ti atoms are located neither at substitutional nor interstitial sites for both PLA and FLA samples.

Se implanted Si shows a substitutional fraction of around 70% with a doping concentration up to 2.3% after FLA. While at the same doping concentration, PLA sample has a substitutional fraction of around 40%. This is due to the diffusion coefficient is much larger in liquid phase than in solid phase. As we show in Figure 1.3, the diffusion coefficient of Ti is around $5 \times 10^{-11} - 4 \times 10^{-10} \text{ cm}^2/\text{sec}$ in the temperature range from 1000 °C to 1250 °C, whereas it is $1.1 \times 10^{-11} - 1.0 \times 10^{-9} \text{ cm}^2/\text{sec}$ for Se in the temperature range from 1000 °C to 1260 °C. Se has even slightly higher diffusion coefficient at high temperature range. In this case, the observation that Ti atoms are not in ordered lattice sites and Se atoms are in

substitutional sites in Si is rather puzzling. One reason could be the diffusion coefficient is strongly depending on the impurity concentration. The diffusion coefficient data we quote here was generally determined at low impurity concentration (under thermal equilibrium condition). We have implanted both Ti and Se with their concentrations much above the thermal equilibrium concentration. At high impurity concentration, the diffusion coefficient for Se can be changed, probably much lower than the quoted data. However, a further investigation is needed to clarify this issue.

7.2 Outlook

Although the structural and electrical properties of Ti and Se hyperdoped Si have been studied in details, there are some ideas worth being investigated as further work. The following three points can be considered:

- (1) In this thesis, Ti-hyperdoped Si was fabricated by ion implantation followed by PLA and FLA. The problem of the PLA-treated sample is the cellular breakdown happens at high Ti doping concentration, preventing supersaturation. In terms of preventing surface segregation, FLA is superior to PLA because the cellular breakdown can be avoided leading to a much higher incorporation concentration. However, the hemispherical particles of single-crystalline nature containing Ti and Si beneath the sample surface are formed in the FLA-treated sample. For those Ti impurities beneath the surface, RBS/channeling results show that the majority of the Ti impurities are neither in the substitutional nor in the interstitial sites. In the future, one can implant Ti with the fluence between $1.2 \times 10^{16} \text{ cm}^{-2}$ and $2 \times 10^{15} \text{ cm}^{-2}$ and investigate the structural and electrical properties of the implanted layers. One might get a chance to avoid the cellular breakdown and obtain the wanted optoelectronic properties.
- (2) In this thesis, we only measured RBS/channeling spectra across the $\langle 001 \rangle$ axis directions to determine the impurity lattice location. It is not enough to get the conclusion that Se atoms are precisely on a substitutional lattice location. One can measure channeling spectra across the $\langle 110 \rangle$ and $\langle 111 \rangle$ axis directions together with simulations to determine the impurity lattice location in future work.

(3) Silicon hyperdoped with chalcogens has recently gained much attention due to its unique optical and electrical properties, such as the strong sub-band photoresponse and the insulator-to-metal transition. These materials can be used for developing intermediate band solar cells and infrared photodiodes. Therefore, it is worth to explore the structural, electrical and optical properties of S or Te hyperdoped Si layers in the future and to explore the potential application for infrared sensing. Particularly the FLA process can be applied in the wafer scale. If the concept works, one can transfer the knowledge to industry applications.

References

- [1] R. Behrensmeier, M. Brede, and P. Haasen, *Scripta. Metal.* 21, 1581 (1987).
- [2] H. R. Vydyanath, W. J. Helm, J. S. Lorenzo, and S. T. Hoelke, *Infrared Phys.* 19, 93 (1979).
- [3] J. Wagner and J. A. Delalampo, *J. Appl. Phys.* 63, 425 (1988).
- [4] F. J. Morin and J. P. Maita, *Phys. Rev.* 96, 28 (1954).
- [5] G. L. Pearson and J. Bardeen, *Phys. Rev.* 75, 865 (1949).
- [6] R. Carlson, R. Hall, and E. Pell, *J. Phys. Chem. Solids* 8, 81 (1959).
- [7] F. A. Trumbore, *Bell System Technical Journal* 39, 205(1960).
- [8] S. Hocine and D. Mathiot, *Appl. Phys. Lett.* 53, 1269 (1988).
- [9] A. Luque, A. Martí, E. Antolín, and C. Tablero, *Phys. B: Condens. Matter* 382, 320 (2006).
- [10] E. (ed.) Abrahams, World Scientific, Singapour (2010).
- [11] E. R. Weber, *Appl. Phys. A* 30, 22 (1983).
- [12] F. Rollert, N.A. Stolwijk, H. Mehrer. *Appl. Phys. Lett.* 63, 506 (1993).
- [13] C. Kim, and M. Sakata. *Jpn. J. Appl. Phys.* 18, 2 (1979).
- [14] H. R. Vydyanath, J. S. Lorenzo, and F. A. Kroeger, *J. Appl. Phys.* 49, 5928 (1978).
- [15] S. U. Campisano, G. Foti, P. Baeri, M. G. Grimaldi, and E. Rimini, *Appl. Phys. Lett.* 37, 719 (1980).
- [16] S. A. Kokorowski, G. L. Olson, and L. D. Hess, *J. Appl. Phys.* 53, 921 (1982).
- [17] A. Lietoila, R. Gold, and J. Gibbons, *Appl. Phys. Lett.* 39, 810 (1981).
- [18] J. A. Roth, G. L. Olson, D. C. Jacobson, and J. M. Poate, *Appl. Phys. Lett.* 57, 1340 (1990).
- [19] L. Csepregi, E. Kennedy, J. Mayer, and T. Sigmon, *J. Appl. Phys.* 49, 3906 (1978).
- [20] B. P. Bob, A. Kohno, S. Charnvanichborikarn, J. M. Warrender, I. Umezu, M. Tabbal, J. S. Williams, and M. Aziz, *J. Appl. Phys.* 107, 123506 (2010).
- [21] S. Zhou F. Liu, S. Prucnal, K. Gao, M. Khalid, C. Baehtz, M. Posselt, W. Skorupa, and M. Helm, *Sci. Rep.* 5, 8329 (2015).
- [22] C. B. Simmons, A. J. Akey, J. J. Krich, J. T. Sullivan, D. Recht, M. J. Aziz, and T. Buonassisi, *J. Appl. Phys.* 114, 243514 (2013).

- [23] S. U. Campisano, E. Rimini, P. Baeri, and G. Foti, *Appl. Phys. Lett.* 37, 170 (1980).
- [24] J. Olea, E. López, E. Antolín, A. Martí, A. Luque, E. García-Hemme, D. Pastor, R. García-Hernansanz, A. del Prado, and G. González-Díaz, *J. Phys. D: Appl. Phys.* 49, 055103 (2016).
- [25] H. Castán, E. Pérez, H. García, S. Dueñas, L. Bailón, J. Olea, D. Pastor, E. García-Hemme, M. Irigoyen, and G. González-Díaz, *J. Appl. Phys.* 113, 024104 (2013).
- [26] A. Luque and A. Martí, *Phys. Rev. Lett.* 78, 5014 (1997).
- [27] T. G. Kim, J. M. Warrender, and M. J. Aziz, *Appl. Phys. Lett.* 88, 241902 (2006).
- [28] J. Olea, G. González-Díaz, D. Pastor, and I. Mártil, *J. Phys. D: Appl. Phys.* 42, 085110 (2009).
- [29] D. Pastor, J. Olea, A. Muñoz-Martín, A. Climent-Font, I. Mártil, and G. González-Díaz, *J. Appl. Phys.* 112, 113514 (2012).
- [30] K. Sánchez, I. Aguilera, P. Palacios, and P. Wahnón, *Phys. Rev. B* 79, 165203 (2009).
- [31] J. Mathews, A. J. Akey, D. Recht, G. Malladi, H. Efstathiadis, M. J. Aziz, and J. M. Warrender, *Appl. Phys. Lett.* 104, 112102 (2014).
- [32] J. E. Carey, C. H. Crouch, M. Shen, and E. Mazur, *Opt. Lett.* 30, 1773 (2005).
- [33] A. J. Said, D. Recht, J. T. Sullivan, J. M. Warrender, T. Buonassisi, P. D. Persans, and M. J. Aziz, *Appl. Phys. Lett.* 99, 073503 (2011).
- [34] S. Hu, P. Han, S. Wang, X. Mao, X. Li, and L. Gao, *Semicond. Sci. Technol.* 27, 102002 (2012).
- [35] E. Antolín, A. Martí, J. Olea, D. Pastor, G. González-Díaz, I. Mártil, and A. Luque, *Appl. Phys. Lett.* 94, 042115 (2009).
- [36] K. Sánchez, I. Aguilera, P. Palacios, and P. Wahnón, *Phys. Rev. B* 82, 165201 (2010).
- [37] K. M. Guenther, T. Gimpel, J. W. Tomm, S. Winter, A. Ruibys, S. Kontermann, and W. Schade, *Appl. Phys. Lett.* 104, 042107 (2014).
- [38] M. T. Winkler, D. Recht, M. -J. Sher, A. J. Said, E. Mazur, and M. J. Aziz, *Phys. Rev. Lett.* 106, 178701 (2011).
- [39] E. Ertekin, M. T. Winkler, D. Recht, A. J. Said, M. J. Aziz, T. Buonassisi, and J. C. Grossman¹, *Phys. Rev. Lett.* 108, 026401 (2012).

- [40] R. Minixhofer and Master thesis, Integrating Technology Simulation into the Semiconductor Manufacturing Environment (2006).
- [41] G. J. Phelps, *Modelling Simul. Mater. Sci. Eng.* 12, 1139 (2004).
- [42] H. Ryssel and I. Ruge, p7, ISBN 0-471-10311-X, New York: Wiley, (1986).
- [43] J. F. Ziegler, *Nucl. Instru. and Methods in Phys. Res. B* 219–220, 1027 (2004).
- [44] L. R. Doolittle, *Nucl. Instr. Meth. in Phys. Res. B* 9, 344 (1985).
- [45] S. Prucnal, T. Schumann, W. Skorupa, B. Abendroth, K. Krockert, and H.J. Möller, *Acta Phys. Pol. A* 120, 30 (2011).
- [46] W. Skorupa, T. Gebel, R. A. Yankov, S. Paul, W. Lerch, D. F. Downey, and E. A. Arevalo, *J. Electrochem. Soc.* 152, 436 (2005).
- [47] J. Perrière, *Pergamon Journals Ltd*, 37, 429 (1987).
- [48] L. C. Feldman, J. W. Mayer, and S. T. Picraux, *Academic Press* (1982).
- [49] L. J. van der Pauw, *Philips Res. Repts.* 13,1 (1958).
- [50] A. H. A. Hassan, PhD Thesis, Transport properties for pure strained Ge quantum well (2014).
- [51] D. Pastor, J. Olea, A. Del Prado, E. García-Hemme, R. García-Hernansanz, I. Mártel, and D. González-Díaz, *J. Phys. D: Appl. Phys.* 46, 135108 (2013).
- [52] Y. Zhou, F. Liu, M. Zhu, X. Song, and P. Zhang, *Appl. Phys. Lett.* 102, 222106 (2013).
- [53] G. K. Celler, J. M. Poate and L. C. Kimerling, *Appl. Phys. Lett.* 32, 464 (1978).
- [54] T. Venkatesan, J. Golovchenko, J. Poate, P. Cowan, and G. K. Celler, *Appl. Phys. Lett.* 33, 429 (1978).
- [55] J. A. Kittl, P. G. Sanders, M. J. Aziz, D. P. Brunco, and M. O. Thompson *Acta Mater.* 48, 4797 (2000).
- [56] R. Reitano, P. M. Smith, and M. J. Aziz, *J. Appl. Phys.* 76 1518 (1994).
- [57] J. Mathews, A. J. Akey, D. Recht, G. Malladi, H. Efstathiadis, M. J. Aziz, and J. M. Warrender, *Appl. Phys. Lett.* 104, 112102 (2014).
- [58] W. Skorupa, T. Gebel, R. A. Yankov, S. Paul, W. Lerch, D. F. Downey, and E. A. Arevalo, *J. Electrochem. Soc.* 152, 436 (2005).
- [59] M. C. Lee, C. R. Huang, Y. S. Chang, and Y. F. Chao, *Phys. Rev. B* 40, 10420 (1989).
- [60] D. Recht, M. J. Smith, S. Charnvanichborikarn, J. T. Sullivan, M. T. Winkler, J. Mathews, J. M. Warrender, T. Buonassisi, J. S. Williams, S. Gradecák, and M. J. Aziz, *J. Appl. Phys.* 114, 124903 (2013).

- [61] L. M. Goldman and M. J. Aziz, *J. Mater. Res.* 2, 524 (1987).
- [62] J. Narayan, *J. Appl. Phys.* 52, 1289 (1981).
- [63] J. Narayan, *J. Cryst. Growth.* 59 583 (1982).
- [64] A. G. Cullis, D. T. J. Hurle, H. C. Webber, N. G. Chew, J. M. Poate, P. Baeri, and G. Foti, *Appl Phys. Lett.* 38, 642 (1981).
- [65] A. G. Cullis, H. C. Webber, N. G. Chew, J. M. Poate, and P. Baeri, *Phys. Rev. Lett.* 49, 219 (1982).
- [66] G. Foti, E. Rimini, W. S. Tseng, and J. W. Mayer, *Appl. Phys.* 15, 365 (1978).
- [67] R. Duffy, V. C. Venezia, K. van der Tak, M. J. P. Hopstaken, G. C. J. Maas, F. Roozeboom, Y. Tamminga, and T. Dao, *J. Vac. Sci. Technol. B* 23, 2021 (2005).
- [68] A. G. Cullis, N. G. Chew, H. C. Webber, and D. J. Smith, *J. Cryst. Growth.* 68, 624 (1984).
- [69] C. W. White, B. R. Appleton, B. Stritzker, D. M. Zehner, and S. R. Wilson, *MRS Proc.* 1, 59 (1980).
- [70] R. G. Elliman and Z. W. Fang, *J. Appl. Phys.* 73 3313 (1993).
- [71] S. A. Kokorowski, G. L. Olson, and L. D. Hess, *J. Appl. Phys.* 53, 921 (1982).
- [72] J. A. Burton, R. C. Prim and W. P. Slichter, *J. Chem. Phys.* 21, 1987 (1953).
- [73] Y. Berencén, S. Prucna, F. Liu, I. Skorupa, R. Hübner, L. Rebohle, S. Zhou, H. Schneider, M. Helm, and W. Skorupa, *Sci. Rep.* 7, 43688 (2017).
- [74] C. H. Crouch, J. E. Carey, M. Shen, E. Mazur, and F. Y. Génin, *Appl. Phys. A* 79, 1635–1641 (2004).
- [75] M. A. Sheehy, B. R. Tull, C. M. Friend, and E. Mazur, *Mater. Sci. & Eng.: B* 137, 289–294 (2007).
- [76] J. Olea, M. Toledano-Luque, D. Pastor, G. González-Díaz, and I. Mártil, *J. Appl. Phys.* 104, 016105 (2008).
- [77] J. Olea, A. del Prado, E. García-Hemme, R. García-Hernansanz, and G. González-Díaz, *Sol. Energy Mater. Sol.* 104, 159–164 (2012).
- [78] V. P. Markevich, S. Leonard, A. R. Peaker, B. Hamilton, A. G. Marinopoulos, and J. Coutinho, *Appl. Phys. Lett.* 104, 152105 (2014).
- [79] J. Olea, A. del Prado, D. Pastor, I. Mártil, and G. González-Díaz, *J. Appl. Phys.* 109, 113541 (2011).
- [80] F. Liu, S. Prucnal, R. Hübner, Y. Yuan, W. Skorupa, M. Helm, and S. Zhou, *J. Phys. D: Appl. Phys.* 49, 245104 (2016).

- [81] S. Prucnal, M. Turek, A. Drozdziel, K. Pyszniak, S. Zhou, A. Kanjilal, W. Skorupa, and J. Zuk, *Appl. Phys. B* 101, 315-319 (2010).
- [82] M. L. Swanson, *Vacuum* 39, 87-90 (1989).
- [83] R. Jones, S. Öberg, F. Berg Rasmussen, and B. Bech Nielsen, *Phys. Rev. Lett.* 72, 1882 (1994).
- [84] P. Sheng, B. Abeles, and Y. Arie, *Phys. Rev. Lett.*, 31, 44(1973).
- [85] S. Bl, and A. Efros, *Springer Series in Solid-State Sciences*, 45, 203(1984).
- [86] B. Abeles, H. L. Pinch, and J. I. Gittleman, *Phys. Rev. Lett.* 35, 247(1975).
- [87] A. Zabrodskii, *Philos. Mag. B*, 81, 1131-1151(2001).
- [88] E. García-Hemme, D. Montero, R. García-Hernansanz, J. Olea, I. Mártil, and G. González-Díaz, *J. Phys. D: Appl. Phys.* 49, 275103(2016).
- [89] A. J. Akey, D. Recht, J. S. Williams, M. J. Aziz, and T. Buonassisi, *Adv. Funct. Mater.* 25, 4642 (2015).
- [90] E. García-Hemme, R. García-Hernansanz, J. Olea, D. Pastor, A. Del Prado, I. Mártil, and G. González-Díaz, *Appl. Phys. Lett.* 101, 192101 (2012).
- [91] E. García-Hemme, R. García-Hernansanz, J. Olea, D. Pastor, A. Del Prado, I. Mártil, and G. González-Díaz, *Appl. Phys. Lett.* 104 (21), 211105 (2014).
- [92] A. Luque, A. Martí, and C. Stanley, *Nat. Photonics* 6, 146 (2012).
- [93] C. H. Crouch, J. E. Carey, J. M. Warrender, E. Mazur, M. J. Aziz, and F. Genin, *Appl. Phys. Lett.* 84, 1850 (2004).
- [94] M. A. Sheehy, L. Winston, J. E. Carey, C. M. Friend, and E. Mazur, *Chem. Mater.* 17, 3582 (2005).
- [95] K.-F. Wang, H. Shao, K. Liu, S. Qu, Y. Wang, and Z. Wang, *Appl. Phys. Lett.* 107, 112106 (2015).
- [96] H. Shao, Y. Li, J. Zhang, B.-Y. Ning, W. Zhang, X.-J. Ning, L. Zhao, and J. Zhuang, *Europhys. Lett.* 99, 46005 (2012).
- [97] J.-W. Chen, and A. G. Milnes, *Ann. Rev. Mater. Sci.* 10, 157-228 (1980).
- [98] V. A. Singh, U. Lindefelt, and A. Zunger, *Phys. Rev. B* 27, 4909 (1983).
- [99] D. Pastor, J. Olea, A. del Prado, E. García-Hemme, R. García-Hernansanz, and G. González-Díaz, *Sol. Energy Mater. Sol. Cells* 104, 159 (2012).
- [100] P. P. Edwards and M. J. Sienko, *Phys. Rev. B* 17, 2575 (1978).
- [101] T. F. Rosenbaum, R. F. Milligan, M. A. Paalanen, G. A. Thomas, R. N. Bhatt and W. Lin *Phys. Rev. B* 27, 7509 (1983).

- [102] X. Mao, P. Han, S. Hu, L. Gao, X. Li, Y. Mi, and P. Liang, *Chin. Phys. Lett.* 29, 097101 (2012).
- [103] S. Hu, P. Han, P. Liang, Y. Xing, and S. Lou, *Mater. Sci. Semicond. Process.* 17, 134 (2014).
- [104] S. Prucnal, F. Liu, M. Voelskow, L. Vines, L. Rebohle, D. Lang, Y. Berencén, S. Andric, R. Boettger, M. Helm, S. Zhou, and W. Skorupa, *Sci. Rep.* 6, 27643 (2016).
- [105] S. Prucnal, F. Liu, Y. Berencén, L. Vines, L. Bischoff, J. Grenzer, S. Andric, S. Tiagulskyi, K. Pysznik, M. Turek, A. Drozdziel, M. Helm, S. Zhou, and W. Skorupa, *Semi. Sci. & Technol.* 31, 105012 (2016).
- [106] L. Rebohle, S. Prucnal, and W. Skorupa, *Semi. Sci. & Technol.* 31, 103001 (2016).
- [107] H. R. Vydyanath, J. S. Lorenzo, and F. A. Kroger, *J. Appl. Phys.* 49, 5928-5937 (1978).
- [108] J. Ziegler, J. Biersack, and U. Littmark, *The Stopping and Range of Ions in Solids*, Vol. 1, (Pergamon, Oxford, 1985).
- [109] H. Shao, C. Liang, Z. Zhu, B. Ning, X. Dong, X. Ning, L. Zhao, and J. Zhuang, *Appl. Phys. Express* 6, 085801(2013).
- [110] P. A. Temple and C. E. Hathaway, *Phys. Rev. B* 7, 3685 (1973).
- [111] A. G. Zabrodsii, *Philos. Mag. B* 81, 1131 (2001).
- [112] B. Shklovskii and A. Efros, *Springer Series in Solid-State Sciences*, Vol. 45. (Springer-Verlag, Berlin, 1984).
- [113] M. Tabbal, T. Kim, D. Woolf, B. Shin, M. Aziz, *Appl. Phys. A* 98, 589 (2010).
- [114] I. Umezu, J. M. Warrender, S. Charnvanichborikarn, A. Kohno, J. S. Williams, M. Tabbal, D. G. Papazoglou, X. C. Zhang, M. J. Aziz, *J. Appl. Phys.* 113, 213501 (2013).
- [115] R. O. Carlson, R. N. Hall, E. M. Pell, *J. Phys. Chem. Solids* 8, 81 (1959).
- [116] J. Ziegler, J. Biersack, and U. Littmark, (Oxford: Pergamon) 1985.
- [117] A. McMahon, M. P. Smith, K. A. Seffen, M. Voelskow, W. Anwand, and W. Skorupa, *Vacuum* 81, 1301 (2007).

Publications

1. **F. Liu**, S. Prucnal, R. Hübner, Y. Yuan, W. Skorupa, M. Helm, and S. Zhou, *Suppressing the cellular breakdown in silicon supersaturated with titanium*, **J. Phys. D: Appl. Phys.** 49, 245104 (2016). [\(Chapter 3\)](#)
2. **F. Liu**, M. Wang, Y. Berencén, S. Prucnal, M. Engler, R. Hübner, Y. Yuan, R. Heller, R. Böttger, L. Rebohle, W. Skorupa, M. Helm, and S. Zhou, *On the insulator-to-metal transition in titanium-implanted silicon*, **Scientific Reports** 8, 4164 (2018). [\(Chapter 4\)](#)
3. **F. Liu**, S. Prucnal, Y. Berencén, Z. Zhang, Y. Yuan, Y. Liu, R. Heller, R. Boettger, L. Rebohle, W. Skorupa, M. Helm, and S. Zhou, *Realizing the insulator-to-metal transition in Se-hyperdoped Si via non-equilibrium material processing*, **J. Phys. D: Appl. Phys.** 50, 415102 (2017). [\(Chapter 5\)](#)
4. **F. Liu**, S. Prucnal, Y. Yuan, R. Heller, Y. Berencén, R. Boettger, L. Rebohle, W. Skorupa, M. Helm, and S. Zhou, *Structural and electrical properties of Se-hyperdoped Si via ion implantation and flash lamp annealing*, **Nuclear Inst, and Methods in Physics Research B** 424, 52–55 (2018). [\(Chapter 6\)](#)
5. S. Prucnal, **F. Liu**, M. Voelskow, L. Vines, L. Rebohle, D. Lang, Y. Berencén, S. Andric, R. Boettger, M. Helm, S. Zhou, and W. Skorupa, *Ultra-doped n-type germanium thin films for sensing in the mid-infrared*, **Scientific Reports** 6, 27643 (2016).
6. S. Prucnal, **F. Liu**, Y. Berencén, L. Vines, L. Bischoff, J. Grenzer, S. Andric, S. Tiagulskiy, K. Pysznik, M. Turek, A. Drozdziel, M. Helm, S. Zhou, and W. Skorupa, *Enhancement of carrier mobility in thin Ge layer by Sn co-doping*, **Semi. Sci. & Technol.** 31, 105012 (2016).
7. S. Zhou, **F. Liu**, S. Prucnal, K. Gao, M. Khalid, C. Baetz, M. Posselt, W. Skorupa, and M. Helm, *Hyperdoping silicon with selenium: solid vs. liquid phase epitaxy*, **Scientific Reports** 5, 8329 (2015).
8. J. Zhu, **F. Liu**, S. Zhou, C. Franke, S. Wimmer, V. V. Volobuev, G. Springholz, A. Pashkin, H. Schneider, and M. Helm, *Lattice vibrations and electrical transport in (Bi_{1-x}In_x)₂Se₃ films*, **Appl. Phys. Lett.** 109, 202103 (2016).
9. Y. Berencén, S. Prucnal, **F. Liu**, I. Skorupa, R. Hübner, L. Rebohle, S. Zhou, H. Schneider, M. Helm, and W. Skorupa, *Room-temperature short-wavelength infrared Si photodetector*, **Scientific Reports** 7, 43688 (2017).

10. Y. Yuan, R. Hübner, **F. Liu**, M. Sawicki, O. Gordan, G. Salvan, D. R. T. Zahn, D. Banerjee, C. Baehtz, M. Helm, and S. Zhou, *Ferromagnetic Mn-Implanted GaP: Microstructures vs Magnetic Properties*, **ACS Applied Materials and Interfaces** 8, 3912-3918 (2016).
11. Y. Liu, Y. Yuan, **F. Liu**, R. Böttger, W. Anwand, Y. Wang, A. Semisalova, A. N. Ponomaryov, X. Lu, A. T. N'Diaye, E. Arenholz, V. Heera, W. Skorupa, M. Helm, and S. Zhou, *Interaction between magnetic moments and itinerant carriers in d0 ferromagnetic SiC*, **Phys. Rev. B** 95, 195309 (2017).
12. Y. Tan, Z. Guo, Z. Shang, **F. Liu**, R. Böttger, S. Zhou, J. Shao, X. Yu, H. Zhang, and F. Chen, *Tailoring nonlinear optical properties of Bi₂Se₃ through ion irradiation*, **Scientific Reports** 6, 21799 (2016).
13. Y. Liu, L. Chen, D. Hilliard, Q.-S. Huang, **F. Liu**, M. Wang, R. Böttger, R. Hübner, A. T. N'Diaye, E. Arenholz, V. Heera, W. Skorupa, and S. Zhou, *Controllable growth of vertically aligned graphene on C-face SiC*, **Scientific Reports** 6, 34814 (2016).
14. Y. Liu, Z. Li, L. Guo, X. Chen, Y. Yuan, **F. Liu**, S. Prucnal, M. Helm, and S. Zhou, *Intrinsic diamagnetism in the Weyl semimetal TaAs*, **J. Magn. Magn. Mater.** 408, 73-76 (2016).
15. S. Prucnal, J. Wu, Y. Berencen, M. O. Liedke, A. Wagner, **F. Liu**, M. Wang, L. Rebohle, S. Zhou, H. Cai, and W. Skorupa, *Engineering of optical and electrical properties of ZnO by non-equilibrium thermal processing: The role of zinc interstitials and zinc vacancies*, **J. Appl. Phys.** 122, 035303 (2017).
16. Y. Liu, R. Pan, X. Zhang, J. Han, Q. Yuan, Y. Tian, Y. Yuan, **F. Liu**, Y. Wang, A. T. N'Diaye, E. Arenholz, X. Chen, Y. Sun, B. Song, and S. Zhou, *Vacancy Defect Complexes in Silicon: Charge and Spin Order*, **Phys. Rev. B** 94, 195204 (2016).

Erklärung

Hiermit versichere ich, dass ich die vorliegende Arbeit ohne unzulässige Hilfe Dritter und ohne Benutzung anderer als der angegebenen Hilfsmittel angefertigt habe; die aus fremden Quellen direkt oder indirekt übernommenen Gedanken sind als solche kenntlich gemacht. Die Arbeit wurde bisher weder im Inland noch im Ausland in gleicher oder ähnlicher Form einer anderen Prüfungsbehörde vorgelegt.

Diese Dissertation wurde angefertigt im

Helmholtz-Zentrum Dresden-Rossendorf
Institut für Ionenstrahlphysik und Materialforschung
Bautzner Landstr. 400, 01328 Dresden,

Die wissenschaftliche Betreuung der Arbeit erfolgte durch Prof. Dr. Manfred Helm.

Ich versichere, an keiner Institution, auch nicht im Ausland, jemals den Antrag auf Eröffnung eines Promotionsverfahrens gestellt zu haben.

Ich erkenne die Promotionsordnung der Fakultät Mathematik und Naturwissenschaften der Technischen Universität Dresden an.

15.12.2017

Fang Liu